Linear stability of a weakly magnetized rotating plasma column.

Aggarwal Surabhi

Aix*Marseille université
Socialement engagée

NNT/NL : 2023AIXM0338

THÈSE DE DOCTORAT

Soutenance à Aix-Marseille Université
le 17 Octobre 2023 par

Surabhi Aggarwal

Linear stability of a weakly magnetized rotating plasma column

Discipline
Physique et Sciences de la Matière

Spécialité
ENERGIE, RAYONNEMENT ET PLASMA

École doctorale
ED 352

Laboratoire/Partenaires de recherche
Centre National de la Recherche Scientifique
Physique des Interactions Ioniques et Moléculaires,
UMR 7345-CNRS

Composition du jury

Alexandre Escarguel PIIM, AMU	Directeur de thèse
Yann Camenen PIIM, CNRS	Co-directeur de thèse
Gwenaël Fubiani Laboratoire LAPLACE , Univ. Toulouse Paul Sabatier	Président du jury, Rapporteur
Etienne Gravier Institut Jean Lamour , Univ. de Lorraine	Rapporteur
Laurence Kovacic PIIM, AMU	Examinatrice
Sedina Tsikata Daniel Guggenheim School of Aerospace Engineering , Georgia Tech	Examinatrice

cnrs

PIIM

Contents

Affidavit

Je soussignée, Surabhi Aggarwal, déclare par la présente que le travail présenté dans ce manuscrit est mon propre travail, réalisé sous la direction scientifique d'Alexandre Escarguel et de Yann Camenen, dans le respect des principes d'honnêteté, d'intégrité et de responsabilité inhérents à la mission de recherche. Les travaux de recherche et la rédaction de ce manuscrit ont été réalisés dans le respect à la fois de la charte nationale de déontologie des métiers de la recherche et de la charte d'Aix-Marseille Université relative à la lutte contre le plagiat.

Ce travail n'a pas été précédemment soumis en France ou à l'étranger dans une version identique ou similaire à un organisme examinateur.

Fait à Marseille le 10/07/2023

Acknowledgements

Finally, it's time to say thanks to all the amazing people who were an important part of these three years. Needless to say, I hope they will continue to remain part of this journey wherever I will go. It has to begin with Alexandre and Yann for being a constant support of guidance throughout these three years. Before coming to Marseille, I had not much idea with whom I will be working but I have to say it was a great pleasure to work with both of you. You both were always there to help, support and guide me whenever I need some advice with work or with bureaucracy. Thanks a lot, Yann for always being so patient with me and answering all my questions and doubt. You always welcomed me into your office with a great smile, no matter how many times I knock on your door. Thanks for being patient with my naive questions. The kind of enthusiasm and passion that you have for research is amazing and it motivates me a lot. Thanks a lot, Alexandre for always guiding the experimental work patiently. Whatever I know about experiments is all because of you. You have always cleared my doubts with such ease and patience. I would be happy if I will be able to keep and forward whatever I have learned regarding experiments from you. Thanks to both of you for always being available whenever I need. Thanks for devoting this much time and effort in thoroughly examining this thesis as well. This work would not have been accomplished without the help of Alexandre Poye. You and Yann are the reason that I can now program efficiently. You have always encouraged me to do things that I sometimes think I am not capable of. Thanks for always being a person of constant support and guidance.

I would also like to thank Dr. Sedina Tiskata and Dr. Laurence Kovacic for taking out the time to read my manuscript and to accept to be part of the jury. Special thanks to Dr. Etienne Gravier and Dr. Gwenael Fubiani for reading the manuscript thoroughly and accepting the offer of being the jury member in my PhD defense.

Special thanks to all the people in the administrative department especially - Marie Pierre, Zaina, and Eric. Eric, I know that I have disturbed you a lot since the beginning of my Ph.D. Thanks for always being patient with all my queries.

I express deep gratitude to all the members of the TP and PTM research groups at PIIM. The supportive atmosphere they created has greatly contributed to my thesis progress and overall work experience.

These years of Ph.D. wouldn't have been easier if I hadn't crossed paths with some of the amazing friends I made these years. I would like to thank all my friends whom I

met from Europhtonics - Jaime, Maran, Sarah, Nur, Murtaza, and Narmin who made my first few months in Marseille as memorable as they could be. Especially to Jaime, Maran, and Sarah, we have traveled a lot together and I hope will continue to do that and make more beautiful memories. It's always fun to be with you all. Thank you, Sonia, for always being there whenever I need you. Having you was like having a roommate that I could always rely on. We spent a lot of tough and good times together during these three years which I will always cherish.

My special thanks to all my friends and labmates at PIIM. Neeraj for helping me when I was in India as well as in Marseille, Samuele for always complaining and making me laugh and being a nice flatmate as well, Federica for always being there for everything whether it's traveling, eating out, or just talking, Mattia for always being the funny one, Anass and Alodie for being such nice friends. Many thanks to all the friends with whom I shared my office - Julien for always being there to discuss the stuff about physics, programming, and whatnot, Mattheus for the chocolates and cookies, and Nicholas and Khalil for being always helpful. I will always cherish the time I spent with you all. Not to forget some amazing people I met in Lausanne especially, Rita, Lorenzo, Jia, Simon, Claudia, Antonia, and of course Francesco. The time I spent with you guys was amazing. Francesco, I am sorry but I can never help with my sarcasm towards you, it just comes naturally.

I am thankful to all my friends in India who always take out some time for me - Harmeet, Kunika, Jasdeep, Seema, Simran, Reema, and Manisha. Thanks for always being in touch even though we are farther apart and for your constant support for all these years. I always look forward to meeting you all whenever I visit India.

I would certainly like to thank my mentors from my Master's studies, Dr. Saini, and Dr. Yashika Ghai. Thank you for your constant support and motivation. A heartful thanks to Yashika for always taking my calls, for her constant encouragement, and for taking the time to answer my questions. You have always guided me in the right direction whenever needed. I hope I could be as helpful and kind to someone as much as you are to me.

It's time to say a big thanks to them, because of whom, I am able to reach up to this point, Mama and Papa. I cannot thank you enough for whatever you have done for me so far. You have cried with me, laughed with me, and celebrated with me. Thanks for checking up on me every day even though we are so far from each other. These three years have not been easier but you have always supported me. A special thanks to my brother and all my family members. And finally, my deepest gratitude to dadi maa, I always regret not getting a chance to see or talk to you during your last days. I know you would have been the happiest and most excited among everyone on the day of my defense. This is for you, dadi maa.

Liste de publications et participation aux conférences

Liste des publications réalisées dans le cadre du projet de thèse:

1. S. Aggarwal, Y. Camenen, A. Escarguel, A. Poyé, “Centrifugal instability in a weakly magnetized rotating plasma column”. In: Journal of Plasma Physics, 89(3), 905890310, doi:10.1017/S002237782300051X (2023).

2. S. Aggarwal, Y. Camenen, A. Escarguel, “Fluid modeling of the weakly magnetized plasma column MISTRAL", Conference Proceedings. In: 47th European Physical Society Conference on Plasma Physics (EPS 2022), Virtual conference. https://indico.fusenet.eu/event/28/contributions/484/attachments/498/1116/eps_paper_surabhi.pdf

Participation aux conférences et écoles d’été au cours de la période de thèse:

1. **Poster**
   a) S. Aggarwal, Y. Camenen, A. Escarguel, A. Poyé “Centrifugal instability in a weakly magnetized bounded plasma column". In: 48th European Physical Society Conference on Plasma Physics (EPS 2023), Bordeaux, France, 3.07-07.07.2023.
   b) S. Aggarwal, Y. Camenen, A. Escarguel, “Linear Stability of the weakly magnetized plasma column MISTRAL". In: Europhysics Conference on the Atomic and Molecular Physics of Ionized Gases (ESCAMPIG 2022), Sorbonne University, Paris, 19.07-23.07.2022.
   c) S. Aggarwal, Y. Camenen, A. Escarguel, “Fluid modeling of the weakly magnetized plasma column MISTRAL". In: 47th European Physical Society Conference on Plasma Physics (EPS 2022), Virtual conference 27.06-01.07.2022.
   d) S. Aggarwal, Y. Camenen, A. Escarguel, T. Vidril, “Study of abnormal transport in a magnetized plasma column". In: Journées 2021 du GDR EMILI, École Polytechnique, Paris 25.10-28.10.2021.

2. **Oral presentations**

   a) S. Aggarwal, Y. Camenen, A. Escarguel, A. Poyé “Development in two-fluid model to study instabilities in **E**× **B** plasmas".In: SoPlasma Workshop (SoP 2023), ENS Lyon, France, 15.06-16.06.2023.

   b) S. Aggarwal, Y. Camenen, A. Escarguel, “Linear Stability of rotating plasma columns". In: SoPlasma Workshop (SoP 2022), Marseille, France, 14.06-16.06.2022.

Résumé

La compréhension et la prévision du comportement des particules chargées dans les plasmas magnétisés, ainsi que l'auto-organisation de ces systèmes complexes, revêtent une importance capitale tant pour la recherche fondamentale que pour les applications technologiques. Lorsque des particules chargées se déplacent à travers des champs magnétiques, elles génèrent des courants qui, à leur tour, exercent un couple $\mathbf{j}\times\mathbf{B}$ sur le plasma, conduisant à l'émergence d'écoulements à grande échelle. Ces écoulements ont un impact significatif sur le transport perpendiculaire et conduisent le système vers un état statistique moyen par le développement de structures, d'instabilités et de turbulences à grande échelle. L'étude des plasmas fortement magnétisés a fait l'objet d'une attention considérable au cours des dernières décennies, principalement en raison de son importance pour la fusion par confinement magnétique. Les plasmas faiblement magnétisés ont été relativement peu étudiés malgré leur prévalence dans la nature et la technologie. Appréhender la formation de structures à grande échelle dans ces plasmas représente une étape cruciale vers le développement de capacités prédictives pour les dispositifs $\mathbf{E}\times\mathbf{B}$ dédiés à l'étude des phénomènes fondamentaux de la physique des plasmas. En outre, il existe un intérêt croissant pour l'exploration de l'impact des collisions dans les plasmas faiblement ionisés dans le contexte astrophysique, où les collisions affectent naturellement les courants et la rotation.

Le dispositif expérimental standard pour l'étude des plasmas faiblement magnétisés consiste en une colonne de plasma cylindrique immergée dans un champ magnétique axial. MISTRAL est un dispositif de ce type basé au laboratoire PIIM pour étudier le plasma dans une configuration de champ croisé ($\mathbf{E}\perp\mathbf{B}$). La formation de structures rotatives cohérentes dans MISTRAL est supposée être due au dèveloppement d'instabilités en présence d'un écoulement $\mathbf{E}\times\mathbf{B}$. Plusieurs mécanismes potentiels, y compris les ondes de dérive, l'instabilité de Rayleigh-Taylor/Centrifuge, l'instabilité de Kelvin-Helmholtz et l'instabilité de traînée neutre, ont été identifiés comme contribuant potentiellement à la formation de structures tournantes dans MISTRAL. Cependant, l'identification des instabilités responsables de leur émergence et des déclencheurs spécifiques impliqués reste difficile à obtenir. Cette thèse s'efforce de répondre à ces questions.

Une étude expérimentale du plasma MISTRAL a été réalisée pour établir les bases de la modélisation théorique. Un modèle à deux fluides a été développé pour étudier la stabilité linéaire des colonnes de plasma en rotation. Des travaux antérieurs ont démontré que les colonnes de plasma rotatives sont sensibles à l'instabilité cen-

trifuges. Cependant, la plupart des modèles existants reposent sur l'approximation basse fréquence (LFA), qui est valable lorsque la fréquence d'instabilité et la fréquence d'écoulement d'équilibre sont considérablement plus petites que la fréquence cyclotronique. Cette hypothèse est remise en question dans de nombreux dispositifs à plasma de laboratoire, y compris les colonnes à plasma faiblement magnétisées comme MISTRAL. Pour remédier à cette limitation, une relation de dispersion globale radiale décrivant l'instabilité centrifuge sans la LFA a été dérivée. Le domaine de validité de l'approximation à basse fréquence a été discuté. En outre, l'influence de la limite radiale sur la stabilité linéaire a été examinée. On a constaté que l'écoulement d'équilibre et la limite radiale influencent fortement le taux de croissance et la fréquence des modes existants. Une comparaison a été faite entre les résultats obtenus en utilisant la relation de dispersion avec l'approximation radiale locale et ceux obtenus en utilisant la relation de dispersion radiale globale. Cette comparaison a révélé la non-applicabilité de la solution locale aux systèmes de plasma de type MISTRAL.

En raison de la fraction élevée de neutres dans le système de plasma actuel, le modèle a été étendu pour inclure les effets dus aux collisions ion-neutre dans la limite $\epsilon << 1$ avec $\epsilon = \bar{\nu}_{in}\bar{\omega}_0/C$. Dans cette première étape, la relation de dispersion est obtenue dans la limite $\epsilon \to 0$ qui est applicable pour la gamme de fréquences trouvée dans MISTRAL. Une comparaison est ensuite faite entre les solutions obtenues dans le cas sans collision et dans le cas avec collisions pour mettre en évidence l'effet de la collisionnalité sur le taux de croissance et la fréquence des modes.

Mots-clés: plasma, instabilités, **E**×**B** configuration, structures tournantes, modélisation des fluides, stabilité linéaire.

Abstract

Understanding and predicting the behavior of charged particles in magnetized plasmas, as well as the self-organization of these intricate systems, holds paramount importance in both fundamental research and technological applications. When charged particles move across magnetic fields, they generate currents that, in turn, exert a $\mathbf{j}\times\mathbf{B}$ torque on the plasma, leading to the emergence of large-scale flows. These plasma flows significantly impact perpendicular transport and drive the system towards a statistical mean state through the development of large-scale structures, instabilities, and turbulence. The study of strongly magnetized plasmas has received considerable attention over the past decades, primarily due to its relevance in magnetic confinement fusion. Weakly magnetized plasmas have been relatively less studied despite their prevalence in nature and technology. Understanding the formation of large-scale structures in such plasmas represents a crucial step towards developing predictive design capabilities for $\mathbf{E}\times\mathbf{B}$ devices dedicated to investigating fundamental plasma physics phenomena. Furthermore, there is a growing interest in exploring the impact of collisions in weakly ionized plasmas within the astrophysical context, where collisions naturally affect currents and rotation.

The standard experimental arrangement for examining weakly magnetized plasmas consists of a cylindrical plasma column immersed in an axial magnetic field. MISTRAL is such a device based at PIIM laboratory to study plasma in cross-field configuration ($\mathbf{E}\perp\mathbf{B}$). The formation of coherent rotating structures formed in MISTRAL is supposed to be due to an interplay between various instabilities and the $\mathbf{E}\times\mathbf{B}$ flow. Several potential mechanisms, including drift waves, Rayleigh-Taylor/Centrifugal instability, Kelvin-Helmholtz instability, and neutral drag instability, have been identified as potential contributors to the formation of rotating structures in MISTRAL. However, a definitive understanding of which instabilities are accountable for their emergence and the specific triggers involved remains elusive. This thesis endeavors to address these questions.

An experimental investigation of MISTRAL plasmas has been performed in a typical configuration with the rotating spoke. In parallel, theoretical work has been performed based on the experimental data. A two-fluid model has been developed to discuss the linear stability of rotating plasma columns. Prior works have demonstrated that rotating plasma columns are susceptible to centrifugal flute modes. However, the existing models rely on the low-frequency approximation (LFA), which holds true when the instability frequency and equilibrium flow frequency are considerably smaller than the ion-cyclotron frequency. This assumption is challenged in numerous laboratory

plasma devices, including weakly magnetized plasma columns like MISTRAL. To address this limitation, a radially global dispersion relation describing the centrifugal instability without the LFA has been derived. The validity range of the low-frequency approximation has been discussed. Additionally, the influence of the radial boundary on linear stability has been examined. The equilibrium flow and radial boundary have been found to strongly influence the growth rate and frequency of the existing modes. A comparison has been made between the results obtained using the dispersion relation with the radially local approximation and those obtained using the radially global dispersion relation. This comparison revealed the non-applicability of the local solution to MISTRAL-like plasma systems.

Due to the high fraction of neutrals in the present plasma system, the model was further extended to include the effects due to ion-neutral collisions in the limit $\epsilon << 1$ with $\epsilon = \bar{\nu}_{in}\omega_0/C$. In this first step, the dispersion relation is obtained in the limit $\epsilon \to 0$ which is applicable for the frequency range found in MISTRAL. A comparison is then made between the solutions obtained from the collisionless case and the one with collisions to highlights the effect of collisionality on the growth rate and frequency of the modes.

Keywords: plasma, instabilities, **E**×**B** configuration, rotating structures, fluid modeling, linear stability.

Résumé (Version étendue)

La compréhension et la prévision du comportement des particules chargées dans les plasmas magnétisés, ainsi que l'auto-organisation de ces systèmes complexes, occupent une importance capitale tant pour la recherche fondamentale que pour les applications. Lorsque des particules chargées se déplacent à travers un champs magnétique, elles génèrent des courants qui, à leur tour, exercent un couple $\mathbf{j}\times\mathbf{B}$ sur le plasma, conduisant à l'émergence d'écoulements à grande échelle. Ces écoulements ont un impact significatif sur le transport perpendiculaire et conduisent le système vers un état statistique moyen par le développement de structures, d'instabilités et de turbulences à grande échelle. L'étude des plasmas fortement magnétisés a fait l'objet d'une attention considérable au cours des dernières décennies, principalement en raison de leur importance pour la fusion par confinement magnétique. Les plasmas faiblement magnétisés ont été beaucoup moins étudiés malgré leur importance en ce qui concerne les applications technologiques. Appréhender la formation de structures à grande échelle dans ces plasmas représente une étape cruciale vers la possibilité de concevoir des dispositifs $\mathbf{E}\times\mathbf{B}$ dédiés à l'étude des phénomènes fondamentaux en physique des plasmas. En outre, il existe un intérêt croissant pour l'exploration de l'impact des collisions dans les plasmas faiblement ionisés dans le contexte astrophysique, où elles affectent naturellement les courants et la rotation.

Les structures cohérentes en rotation, qui sont supposées se former suite à la manifestation d'instabilités, ont été observées dans les propulseurs à effet Hall où elles peuvent limite leurs performances. Elles correspondent à une augmentation locale de la densité du plasma. Des structures cohérentes résultant de l'auto-organisation du plasma sont également observées dans les plasmas des tokamaks. Il est important de mieux comprendre les mécanismes conduisant à la formation de ces structures et leur relation avec les instabilités et le transport du plasma. Cette thèse s'efforce de répondre à ces questions.

Dans ce qui suit, un bref résumé du manuscrit est donné. Il présente les concepts clés de la thèse et tous les résultats notables obtenus.

Le premier chapitre de la thèse donne une description générale des plasmas, suivie d'une présentation de plusieurs expériences sur les plasmas et de leurs applications. Dans la majorité des expériences à plasma examinés, un champ magnétique externe est appliqué pour confiner le plasma, ce qui l'isole des parois et réduit les pertes d'énergie, de sorte que le plasma peut être chauffé pour atteindre une température élevée, par exemple celle requise pour la réaction thermonucléaire dans les applica-

tions de fusion. Dans les systèmes de plasma à basse température, le champ magnétique peut être utilisé pour confiner les électrons, ce qui permet de maintenir la température électronique nécessaire à l'ionisation du gaz neutre. Cela tend à générer des gradients importants, par exemple une pression plus importante au cœur du plasma qu'à sa périphérie. Ces gradients entraînent des instabilités dans le plasma. Des structures en rotation cohérentes peuvent résulter de divers mécanismes et instabilités dans les plasmas. Le processus par lequel les instabilités peuvent donner naissance à des structures cohérentes implique probablement une série d'interactions non linéaires et une auto-organisation au sein du plasma.

Le dispositif expérimental standard pour l'étude des plasmas faiblement magnétisés consiste en une colonne de plasma cylindrique immergée dans un champ magnétique axial. MISTRAL est un dispositif de ce type basé au laboratoire PIIM. L'expérience a été conçue pour étudier une colonne de plasma dans une configuration de champs croisés ($\mathbf{E}\perp\mathbf{B}$). Plusieurs mécanismes potentiels, y compris les ondes de dérive, l'instabilité de Rayleigh-Taylor/Centrifuge, l'instabilité de Kelvin-Helmholtz et l'instabilité de entrainement neutre, ont été identifiés comme contribuant potentiellement à la formation des structures en rotation observées dans MISTRAL. Cependant, l'identification des instabilités responsables de leur émergence reste difficile à obtenir.

Plusieurs modèles (voir Chapitre 4) ont été proposés pour étudier l'apparition d'instabilités susceptibles de se transformer en structures en rotation cohérentes auto-organisées. Cependant, la physique qui sous-tend le développement de ces structures n'est pas encore comprise. Le travail effectué dans le cadre de ce doctorat vise à faire progresser notre compréhension de la formation de ces modes de rotation cohérents et du transport radial associé grâce à une modélisation appropriée. Les ondes de dérive, les ondes de Rayleigh-Taylor et les ondes de Kelvin-Helmhlotz se sont avérées responsables du transport radial dans les dispositifs à plasma linéaire [Bro+06], [Gra+04] et [BGB05]. La grande majorité des modèles développés pour décrire ces instabilités reposent sur l'approximation basse fréquence (LFA). L'approximation basse fréquence se réfère ici à l'approximation telle que $\omega - m\omega_0 << \omega_{ci}$ où ω est la partie réelle de la fréquence perturbée, ω_0 est la fréquence du écoulement d'équilibre, m est le nombre de mode azimutal et ω_{ci} est la fréquence cyclotron ionique. Cependant, dans les plasmas faiblement magnétisés comme MISTRAL, RAID et VKP, la fréquence des ondes peut être comparable ou supérieure à ω_{ci}. Cette approximation à basse fréquence (LFA) impose des limites à l'étude de la dynamique réelle du plasma et à la compréhension des instabilités qui peuvent se produire dans le système. En tant qu'étape initiale cruciale vers la compréhension des modes rotatifs cohérents, il est essentiel de développer un modèle qui peut être appliqué sur une large gamme de valeurs de fréquence. Le développement d'un modèle sans cette approximation est donc l'élément clé de ce travail.

Le Chapitre 2 donne une description générale de l'expérience MISTRAL. Cette tous les diagnostics intrusifs et non intrusifs disponibles sur MISTRAL sont présentés. Les

travaux expérimentaux de ce chapitre constituent la base de la modélisation théorique. Quelques conditions expérimentales de référence sont données afin que les lecteurs puissent se faire une idée générale de la façon dont les propriétés du plasma changent dans MISTRAL en fonction de la configuration utilisée. Les profils radiaux moyennés dans le temps de la densité électronique et du potentiel plasma à différentes valeurs de pression et de champ magnétique sont fournis en fonction de la configuration utilisée. On a constaté que le champ électrique agissait radialement vers l'intérieur pour la configuration utilisée. Les profils de densité électronique et de potentiel plasma sont paramétrés à l'aide des relations:

$$n_e(r) = n_{e0}\ exp\left(-\frac{r^2}{r_0^2}\right);\ \ \phi_0 = p_1 r^2 + p_2 \tag{0.1}$$

où n_{e0}, p_1 et p_2 sont des constantes. Ici, r est la coordonnée radiale et r_0 est la largeur de la gaussienne utilisée pour paramétrer le profil de densité ; r_0 caractérise la diminution radial de la densité du plasma. Ces profils d'équilibre sont compatibles avec l'hypothèse de rotation d'un corps rigide utilisée pour l'équilibre (voir le Chapitre 4). Ces paramétrisations fournissent une représentation mathématique permettant le calcul des quantités nécessaires à la modélisation théorique et à l'analyse du plasma.

En outre, le Chapitre 2 étudie l'influence de la pression et du champ magnétique sur la fréquence du mode. On constate que la fréquence du mode diminue avec l'augmentation de la pression, alors qu'elle augmente avec l'intensité du champ magnétique. Deux configurations supplémentaires sont étudiées pour mesurer les fluctuations de densité et de potentiel. Ces résultats peuvent être comparés aux prédictions théoriques du chapitre 5 pour l'identification des instabilités. En outre, les modes m = 1, 2 et 3 peuvent être observés expérimentalement, grâce aux measures de sondes et de caméra rapide.

Une description générale des différents types de modélisation du plasma est ensuite présentée au Chapitre 3. Différents types d'instabilités apparaissant dans les plasmas avec des configurations de champs croisés sont fournis en fonction de leur vecteur d'onde parallèle ($k_\parallel$) : instabilité de type flûte et instabilité d'onde de dérive (voir Fig. 3.2). Ici, $k_\parallel = \mathbf{k}.\mathbf{B}/\mathrm{B}$ représente la composante du vecteur d'onde parallèle à la direction du champ magnétique. Dans le cas des modes flûte, le mouvement dominant se produit perpendiculairement aux lignes de champ magnétique. Par conséquent, $k_\parallel$ est souvent petit ou négligeable par rapport au nombre d'ondes perpendiculaires ($k_\perp$). Les ondes de dérive, en revanche, sont associées à un nombre d'ondes parallèles non nul, c'est-à-dire $k_\parallel > 0$. Un mécanisme général des instabilités couramment observées dans les expériences de plasma en laboratoire est également présenté pour donner une idée de la façon dont ces instabilités se développent.

Une vue d'ensemble des modèles existants pour étudier la stabilité linéaire des plasmas en configuration $\mathbf{E}\times\mathbf{B}$ est présentée. Il est souligné que la plupart des modèles

formulés jusqu'à présent pour étudier les plasmas **E**×**B** sont basés sur l'approximation basse fréquence (LFA) comme expliqué précédemment. En outre, les effets du rayon de Larmor fini (FLRE) et les collisions de particules chargées avec des neutres sont importants pour la modélisation des instabilités du plasma dans ces dispositifs de laboratoire, comme le montre le Chapitre 4.

Afin de construire un modèle approprié pour la description des plasmas MISTRAL, il est nécessaire de connaître les conditions de plasma typiques rencontrées dans l'expérience. Le Chapitre 4 présente les paramètres nécessaires à la modélisation du plasma MISTRAL. Les différentes échelles de temps et de longueur impliquées dans la dynamique du plasma (Table 1) constituent la base d'une modélisation appropriée et permettent de formuler des hypothèses pour le modèle de fluide.

Debye length	λ_D	1.3 mm - 0.13 mm
Ion thermal speed	v_{thi}	692 ms^{-1}
Electron thermal speed	v_{the}	593 kms^{-1} - 1027 kms^{-1}
Ion Larmor radius	ρ_i	18 mm
Electron Larmor radius	ρ_e	0.2 mm - 0.4 mm
Ion plasma frequency	ω_{pi}	0.53 MHz - 5.3 MHz
Electron plasma frequency	ω_{pe}	0.46 GHz - 7.9 GHz
Ion-neutral collision frequency	ν_{in}	0.18 kHz - 17.9 kHz
Electron neutral collision frequency	ν_{en}	24 kHz - 2.4 MHz
Electron-ion Coulomb collision frequency	ν_{ei}^C	760 Hz - 76 kHz
Electron-electron Coulomb collision frequency	ν_{ee}^C	760 Hz - 76 kHz
Ion-Ion Coulomb collision frequency	ν_{ii}^C	125 Hz - 10.6 kHz
Plasma column length	L	1 m
Cylinder radius	R	10 cm
Ionization rate	-	$< 1\%$

Table 1.: Échelles de longueur et de temps typiques dans le plasma MISTRAL. Pour calculer la gamme de λ_D, n varie de $10^{14} - 10^{16}$ m^{-3} comme indiqué dans le tableau 4.1 et $T_e \approx 3$ eV est utilisé.

Les informations données dans le tableau 1 montrent que le plasma étudié est quasi-neutre. Les électrons peuvent être considérés comme fortement magnétisés tandis que les ions sont faiblement magnétisés. Les hypothèses sont utilisées pour modéliser les plasmas de MISTRAL.

Un formalisme à deux fluides est ensuite utilisé pour étudier la stabilité des colonnes de plasma en rotation faiblement magnétisées. Nous considérons un plasma cylindrique limité radialement et immergé dans un champ magnétique homogène tel que $\mathbf{B} = B\,\hat{e}_z$. Sur la base des caractéristiques expérimentales de MISTRAL et des conditions de plasma discutées ci-dessus, nous faisons les hypothèses suivantes:

- L'approximation électrostatique est utilisée de telle sorte que $\frac{\partial B}{\partial t} = 0$.

- Le champ magnétique est uniforme le long de la direction axiale, c'est-à-dire $\mathbf{B} = B\hat{e}_z$.
- Les fluctuations le long de la direction axiale sont négligées, c'est-à-dire que $k_\parallel = 0$.
- Profil parabolique pour le potentiel du plasma, cette hypothèse n'est pas valable à haute pression.
- La température des ions T_i est supposée être radialement uniforme. La température des électrons varie radialement suivant une distribution gaussienne telle que $T_e = T_{e0}\ exp\ \left(-r^2/r_0^2\right)$.

- Pour conserver un modèle traitable analytiquement, la viscosité gyroscopique est négligée: $\nabla\cdot\pi_i = 0,\ \nabla\cdot\pi_e = 0$.
- L'inertie des électrons est négligée en raison de la faible masse des électrons par rapport aux ions, $m_e/m_i \ll 1$.
- Les collisions neutres dominent les collisions de Coulomb pour les régimes rencontrés dans MISTRAL [Ann+11], [Pie16] où $\nu_{ei}, \nu_{eiC}, \nu_{en}/\omega_{ce} \ll 1$.
- Quasineutralité, $n_i = n_e$.
- Rotation d'équilibre du corps rigide.

Sur la base de ces hypothèses, l'équation de continuité pour la $j$ième espèces est,

$$\frac{\partial n_j}{\partial t} + \nabla\cdot(n_j\mathbf{v}_j) = 0 \tag{0.2}$$

L'équation de la quantité de mouvement pour les ions et les électrons est:

$$n_i m_i\left[\frac{\partial \mathbf{v}_i}{\partial t} + (\mathbf{v}_i\cdot\nabla)\mathbf{v}_i\right] = en_i\left(-\nabla\phi + \mathbf{v}_i\times\mathbf{B}\right) - T_i\nabla n_i - m_i n_i \nu_{in}\mathbf{v}_i \tag{0.3}$$

$$0 = -en_e(-\nabla\phi + \mathbf{v}_e\times\mathbf{B}) - \nabla(n_e T_e) \tag{0.4}$$

Le système est fermé en supposant T_e et T_i constants dans le temps. Le système d'équations donné est ensuite linéarisé. Pour la linéarisation, la densité du plasma, l'écoulement et le potentiel électrique sont écrits comme la somme d'une partie d'équilibre indépendante du temps désignée par l'indice 0 et d'une partie fluctuante désignée par l'exposant $\sim$ comme, $n = n_0 + \tilde{n}$, $\mathbf{v} = \mathbf{v}_0 + \tilde{\mathbf{v}}$ et $\phi = \phi_0 + \tilde{\phi}$ où la partie fluctuante a la forme suivante :

$$\begin{aligned}
\tilde{n} &= n_1(r)\ exp[i(m\theta - \omega t)] \\
\tilde{\mathbf{v}} &= \mathbf{v}_1(r)\ exp[i(m\theta - \omega t)] \\
\tilde{\phi} &= \phi_1(r)\ exp[i(m\theta - \omega t)]
\end{aligned} \tag{0.5}$$

Ici, n_0 est la densité d'équilibre des ions ou des électrons, ϕ_0 est le potentiel électrique d'équilibre et $\mathbf{v_0}$ est l'écoulement d'équilibre. Pour la partie fluctuante, n_1 et ϕ_1 donnent l'amplitude de perturbation de la densité et du potentiel respectivement, $\mathbf{v}_1(r) = v_{r_1}\hat{e}_r + v_{\theta_1}\hat{e}_\theta$ avec v_{r1} et $v_{\theta 1}$, la composante radiale et azimutale de la vitesse perturbée, m est le nombre de modes azimutaux et $\omega = \omega_r + i\gamma$ où ω_r est la fréquence du mode et γ le taux de croissance.

La densité d'équilibre (n_0) et le potentiel du plasma (ϕ_0) sont supposés avoir des profils gaussiens et paraboliques, respectivement. Ceci est compatible avec les profils typiques mesurés dans MISTRAL comme donné par l'équation 0.1.

L'écoulement d'équilibre pour les ions et les électrons est ensuite étudié en utilisant la partie d'ordre zéro de l'équation de quantité de mouvement linéarisée des ions (Eq. 0.3) et des électrons (Eq. 0.4) respectivement. Nous obtenons pour les ions:

$$4\left(\bar{\omega}_0 + \frac{1}{2}\right)^4 - \left(1 - \bar{\nu}_{in}^2 + 4(\bar{\omega}_{E0} + \bar{\omega}_{*0})\right)\left(\bar{\omega}_0 + \frac{1}{2}\right)^2 - \frac{\bar{\nu}_{in}^2}{4} = 0 \tag{0.6}$$

qui est une équation bi quadratic en $\bar{\omega}_0$ dont les solutions sont données par:

$$\bar{\omega}_0 = \pm\frac{1}{2}\sqrt{\frac{1}{2}\left[b + \sqrt{b^2 + 4\bar{\nu}_{in}^2}\right]} - \frac{1}{2} \tag{0.7}$$

où $b = 1 + 4(\bar{\omega}_{*0} + \bar{\omega}_{E0}) - \bar{\nu}_{in}^2$.

Ici, ω_{E0} est la fréquence de dérive $E \times B$:

$$\omega_{E0} = \frac{\mathbf{B} \times \nabla\phi_0}{rB^2} \cdot \hat{e}_\theta = \frac{\phi_0'}{rB} \tag{0.8}$$

et ω_{*0} est la fréquence de dérive diamagnétique de l'ion:

$$\omega_{*0} = \frac{T_i}{en_0B}\frac{\mathbf{B} \times \nabla n_0}{rB} \cdot \hat{e}_\theta = \frac{T_i}{erB}\frac{n_0'}{n_0} \tag{0.9}$$

$$= -\frac{T_i}{erB}\frac{1}{L_n} \tag{0.10}$$

où $1/L_n = -n_0'/n_0 = 2r/r_0^2$ est le gradient de densité logarithmique. Il convient de noter que ω_{E0} et ω_{*0} sont indépendants de r en raison du choix de n_0 et ϕ_0 donné par l'équation (0.1).

L'écoulement d'électrons à l'équilibre est:

$$\bar{v}_{e\theta_0} = \bar{r}\bar{\omega}_{0e} \quad \text{with} \quad \bar{\omega}_{0e} = \bar{\omega}_{E0} + \bar{\omega}_{*e} \tag{0.11}$$

où $\bar{\omega}_{0e}$ est la fréquence du écoulement d'équilibre des électrons et $\bar{\omega}_{*e}$ est la fréquence

de dérive diamagnétique des électrons ω_{*e} normalisée à la fréquence du cyclotron ionique, avec:

$$\omega_{*e} = -\frac{1}{en_0B}\frac{\mathbf{B}\times\nabla(n_0T_{e0})}{rB}\cdot\hat{e}_\theta \tag{0.12}$$

La plage de la fréquence d'écoulement d'équilibre est déterminée en utilisant les valeurs de ω_{E0}, ω_{*0} et ν_{in}. Pour estimer la gamme de la fréquence de dérive $\mathbf{E}\times\mathbf{B}$ (ω_{E0}) et la fréquence de dérive diamagnétique des ions (ω_{*0}), on utilise les paramètres p_1 et r_0 obtenus par la paramétrisation des profils de densité et de potentiel correspondant aux cas de référence A et B dans le Chapitre 2. Ils sont ensuite utilisés dans les équations suivantes pour trouver la gamme de fréquences désirée:

$$\omega_{E0} = \frac{2p_1}{B};\ \ \omega_{*0} = -\frac{2T_i}{eBr_0^2} \tag{0.13}$$

La gamme de ν_{in} qui est pertinente pour la colonne de plasma MISTRAL a déjà été donnée dans la section 4.1.2 du Chapitre 2. La gamme des diverses fréquences est ensuite calculée pour différentes valeurs de champ magnétique et de pression, comme le montre la figure 1.

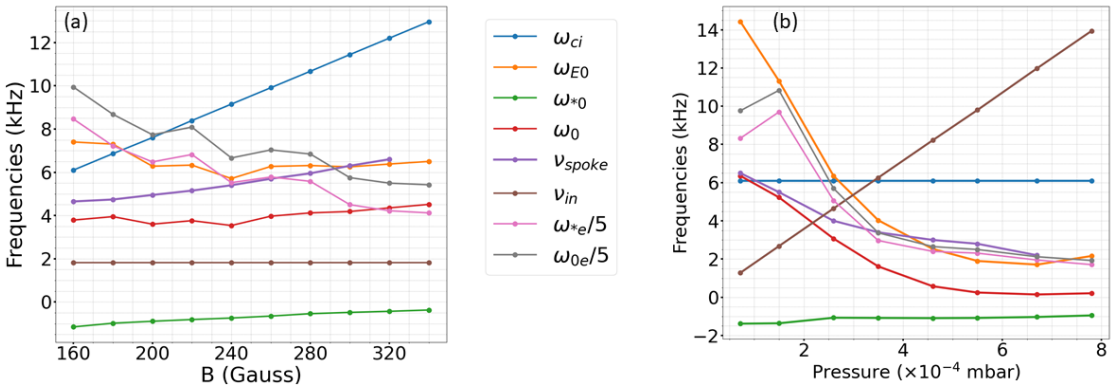

Figure 1.: Variation de la fréquence du cyclotron ionique (ω_{ci}), de la fréquence de dérive $\mathbf{E}\times\mathbf{B}$ (ω_{E0}), de la fréquence de dérive diamagnétique ionique (ω_{*0}), de la fréquence de l'écoulement d'équilibre (ω_0), de la fréquence de l'instabilité en rotation (ν_{spoke}), de la fréquence de collision ion-neutre (ν_{in}), de la fréquence de dérive diamagnétique des électrons (ω_{*e}) et de la fréquence de l'écoulement d'équilibre des électrons (ω_{0e}) pour diverses (a). intensités de champ magnétique et (b). valeurs de pression. Voir Fig. 4.10 et Fig. 4.11 pour plus de détails.

La figure 1 montre clairement que l'approximation basse fréquence selon laquelle $\omega_0 << \omega_{ci}$ et $\nu_{spoke} << \omega_{ci}$ n'est pas valable pour le système de plasma considéré. Par conséquent, il est impératif de considérer les termes d'ordres supérieurs qui ont été négligés dans les modèles précédents pour comprendre pleinement la stabilité linéaire des colonnes de plasma faiblement magnétisées, ce qui est expliqué en détail dans le Chapitre 5 de la thèse.

Pour dériver la relation de dispersion qui donne des informations sur le taux de croissance et la fréquence des modes existants, nous avons d'abord linéarisé les équations de quantité de mouvement pour les ions et les électrons et les avons couplées avec leurs équations de continuité respectives pour établir une relation entre la densité normalisée perturbée ($\bar{n}_1$) et le potentiel normalisé perturbé ($\bar{\phi}_1$). En couplant ensuite l'hypothèse de quasi-neutralité et la relation $\Phi_1 = \bar{n}_1 + \tau\bar{\phi}_1$, on obtient une équation différentielle linéaire pour le cas sans collision,

$$\Phi_1'' + \left[\frac{1}{\bar{r}} - \frac{1}{\bar{L}_n}\right]\Phi_1' - \frac{m^2}{\bar{r}^2}\Phi_1 + \frac{1}{\bar{r}\bar{L}_n}N\Phi_1 = 0 \tag{0.14}$$

où

$$N = m\left[\frac{C}{\bar{\omega}_{ph}} - \frac{C^2 - \bar{\omega}_{ph}^2}{\bar{\omega}_{ph} - m\bar{\omega}_0^2}\right] \tag{0.15}$$

La solution de l'équation différentielle est obtenue en utilisant la fonction de Kummer qui satisfait une équation différentielle linéaire spécifique du second ordre appelée équation de Whittaker. La détermination de la valeur de N à l'aide de la fonction de Kummer permet de résoudre la relation de dispersion cubique. Cette relation de dispersion permet de comprendre le comportement global du système considéré.

L'hypothèse LFA étant l'élément clé de nombreux travaux existants, le domaine de validité de la LFA en fonction de ω_0/ω_{ci} est mis en évidence dans la figure 2 où la solution sans la LFA (Eq. (0.15)) est comparée à la solution avec la LFA (Eq. 5.39).

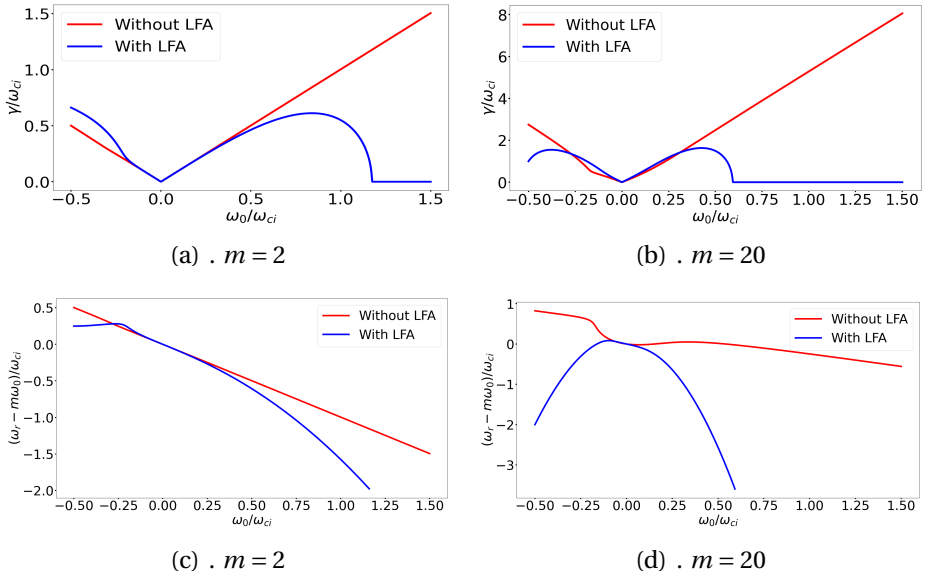

(a) . $m = 2$ (b) . $m = 20$

(c) . $m = 2$ (d) . $m = 20$

Figure 2.: Taux de croissance normalisé γ/ω_{ci} et fréquence décalée Doppler normalisée $(\omega_r - m\omega_0)/\omega_{ci}$ en fonction de la fréquence d'équilibre normalisée (ω_0/ω_{ci}) pour (a,c). $m = 2$ et (b,d). $m = 20$ pour $Z = 10.78$. Pour plus de détails, voir Fig. 5.8 au Chapitre **??**.

En outre, les dépendances paramétriques du taux de croissance normalisé et de la fréquence Doppler normalisée sont étudiées. Le taux de croissance et la fréquence des différents modes sont fortement influencés aux petites valeurs de r_b^2/r_0^2 en fonction de la direction de la fréquence d'écoulement d'équilibre. Dans la limite où la paroi conductrice est éloignée du plasma, $\left(\frac{r_b^2}{r_0^2} >> 1\right)$, le taux de croissance du mode le plus instable est $\bar{\gamma} = |\bar{\omega}_0|\sqrt{m-1}$ avec la fréquence Doppler correspondante comme $\bar{\omega}_r - m\bar{\omega}_0 = -\bar{\omega}_0$ qui est indépendante du nombre de mode azimutal m. Dans cette limite, le mode $m = 1$ est stable. Lorsque le rayon du cylindre conducteur est réduit, le taux de croissance des modes augmente d'abord, y compris celui du mode $m = 1$ qui devient instable avant que la stabilisation complète de tous les modes ne soit obtenue. On constate que le taux de croissance augmente avec le nombre de modes azimutaux. Ceci est, au moins, dû à la négligence des effets FLR qui sont pris en compte en incluant le tenseur de gyroviscosité dans l'équation de la quantité de mouvement de l'ion. L'inclusion des effets FLR stabiliserait tous les modes dont la longueur d'onde est inférieure au rayon de Larmor de l'ion. Pour les paramètres considérés ici, les modes avec des nombres de modes azimutaux $m > 5$ devraient être stabilisés en raison des effets FLR.

En ce qui concerne la structure des modes, les modes à faible nombre m sont plus étalés radialement que ceux à nombre m élevé. Pour un numéro de mode fixe, plus le rayon du cylindre augmente, plus le mode est poussé vers le bord du cylindre. Pour un rayon du cylindre fixe, la différence de phase entre les fluctuations de densité normalisées et les fluctuations de potentiel peut prendre n'importe quelle valeur en fonction de la valeur du nombre de modes, de la fréquence d'écoulement d'équilibre, de la fréquence d'écoulement $\mathbf{E}\times\mathbf{B}$, du paramètre $\bar{r}_0$ et de la limite radiale $\bar{r}_b$. La différence de phase était plus proche de 90° dans les régions où la fréquence perturbée normalisée $(\bar{\omega}_r)$ s'approche de $m\bar{\omega}_{E0}$. En outre, la valeur critique de $\bar{\omega}_{E0}$, à laquelle le déphasage passe de négatif à positif, augmente à mesure que $\bar{r}_0$ diminue. Les prévisions théoriques de l'amplitude des fluctuations du potentiel normalisé par rapport à la densité et de la différence de phase ont également été comparées aux résultats expérimentaux. Certaines divergences ont été constatées dans la comparaison, car le modèle ne tient pas compte de la collisionnalité, qui est élevée dans le plasma MISTRAL et peut éventuellement affecter ces résultats. En outre, les mesures expérimentales correspondent à l'état non linéaire alors que le modèle est linéaire.

La comparaison des solutions locales et globales de la relation de dispersion a révélé que les effets globaux jouent un rôle critique dans toutes les gammes de paramètres. La relation de dispersion locale, qui simplifie l'analyse en négligeant les effets de conditions aux limites et les variations spatiales, prédit un taux de croissance maximal près de l'axe du plasma ou de la frontière extérieure. Ces effets de frontière et ces variations spatiales introduisent une physique supplémentaire qui ne peut pas être capturée de manière adéquate par le modèle local.

Compte tenu de la fréquence relativement élevée des collisions ion-neutre dans le système plasmatique actuel, il devient crucial de tenir compte de l'influence de la collisionnalité sur le comportement de l'instabilité. Au Chapitre 6, une relation de dispersion globale est dérivée dans la limite de $\epsilon \to 0$, où $\epsilon = \bar{\nu}_{in}\bar{\omega}_0/C$. Cette étape nous permet d'examiner l'impact de la collisionnalité sur le comportement de l'instabilité. Pour faciliter cette analyse, nous comparons le taux de croissance et la fréquence perturbée obtenus à l'aide de diverses relations de dispersion globales, en incorporant dans tous les cas les effets de la force de Lorentz et du gradient de pression. Les comparaisons portent sur des cas avec effets inertiels, effets inertiels combinés à des collisions et, enfin, collisions uniquement. Ces comparaisons nous permettent de mieux comprendre comment les différents termes de l'équation du moment cinétique de l'ion contribuent à la modification du comportement de l'instabilité et à la dominance relative d'un effet par rapport à un autre.

Enfin, les conclusions sont présentées au chapitre 7 pour résumer les principaux résultats de ce travail. Malgré cela, il reste encore de nombreuses questions ouvertes qui sont présentées à la fin de la thèse.

List of Figures

List of Tables

Frequently used Symbols

ϵ_0	Vacuum permittivity
μ_0	Vacuum permeability
j=i,e,n	Species type - i for ions, e for electrons and n for neutrals
n_j	density of the species j
T_j	Temperature of the species j
m_j	mass of the species j
E, **B**	Electric and magnetic field vector
V_p	Plasma potenial
V_f	Floating potential
e	electronic charge
v_j	velocity of species j
ρ_i	Ion larmor radius
v_{th_j}	thermal velocity of species j
ω_{ci}	Ion-cyclotron frequency
ω_{ce}	Electron-cyclotron frequency
$1/L_n$	Density gradient scale length
β	Plasma beta (ratio of plasma pressure to the magnetic pressure)
γ	Linear mode growth rate
λ_D	Debye length
ν_{jk}	Collision frequency between two species j and k
ω_0	Ion equilibrium flow frequency
ω_r	Real frequency of the Linear Fourier modes

ω_{*0}	Ion diamagnetic frequency
ω_{*e}	Electron diamagnetic frequency
ω_{0e}	Electron equilibrium flow frequency
ω_{E0}	**E**×**B** drift frequency
$\omega_{pi,e}$	Ion, electron Plasma frequency
f_j	Distribution function of the species **j**
r	radial coordinate
r_b	radial boundary
m	azimuthal mode number
n	radial mode number

1. Introduction

What is plasma? This question is addressed in many textbooks but there are still numerous questions related to plasmas that remain unresolved. This thesis represents a modest attempt to address one of those questions. Before getting into the specifics of the issue, a general description of plasmas will be given. This can aid a beginning reader in grasping the fundamentals. The general description of the plasma will be followed by the practical applications and finally the thesis's major objective.

From the scientific point of view, matter is often classified in terms of four states: solid, liquid, gas, and plasma. It is the strength of the bonds holding the constituent particles together that draws a line of distinction among solids, liquids, and gases. In solids, binding forces are relatively strong, weak in liquids, and almost absent in gases. Whether a given system is found in one of these states depends on the random kinetic energy of its atoms and molecules, i.e. on its temperature. When a sufficient amount of energy is provided such that the thermal kinetic energy of the particles exceeds the molecular binding energy, molecular gas will gradually dissociate into atomic gas due to collisions among the particles. With sufficiently high temperatures, collisions among the atoms increase and an increasing fraction of atoms possess enough kinetic energy to overcome the binding energy of the outermost orbital electrons, and an ionized gas or "PLASMA" results. However, this transition is not a phase transition, rather it occurs gradually with increasing temperature, typically of the order of 10,000 K. Plasma maintains its electrical neutrality down to very small scales. This is made possible by the potent electric forces created by the localized charge imbalance.

W. Crookes [Cro79] in 1987 first coined the term "fourth state of matter" to describe the ionized medium created in the gas discharge often used to describe the plasma state [KT73]. The word plasma comes from the Greek word which means 'something molded'. About 99% of the universe is found to be in the plasma state. As one leaves the Earth's atmosphere, one encounters the plasma comprising the Van Allen radiation belts, the solar winds, nebulae, and stars (Fig. 1.1). In everyday life, encounters with plasma are limited to a few instances, like, the flash of a lightning bolt, lightning of a fluorescent tube, Aurora borealis, etc. We live in the 1% of the universe where plasma does not occur naturally. Although in gas, there is always some small degree of ionization present, it cannot be called as plasma. Basically, plasma is a quasineutral gas of charged and neutral particles which exhibits collective behavior [Che16]. The term quasi-neutral refers to a condition in which plasma is considered neutral enough (at a macroscopic scale) such that $n_e \approx n_i$ approximately holds but not neutral enough that all electromagnetic forces vanish. Here n_e refers to the electron density and n_i

refers to the ion density.

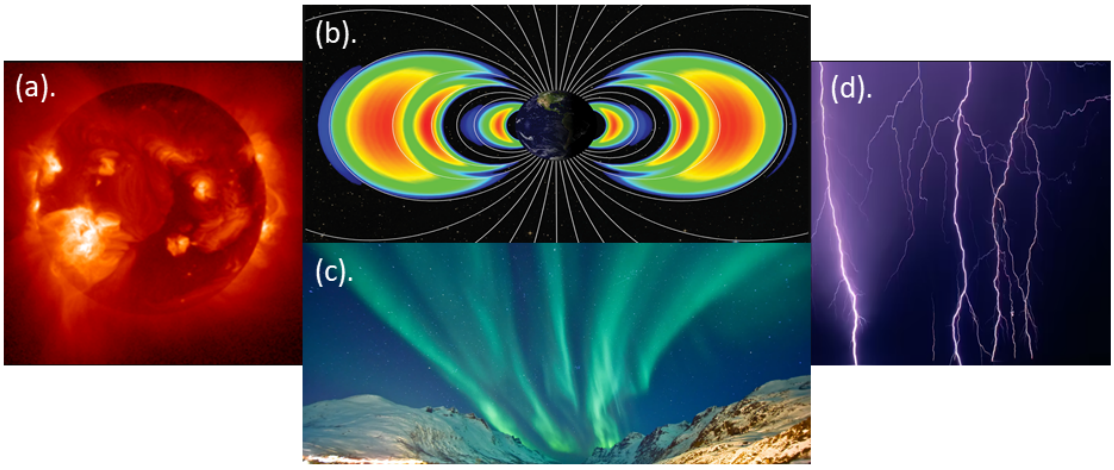

Figure 1.1.: Image of (a).Sun's Corona [Courtesy: Nasa's website]. (b). Van Allen radiation belt around earth [Courtesy: Nasa's website]. (c). Aurora borealis and (d). Lightning during a thunderstorm.

Plasma is characterized by three fundamental parameters [Bel06]:

- the particle density n (measured in particles per cubic meter),
- the temperature T of each species (usually measured in eV, where 1 eV=11,605 K),
- the steady-state magnetic field B (measured in Tesla) and electric field E (measured in V/m).

These three fundamental parameters can be used to determine a wide range of additional parameters, including Debye length, Larmor radius, plasma frequency, cyclotron frequency, and thermal velocity (see Chapter 4).

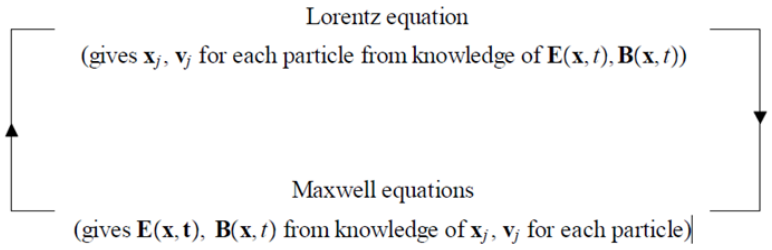

Figure 1.2.: Interrelation between Maxwell's equations and the Lorentz equation. Source[Bel06]

The electromagnetic fields present within the plasma system have a significant influence on the dynamics of charged particles. These fields can be self-generated resulting from the motion of charged particles or can be applied from external sources as well, such as electric and magnetic fields. These electromagnetic fields accelerate the

charged particles which result in the change of their trajectories. Fig. 1.2 presents how the particle trajectories are interconnected with the electromagnetic fields through Lorentz and Maxwell's equations. There are plenty of references available if one wants to learn more about those quantities and how to get their literal expression including [Che16], [LL05], and [Den93].

1.1. Plasma devices and their applications

Numerous plasma devices are available with different characteristics and can be categorized depending on their applications and plasma properties. For instance, plasma regimes can be classified as high or low-temperature plasmas, magnetized or non-magnetized plasmas, fully or partially-ionized plasmas, low or high (atmospheric) pressure plasmas, and so on.

As an example, plasma surface treatment methods allow for the creation of products with considerably greater hardness, enhanced corrosion resistance, biocompatibility, and altered optical and electrical properties [VG21]. A significant plasma application is the creation of integrated circuits (ICs), which accounts for about 1/3 of the processes in semiconductor production. Then there are plasma sterilizers, which use low-temperature plasma to sterilize medical tools and equipment, ensuring the destruction of pathogens such as bacteria and viruses [AYT19]. Plasma torches [Zai+23] are used in metalworking applications, such as welding, brazing, and soldering. They produce an intense and concentrated heat source that can melt and join metals. Plasma mass separators [Gue+19] use plasma physics principles to separate ions based on their mass differences. The basic technique involves generating a plasma, ionizing the gas containing the constituents to be separated, accelerating the ions using electric and/or magnetic fields, and then separating the constituents based on their mass-to-charge ratio.

In the context of space applications, the Hall thruster [Ada+08] is one of the applications of plasma physics where a propellant gas is ionized to form a plasma. The plasma is then accelerated and controlled by electromagnetic fields, creating a high-velocity plasma jet that provides thrust for spacecraft propulsion.

On a larger scale, the tokamak is a device that has proven to be capable of reaching high densities ($\approx 10^{20}\ m^{-3}$) and temperatures (≈10 keV) for a sufficiently long time (≈ 1s) to produce large amounts of fusion reactions [WC04]. A tokamak is a device that uses magnetic fields to constrict a plasma into a donut-shaped structure known as a torus (see Fig. 1.3), to reach the conditions required for fusion. A powerful "toroidal" field is produced by one set of magnetic coils and is directed circumferentially around the torus (in blue). A second magnetic field is produced indirectly by a central solenoid, by inducing a current in the toroidal direction. This current carried by the plasma generates a magnetic field along the "poloidal" direction, which is the

short path around the torus (in green). The two field components produce a twisted magnetic field that ensures good plasma confinement (in black). An outer poloidal field created by a third set of field coils is used for the vertical stability and shaping of the plasma volume (in grey).

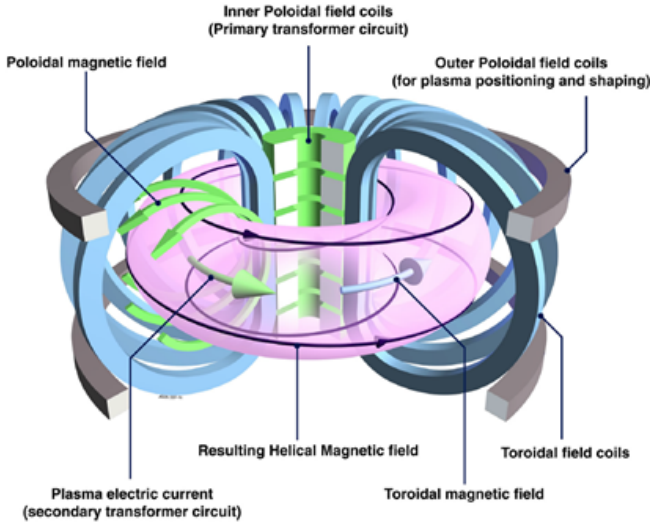

Figure 1.3.: Schematic of the Tokamak configuration. [Image Courtesy: Eurofusion]

1.2. Instabilities, turbulence, and transport in magnetized plasmas

In most of the devices and configurations discussed above, an external magnetic field is applied for plasma confinement, thus insulating it from the walls and reducing energy losses so that the plasma can be heated to achieve high temperature, e.g. such as that required for thermonuclear reaction for fusion applications. In low-temperature plasma systems, the magnetic field can be utilized to confine electrons, thereby sustaining the necessary electron temperature for the ionization of neutral gas. This tends to generate large gradients, e.g. a larger pressure in the core of the plasma than at the edge. These gradients drive plasma instabilities. For example, above a threshold in pressure gradient, instabilities grow and start to interact leading to turbulence. The associated turbulent transport will limit/decrease the gradients and the plasma reaches a dynamic equilibrium.

Rotating coherent structures which are assumed to be formed as a result of the manifestation of instabilities, have been observed in Hall thrusters [Sek+15] where they are called “spokes” and limit the performance of the device. The word “spoke” in the context of low-temperature $\mathbf{E} \times \mathbf{B}$ plasmas, is generally used to refer to the region

of a local enhancement of the plasma density. Coherent structures resulting from plasma self-organization are also observed in tokamak plasmas [Dif+15]. There is a need for a better understanding of the mechanisms leading to the formation of these structures and their relationship with plasma instabilities and transport.

The next section offers a brief description of one class of devices designed to investigate the fundamental mechanisms of plasmas in a controlled setting and a relatively simpler geometry than large-scale toroidal devices.

1.3. Magnetized linear devices to study plasma dynamics

Coherent rotating structures can arise from various instabilities (see Chapter 4) and mechanisms in plasmas. The process by which instabilities can give rise to coherent structures possibly involves a series of nonlinear interactions and self-organization within the plasma system. Understanding the formation of these large-scale structures in weakly magnetized plasmas (here weakly magnetized is understood as a plasma radius of typically 3 to 30 ion Larmor radii (ρ_i)) is of particular interest for both fundamental research and technological applications (magnetrons [Abo12], Penning discharges [Tyu+23], negative ion sources, space propulsion devices [ERF12], [Sek+15]).

A canonical configuration for the study of weakly magnetized plasmas is a cylindrical plasma column immersed in an axial magnetic field (see Fig. 1.4). Linear devices have an advantage over tokamaks because they can give a better grasp of the fundamental characteristics and behavior of plasmas. In comparison to tokamaks, which are significantly more difficult and expensive to build and run, linear devices are simpler and more adaptable in terms of their design and operation. This simplicity facilitates diagnostics and measurements of plasma parameters. It also simplifies the understanding and modeling of plasma behavior as the magnetic field is applied along the axial direction, therefore, the curvature drifts [Che16] arising due to the curved magnetic field can be neglected. Moreover, the plasma discharge can be run for a long time in these devices without the problem of damaging the diagnostics and the device.

With the aid of recent advancements in theory and technology, numerous linear devices have been examining the physics of coherent rotating structures during the past few years [Man+11],[Fre+03],[AYT07],[Mat+03]. Out of the numerous linear devices that are available worldwide to study $\mathbf{E} \times \mathbf{B}$ plasmas, the dimensions, control parameters, and source configuration of three devices MISTRAL [A E10], RAID [Fur+17], and VKP [Pli+14] are given in Table 1.1.

The plasma is generated in these three devices with two methods namely Thermionic

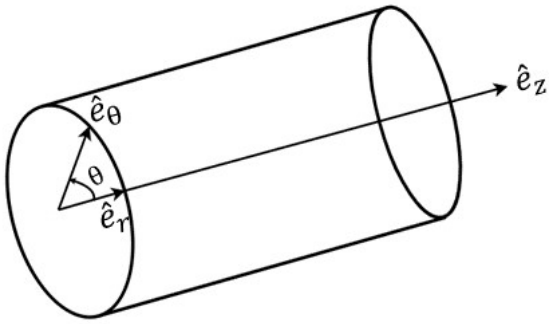

Figure 1.4.: Cylindrical geometry with the cylindrical coordinate system. $\hat{e}_r$ denotes the unit vector in radial direction, $\hat{e}_\theta$ denotes the unit vector in azimuthal direction and $\hat{e}_z$ denotes the unit vector in axial direction.

discharge (in MISTRAL) and Helicon wave source (in VKP and RAID). Thermionic discharge is a kind of DC discharge in which the electrons are emitted from a heated cathode via thermionic emission [LL05]. After being accelerated towards an anode, the electrons create a discharge and form a plasma column in a cylindrical chamber filled with a gas. The ionization of gas particles due to emitted electrons results in plasma formation.

The helicon wave source is a type of radio frequency (RF) plasma source [LL05]. It utilizes a helical antenna or coil to generate a helicon wave, a form of electromagnetic wave that propagates through a cylindrical chamber filled with low-pressure gas. A plasma column is formed along the axis of the cylinder by the helicon wave coupling with the electrons in the gas.

Device	Source	Length(m)	Radius(cm)	P(mbar)	T_e (eV)	T_i(eV)	B(mT)	$n_e(m^{-3})$
MISTRAL	TD	1	10	$10^{-3}-10^{-5}$	1-6	~0.1	10-36	$10^{14}-10^{16}$
VKP	HW	0.8	10	$10^{-2}-10^{-4}$	3-5	0.1-1.2	3.5-160	$\sim 10^{18}$
RAID	HW	1.5	20	$10^{-2}-10^{-4}$	1-10	~0.1	5-80	$10^{16}-10^{19}$

Table 1.1.: Charactersitics of different linear devices available. Here TD refers to thermionic discharge and HW refers to the helicon wave source used to generate plasma in the given devices. Length represents the axial length and Radius refers to the radius of the linear plasma column. P and B denote the pressure and magnetic field respectively under which the given devices can be operated. T_e, T_i and n_e denotes the range of electron temperature, ion temperature, and electron density respectively achievable in the given devices.

The devices listed in Table 1.1 differ in experimental configuration and the range of plasma parameters. The existence of large-scale structures has been indicated in these devices [A E10], [Fub+21], [Pli+15] where the azimuthal spoke frequency and azimuthal ion flow frequency can be typically comparable to the ion-cyclotron frequency ω_{ci}.

1.4. Thesis motivation and Outline

To investigate the occurrence of the instabilities which possibly develop into self-organized coherent rotating structures, several models (see Chapter 4) have been proposed. The entire physics behind the development of these structures, however, is still not entirely understood. The work done in this Ph.D. aims to advance our understanding regarding the formation of these coherent rotating modes and the associated radial transport with appropriate modeling. Drift waves, Rayleigh-Taylor waves, and Kelvin-Helmhlotz waves have been found to be responsible for radial transport in linear plasma devices [Bro+06], [Gra+04] and [BGB05]. The large majority of the models developed to describe these instabilities rely on low-frequency approximation (LFA). Here LFA refers to the approximation such that $\omega - m\omega_0 << \omega_{ci}$ where ω is the real part of perturbed frequency, ω_0 is the equilibrium flow frequency, m is the azimuthal mode number and ω_{ci} is the ion-cyclotron frequency. However, in weakly magnetized plasmas produced in devices like MISTRAL, RAID, and VKP, the wave frequency can be comparable to or greater than ω_{ci}. This low-frequency approximation (LFA) imposes limitations on the study of actual plasma dynamics and the understanding of instabilities that may occur within the system. As a crucial initial step towards comprehending coherent rotating modes, it is essential to develop a model that can be applied across a wide range of frequency values. This is the purpose of the thesis which is organized as follows.

Chapter 2 starts with the description of the MISTRAL experiment. The characterization of the plasma column with the rotating spoke is done using the Langmuir probe diagnostic. The obtained characteristics provide a comprehensive range of MISTRAL plasma parameters. The effect of magnetic field and pressure on the spoke frequency is documented. The collected data serve as an essential input for the development and refinement of the theoretical fluid model, which aims to provide an explanation of the observed phenomena.

In Chapter 3, a discussion of various instabilities responsible for turbulent transport and the development of coherent rotating structures in linear plasma columns is provided. An overview of different models to study plasma dynamics in cross-field configuration ($\mathbf{E}\perp\mathbf{B}$) is also presented, offering a deeper understanding of the theoretical frameworks employed in the field.

Chapter 4 focuses on determining the range of essential plasma characteristics, including Larmor radii, cyclotron frequencies, and collision frequencies in MISTRAL plasma. These parameters play a crucial role in understanding the plasma behavior and formulating an accurate model. Various assumptions made during the development of the two-fluid model are validated. Then the two-fluid model based on these assumptions is developed for the plasma system under investigation. The equilibrium flow for ions and electrons is discussed.

In Chapter 5, the global dispersion relation without ion-neutral collision frequency is derived. Additionally, the dispersion relation in the local limit and in the limit of LFA is presented. Then the linear stability of the MISTRAL plasma column using the derived dispersion relation is discussed. The effect of LFA is highlighted and the emphasis on the removal of LFA is made. The solution of the local dispersion relation is compared to the global solution of the dispersion relation without LFA. The parametric dependencies of growth rate and perturbation frequency are also discussed.

Chapter 6 deals with dispersion relation including ion-neutral collisions in the limit $\epsilon \to 0$ with $\epsilon = \bar{\nu}_{in}\bar{\omega}_0/C$. The impact of ion-neutral collisions on the growth rate and frequency of the existing modes is then analyzed. In addition, we compare the growth rate and perturbed frequency obtained using various global dispersion relations, incorporating the effects of Lorentz force and pressure gradient in all cases. The comparisons cover cases with inertial effects, inertial effects combined with collisions and, finally, collisions only. These comparisons enable us to better understand how the different terms of the ion momentum equation contribute to the modification of instability behavior and the relative dominance of one effect over another.

Finally, Chapter 7 highlights the key findings from the thesis and provides an outlook on possible future developments.

2. Observation of rotating spokes in the MISTRAL plasma column

A general description of the linear plasma column experiment MISTRAL along with the various diagnostics accessible is given. Characterization of the plasma column is done by measuring the radial profiles of various plasma parameters at different pressure and magnetic field values. Additionally, the effect of pressure and magnetic field variation on the spoke frequency and parity is documented.

2.1. Description of the MISTRAL device

MISTRAL is an experimental device based at PIIM laboratory to study instabilities and the associated transport in **E**×**B** plasmas. It can be placed in the category of magnetized linear plasma devices. In these devices, plasma is confined in a cylindrical chamber surrounded by magnetic coils that create a magnetic field parallel to the axis of the chamber. The magnetic field serves to confine the plasma by influencing the motion of the charged particles within the plasma. The schematic of MISTRAL is shown in Fig. 2.1. It is divided in two parts mainly: a source chamber and the study chamber (cylindrical plasma column) (Fig. 2.1).

2.1.0.1. The source chamber

The source chamber consists of 32 tungsten filaments powered by a current of approximately 4 A each, emitting primary electrons by thermionic emission. After being emitted, the electrons are attracted by the anode, a honeycomb-shaped structure placed inside the source chamber and electrically isolated from the chamber's wall. The chamber's wall is at the ground. Hundreds of permanent ferrite magnets having a magnetic field in the range of 80-100 mT are fixed on this anode. Each magnet has an opposite polarity as compared to its nearest neighbor. This creates a local magnetic cusp configuration and prevents the emitted electrons from reaching the anode before creating a plasma in the source chamber or before being injected into the study chamber.

To have a homogenous plasma inside the linear column, two compensating coils around the source chamber prevent the electrons from following the magnetic field lines after entering the linear plasma column. These coils create a magnetic subfield in the direction opposite to the magnetic field along the linear plasma column. This

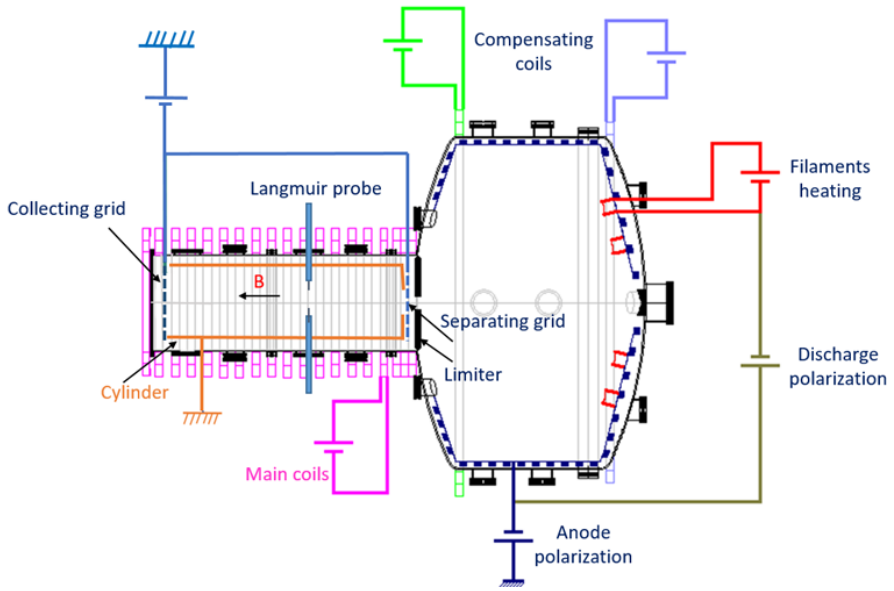

Figure 2.1.: Schematic of MISTRAL. The boundary conditions can be easily controlled or changed. The cylinder is at the ground. The separating and collecting grids are connected and polarized at a negative potential.

results in the formation of a “cusp" (see Fig. 2.2) in front of the filaments. In this way, the trajectory of the electrons emitted from the filaments is deviated and they do not enter directly into the linear cylindrical column.

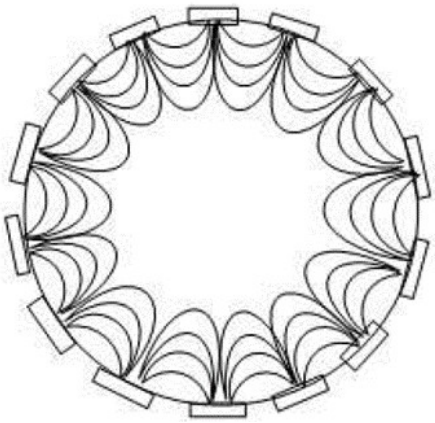

Figure 2.2.: Magnetic field lines forming a cusp in a cross-section of the source chamber. Source[Reb10]

2.1.0.2. Limiter

The linear plasma column and the source are divided by a grounded metallic diaphragm called limiter. The size of the diaphragm sets the diameter of the plasma. In the case of MISTRAL, the limiter opening has a diameter of 8 cm. The area beyond this diameter in the study chamber is referred to as the shadow of the limiter. The limiter

induces a strong radial gradient in the plasma density which is one of the factors leading to the formation of instabilities in MISTRAL plasma.

2.1.0.3. Cylindrical vessel and linear plasma column

Primary electrons ionize the gas particles by collisions resulting in the formation of a plasma in the linear cylindrical column. An outer cylindrical vessel with a diameter of 40 cm surrounds the cylindrical chamber in which plasma is generated. The generated plasma can be seen from the glass window at the end of the linear column. The cylindrical chamber has a length of 1.2 m and is 20 cm in diameter. The main coils, as shown in Fig. 2.1, surround the cylindrical vessel and generate an axial magnetic field within the range of 10 - 36 mT. Depending on the requirements of the experiment, the linear cylindrical column can either be polarized, floating, or connected to the ground.

2.1.0.4. Boundary conditions

Two polarizable grids are placed at both ends of the plasma column setting the axial boundary conditions. The separating grid which separates the source chamber and the study chamber (cylindrical column) is usually polarized negatively to prevent low-energy electrons from entering the column. At the end of the plasma column is a second polarizable grid known as the collecting grid. Controlling the axial boundary conditions, which are determined by the biasing of these grids, allows one to alter the state of the plasma. In Fig. 2.1, the grids are connected and polarized at a negative potential which is one of the configurations used for the experiments given in section 2.5. Nonetheless, the grids can also be grounded or left floating, biased separately or together, depending on the requirements of the experiment.

The values of fixed or manually regulated experimental parameters on Mistral are summarized in the table 2.1.

In MISTRAL, the plasma self-organizes to generate a radial electric field. This electric field, combined with the axial magnetic field results in a cross-field configuration ($\mathbf{E}\perp\mathbf{B}$), also, commonly found in tokamaks, Hall effect thrusters, and ion sources. MISTRAL stands out as a human-scale device that can be operated by a single person. It is designed with multiple optical apertures and access points for intrusive diagnostics. Notably, MISTRAL offers the advantage of steady-state operation for extended durations.

2.2. Available tools and diagnostics

A number of diagnostics are available on MISTRAL including Langmuir probes, Laser-Induced Fluorescence (LIF), Sonification of the plasma, Intensified camera, and tomography. These diagnostics are documented in [Dav17], [Jae10], and [Reb10]. In

Parameter	Unit	Value
Cylinder Length (L)	m	1.2
Core plasma radius	cm	4
Cylinder radius (R)	cm	10
Magnetic field (B)	mT	10-36
Pressure (P)	mbar	$10^{-3} - 10^{-5}$
Filament current	A	120-140
Discharge voltage	V	50
Anode voltage	V	20
Separating grid polarisation	V	-40 - 40/ floating
Collecting grid polarisation	V	-40 - 40/ floating
Cylinder polarisation	V	-40 - 40/ floating

Table 2.1.: Mistral experimental parameters

the scope of this thesis, only the Langmuir probe has been used as a diagnostic to characterize the linear plasma column. A brief overview of how these diagnostics are helpful in characterizing the MISTRAL plasma is given in the following section.

2.2.1. Langmuir probes

Langmuir probes also called electrostatic probes, are one of the most common diagnostics available to characterize the plasma. It works on the simple principle of introducing an electrode in the plasma, biased at the potential V_B with respect to the ground as shown in Fig. 2.3(a). On varying the potential V_B, the current I is recorded and one can obtain the $I(V_B)$ characteristics as shown in Fig. 2.4. From the resulting $I(V_B)$ characteristics, a number of plasma parameters like plasma potential (V_p), floating potential (V_f), electron density (n_e), and electron temperature (T_e) can be determined.

The ion Saturation Current, or I^i_{sat}, is located at the most negative biasing, where all of the electrons have been repelled. The potential at which the electron and ion currents are equal such that the net current is zero is called floating potential V_f. In the transition region between V_f and V_p, the electrons are repelled by the potential $V_B - V_p$. All the flux of the electrons is gathered as V_B reaches V_p. In the electron saturation region, the electron current I_e increases slowly because of sheath expansion [LL05].

The obtained $I(V_B)$ characteristic can be divided into three parts: the ion saturation region, the transition region, and the electron saturation region (see Fig. 2.3 (b)).

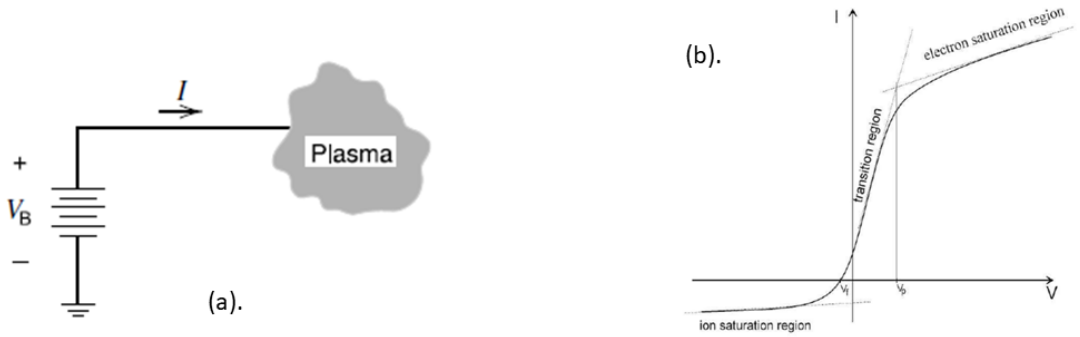

Figure 2.3.: (a). The electrical circuit of a Langmuir probe [LL05] and (b). Ideal characteristics obtained by using a Langmuir probe

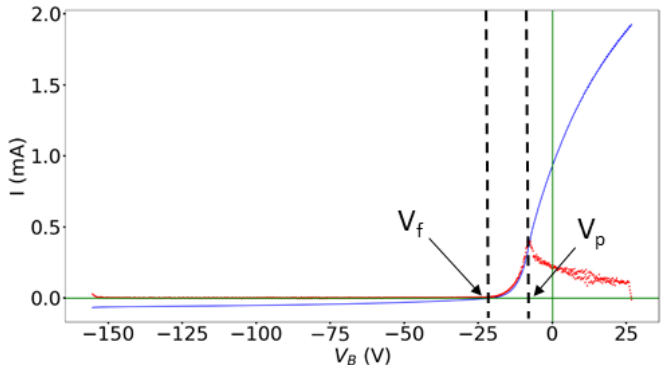

Figure 2.4.: $I(V_B)$ characteristics of a Langmuir probe for an experimental case of MISTRAL. The red curve denotes the first derivative of I w.r.t. V_B.

2.2.1.1. Ion saturation region

When the probe potential is negative enough to repel all the electrons, only ionic current is collected. The ionic current collected is, $I^i_{sat} = -en_s v_s A_s$ where n_s is the ion density and v_s is the velocity at the sheath edge, A_s is the surface of the sheath limit. It enables a satisfactory assessment of the ionic density under ideal experimental conditions.

However, the density at the sheath edge is not exactly equivalent to the bulk plasma density because of the presence of the pre-sheath region (Fig. 2.5). In this case, the ionic velocity must meet the Bohm sheath criterion due to the physics of the sheath in front of the probe [LL05]. The current collected at the bias far below the floating potential ($V_B << V_f$) is then the ion saturation current,

$$|I^i_{sat}| = e\alpha n_i u_B A_s \tag{2.1}$$

where α is n_s/n_i; it represents the density at the sheath edge (n_s) relative to the density of the bulk plasma (n_i) and $u_B = \sqrt{T_e/m_i}$ is the Bohm speed. This implies that the

ion saturation current serves as a measure of the plasma density when the electron temperature and, hence, u_B, are known.

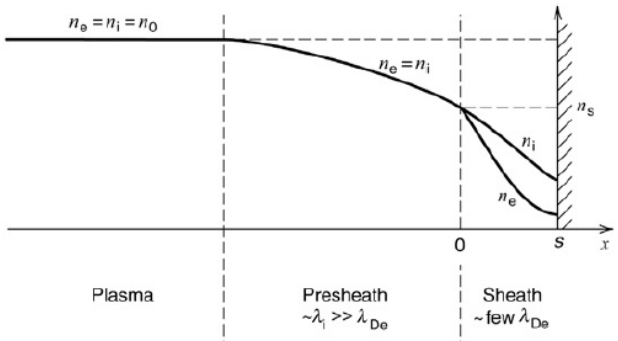

Figure 2.5.: Qualitative behavior of sheath and pre-sheath in contact with a wall. Source [LL05]

2.2.1.2. Floating potential (V_f)

By increasing the probe potential from the ionic saturation region, fewer and fewer electrons are repelled by the probe from the plasma. When the (small) portion of electrons captured is just sufficient to cancel the ionic current such that $I_e + I_i = 0$, then the probing potential corresponding to this current is known as the floating potential V_f. It refers to the potential at which an isolated object places itself in order to maintain the equality of the collected ionic and electronic currents.

2.2.1.3. Plasma potential (V_p)

There are two distinct ways by which plasma potential can be measured [Che03]. In the transition and electron saturation areas, draw straight lines through the $I(V_B)$ curve, designating the crossing point as V_p (see Fig. 2.3(b)) However, it does not work well if the electron saturation region is curved as shown in Fig. 2.4. Then, one can take another approach. The measure of the maximum of $I'(V_B)$ (Here ' refers to the derivative w.r.t. to V_B) corresponds to the plasma potential V_p [Che03] as shown in Fig. 2.4, where $I'(V_B)$ has a clear maximum.

2.2.1.4. Transition and electron saturation region

Between V_f and V_p, only the electrons of sufficient energy are able to cross the potential drop between the plasma and the probe to reach the collecting surface, which results in an electronic current varying exponentially with the probe potential given by [Che03]:

$$I_e = I_{sat}^e exp\left(\frac{e(V_B - V_p)}{T_e}\right) \tag{2.2}$$

where

$$I_{sat}^{e} = \frac{eAn_e\bar{v}}{4} = eAn_e\sqrt{\frac{T_e}{2\pi m_e}} \tag{2.3}$$

is the electron saturation current at V_p and A is the collecting surface area of the probe tip. The electron current increases exponentially when V_B approaches V_p. This exponential development is related to the electron temperature through the Maxwellian distribution of electron velocities. Therefore, T_e can be evaluated from the slope of $ln(I_e) - V_B$ curve which can be obtained using Eq. 2.2. I_e to be used in the Eq. 2.2 can be calculated by subtracting ionic current from the total current.

As the plasma is created by the injection of primary electrons in the linear column of MISTRAL, the presence of these primary electrons can interfere with the Langmuir probe characteristics originally measured for the secondary electrons [Jae10]. In concrete terms, the primary electrons manifest themselves in the form of an additional characteristic. One of the factors leading to the slope appearing in the ion saturation region of the $I(V_B)$ characteristics shown in Fig. 2.4 is the effect of primary electrons. The other factor is the gradual transition in the ion distribution within the presheath [Che03]. Therefore, to accurately determine plasma density using the ion saturation current, one can measure the ion density by polarizing the probe at a potential less than the energy of the primary electrons. Another way is to estimate the electron density using the electron saturation current as given by Eq. 2.3.

Although the basic working principle of the Langmuir probe is rather straightforward, the theory that governs how probes function can be very intricate. A detailed explanation of these theories is available in [Che03]. In fact, the presence of the probe in the plasma disturbs it, modifying the parameters to be measured. In addition, sheath phenomena appear naturally in the vicinity of the probes which modify their effective surface, especially when a significant current is collected or when a magnetic field is present [Hut02].

In the context of this work, a motorized Impedans Langmuir probe is used to measure the plasma characteristics, and the details of the measurements are given in Section 2.5.

2.2.2. Sonification of the plasma

The measured Langmuir probe signals can be seen on the oscilloscope's display. However, walking around the room to manage other diagnostics when doing an experiment is often necessary. Rotating modes can be investigated on Mistral, as will be discussed in section 2.3. Sonification enables the aforementioned probe signal rotating at a frequency of a few kHz to be transmitted from speakers [Esc12]. The frequency or sound variations make it simple to spot any shifts from a normal frequency mode to erratic or irregular behavior. The plasma can then be freely observed while concentrating

on other things from anywhere in the room. Using this diagnostic to keep track of the stationary rotating modes during the measurements specified in the section 2.5 proved to be incredibly helpful.

2.2.3. Fast camera diagnostic

MISTRAL has an axial monochrome camera located at the end of the column that can capture up to 900,000 img/s. This fast camera allows us to observe the flute modes. Pictures from the column's end and the side aperture can be obtained, either directly or through averaging over numerous synchronized acquisitions, as shown in [Ann+11]. The use of the camera is based on the fact that the ionization rate in MISTRAL being very low, the emitted light is mainly due to the de-excitation of the neutrals. In addition, the number of energized neutrals in a radiative state, i.e. being able to de-excite by emission of a photon, is proportional to electron density, n_e. The brightness of a pixel of the camera is thus proportional to n_e (ignoring the fluctuations in electron temperature T_e)[A E10].

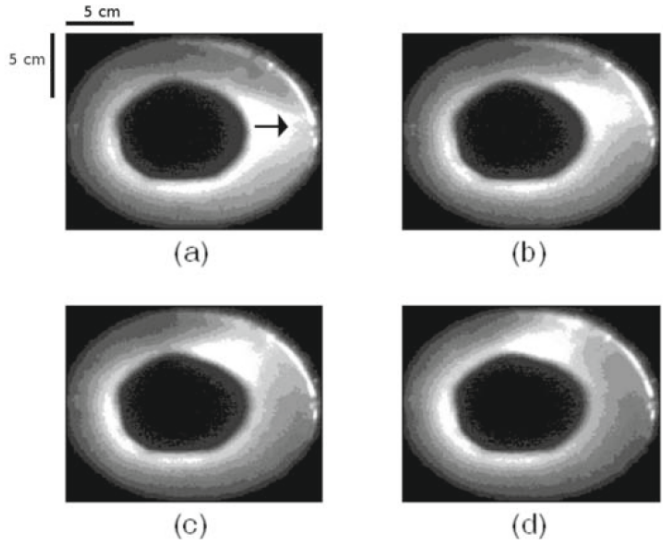

Figure 2.6.: Axial view of the spoke rotating around the central plasma column which has been masked with a 10 cm disk. Source[A E10]

The sensor dynamics preclude simultaneous imaging of the core and edge plasma when imaging the plasma from the end of the column (to have an average radial distribution of the emissivity). The edge appears black when the core plasma is measured. On the other hand, in order to observe the edge, the core plasma must be covered. The camera can be used in particular to determine the direction of rotation of the instability and the mode parity m. An example of how the image taken with the help of fast camera diagnostics after processing appears is shown in Fig. 2.6. The mode is rotating in the anticlockwise direction with the mode parity $m = 1$.

2.2.4. Laser Induced Fluorescence

Laser Induced Fluorescence (LIF) is a local and non-intrusive diagnostic that was installed and used extensively during the Ph.D. of C. Rebont [Reb10]. This technique allows the measurement of many plasma properties with a high degree of spatial and temporal resolution. It is a plasma diagnostic technique in which a laser is tuned to a transition from a sufficiently populated level of an atom, ion, or molecule, usually a ground or metastable level. The subsequent fluorescence, when the atom, ion, or molecule undergoes a transition to a lower level which may be directly or indirectly connected to the excited level is observed (see Fig. 2.7). LIF can be used to identify the presence of species, their densities, and their velocity distribution functions [EKG20].

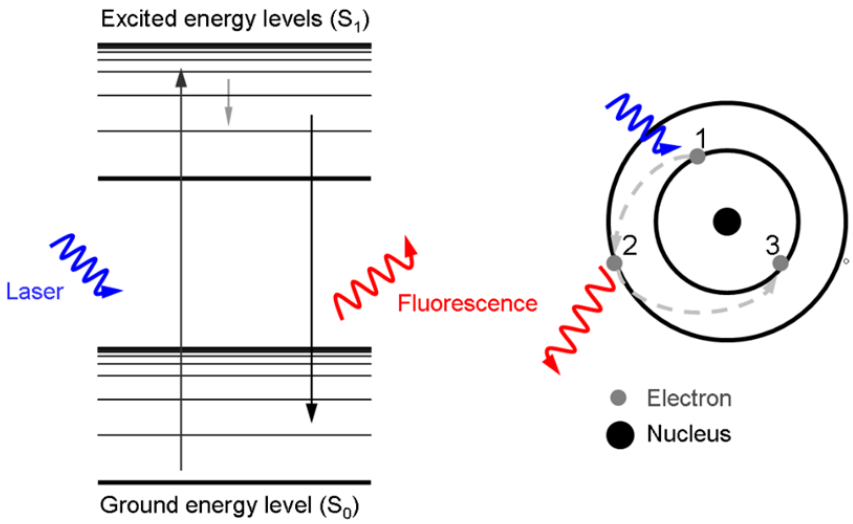

Figure 2.7.: Schematic of LIF. A laser excites a low-lying metastable state in the discharge gas. The atom in the intermediate excited state then de-excites, releasing a photon, which gives the laser-induced fluorescence (LIF) signal.

The velocity map of a plasma section, determined for azimuthal mode number $m = 2$ by LIF (see figure 2.8), shows a complex structure [Reb+11], [Cla+18] with ions moving radially between the arms and azimuthally at the position of the plasma arms. The dotted axis in the middle locates the presence of the maximum density of the spiral arms. The angle formed between the electric field and the velocity is approximately $\pi/2$. A more detailed explanation can be found in [Reb+11].

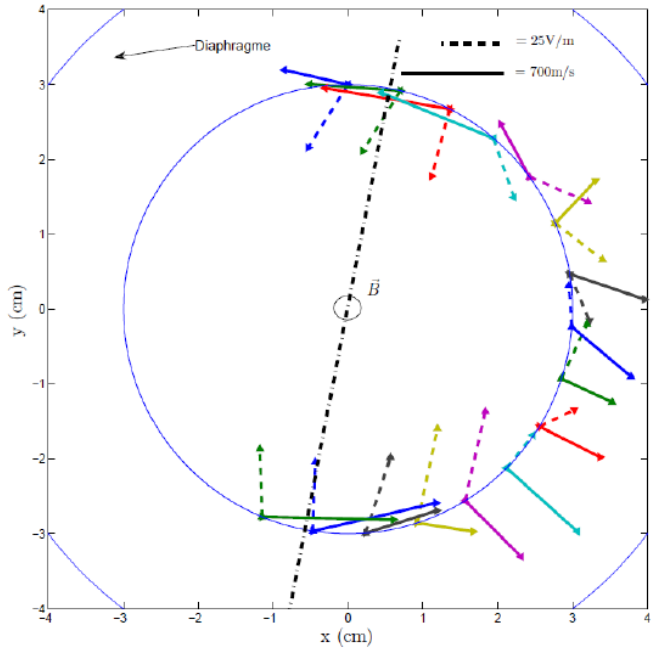

Figure 2.8.: Spatial reconstruction of velocities and electric field. The solid line vectors represent the velocities and the electric field is represented by the dashed arrows. Source[Reb10]

2.2.5. Tomography

Tomography also comes in the category of non-intrusive diagnostics that was installed and used to investigate the occurrence of global rotating modes in the linear plasma column of MISTRAL during the Ph.D. of P. David [Dav17]. Tomography is based on the principle of solving an inverse problem. The line-integrated plasma emissivity is measured along different viewing directions or lines of sight using a photodiode. The local plasma emissivity can then be determined by applying a numerical algorithm for the tomographic inversion of the line-integrated measurements [Dav+17].

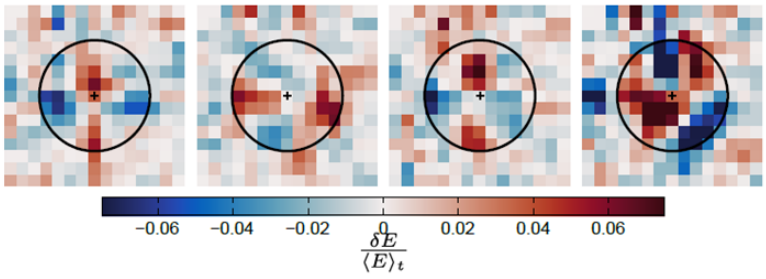

Figure 2.9.: Evolution of the emissivity variation δE for a $m = 2$ rotating mode. Each image is separated by 45 μs and the period of the mode of about 195 μs. Values are normalized to the average emissivity at the center. Source[Dav17]

A result from [Dav17] is shown in Fig. 2.9 where the tomographic inversion of plasma

emissivity (δE) normalized to average emissivity ($< E >_t$) is presented for mode $m = 2$. The measured emissivity is proportional to the primary and thermal electron densities as given in [Dav+17].

2.2.6. Spectro-tomography

The spectro-tomography technique is the combination of the well-known spectroscopy technique and the widely used tomography analysis method. Spectro-tomography combines the advantage of these two approaches to simultaneously offer spatial and spectral resolution. The coupling of spectroscopy and tomography techniques gives access to the local plasma light emission at different wavelengths (visible and near IR) in the plasma. This method provides 2D maps of light intensities at different wavelengths, giving access to the plasma electronic density and temperature. The tomography setup installed on MISTRAL [Pie16] was updated to perform visible spectro-tomography [Gon+20]. 2D maps of the electronic density and plasma temperature were measured and found to be in good agreement with the Langmuir probe results.

2.3. Coherent rotating modes in MISTRAL

Coherent rotating modes have drawn attention for more than half a century, although their exact nature is still unknown. Coherent rotating modes are self-organizing structures that exhibit long-wavelength and plasma oscillations having frequency of the order of 10–100 kHz [KHK18]. These are often observed in a cross-field configuration, where the electric field and magnetic field are perpendicular to each other ($\mathbf{E} \perp \mathbf{B}$). These rotating structures propagate either along (+) or opposite (-) of the $\mathbf{E} \times \mathbf{B}$ drift direction depending on the plasma properties and the geometry of the electromagnetic fields [IC08].

In the past few decades, coherent rotating structures have been frequently observed in various linear devices [Man+11], [Tan+12], [Gra+04], [Pow+18], [Cor+15]. In each instance, the observable structures have been interpreted differently. For example, some coherent low-frequency rotation modes are explained as flute modes [Bro+06], as blobs in [Man+11], or as a spoke [Pow+18]. A brief comparison of the instabilities leading to the formation of these rotating modes and the associated theories with the respective parameters and hypotheses is provided in Chapter 4.

Coherent rotating spokes have been observed in MISTRAL plasma with the experimental evidence given in [SPR09], [Mat+03], and [Pie+04]. The current collected by two probes placed at the same distance from the wall and facing each other (see Fig. 2.10 (b)) can determine the frequency and parity of the spokes. Both probes detect a current oscillation at the same frequency when there is a rotating mode, and the parity of the mode is determined by the phase difference between the two signals. If

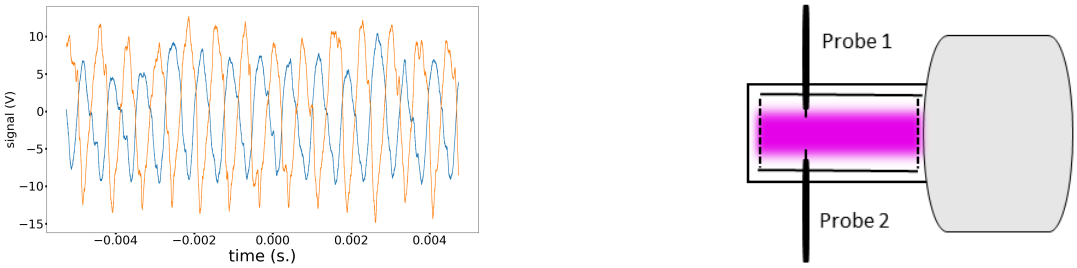

Figure 2.10.: (a). Mode $m = 1$ in MISTRAL (b). Schematic to check mode parity in MISTRAL using Langmuir probes

the signals are in phase, the mode is said to have even parity; if they are out of phase, the mode is said to have odd parity. The fast camera analysis that has been done in the previous works [A E10], [Vid21] also supports the existence of $m = 1, 2$ and 3 modes in Mistral (see Fig. 2.6, 2.13), where m is the azimuthal mode number. Fig. 2.10(a) shows the signals measured on the oscilloscope when the probes are placed as shown in Fig. 2.10(b) in the plasma column at the same distance from the center and it corresponds to $m = 1$ mode.

2.4. Different configurations explored in MISTRAL with rotating spoke

By controlling the axial boundary conditions, the biasing of the cylinder, pressure, and magnetic field, MISTRAL can be used in a variety of configurations. A coherent rotating mode is not necessarily obtained with a random set of experimental parameters. Therefore, to achieve a state with a regular frequency spoke, it is necessary to adjust various experimental parameters. This section lists a few different configurations using two different gases Ar and Xe so that readers can get a general idea of how the plasma state changes in MISTRAL based on the configuration utilized [Vid21].

Schematic	Reference cases
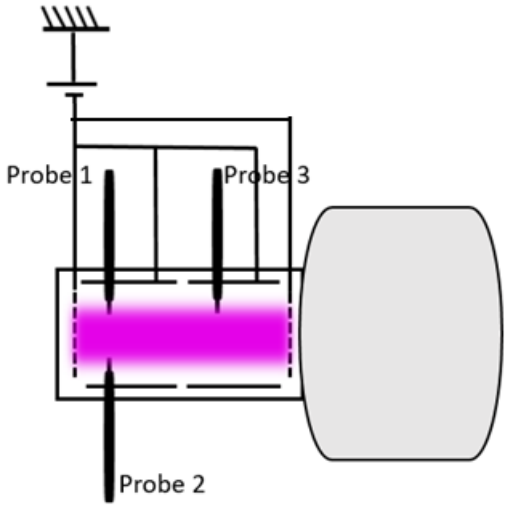	In this case, the separating grid, the collecting grid, and the cylinders are connected and then polarized at -34 V as shown in the corresponding image. The other fixed parameters are listed below, 1. Configuration I: • Gas used: Argon • B=160 G, P=1.1 × 10^{-4} mbar. • V_{anode}= 20 V, I_{anode}= 5.1 A • V_{dis}= 50 V, I_{dis}= 6.7 A • V_{fil}= 16.8 V, I_{fil}= 130 A In this case, the separating grid, the collecting grid, and the cylinders are connected and then polarized at -10 V. The other fixed parameters are listed below, 1. Configuration II: • Gas used: Xenon • B=160 G, P=5 × 10^{-5} mbar. • V_{anode}= 20 V, I_{anode}= 3.8 A • V_{dis}= 50 V, I_{dis}= 6.9 A • V_{fil}= 16 V, I_{fil}= 120 A
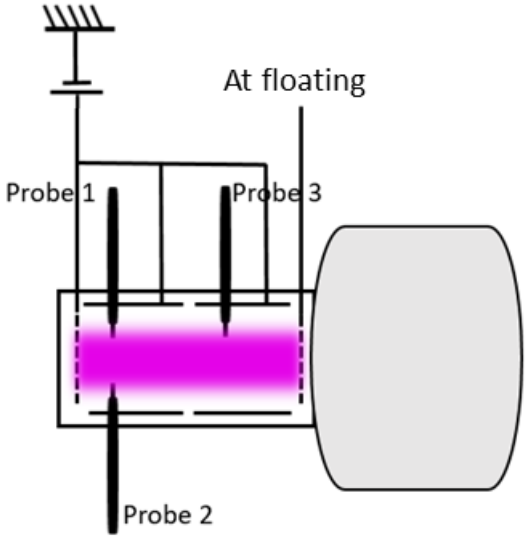	For this case, the separating grid is kept floating and the collecting grid is connected to the cylinders and then polarized at 16.8 V as shown in the corresponding image. The other fixed parameters are listed below, 1. Configuration III:: • Gas used: Argon • B=160 G, P=1.22 × 10^{-3} mbar. • V_{anode}= 20 V, I_{anode}= 10.8 A • V_{dis}= 50 V, I_{dis}= 7.64 A • V_{fil}= 16.6 V, I_{fil}= 110 A

Table 2.2.: Schematic for the experimental configuration with the required parameters. Probe 1 and Probe 2 detect the mode parity and frequency. Probe 3 is a motorized probe to perform measurements at various radial positions. V_{anode} and I_{anode} corresponds to the anode voltage and current respectively. V_{dis} and I_{dis} refers to the discharge voltage and current respectively. V_{fil} and I_{fil} is the filament voltage and current respectively. All these components have already been explained in Section 2.1.

Figs. 2.11 (a), 2.12 (a) and 2.13 (a) present the processed camera images taken for Configurations I, II and III respectively. The mode parity was observed to be $m = 1$ with a spoke frequency of 3.3 kHz for Configuration I, $m = 2$ with a spoke frequency of 0.79 kHz for Configuration II and $m = 3$ with a spoke frequency of 0.55 kHz for Configuration III. The central bright plasma was covered with a disk in order to observe the plasma arms in the shadow of the limiter. This work was performed with Théo Vidril as a part of his master's thesis and the experimental protocol for performing the measurements can be found in [Vid21]. The corresponding normalized fluctuations for electron density are also displayed in the polar coordinates (Fig. 2.11 (b)) by using the data measured by employing the Langmuir probe which makes the fluctuations more visible. For more details refer to [Vid21].

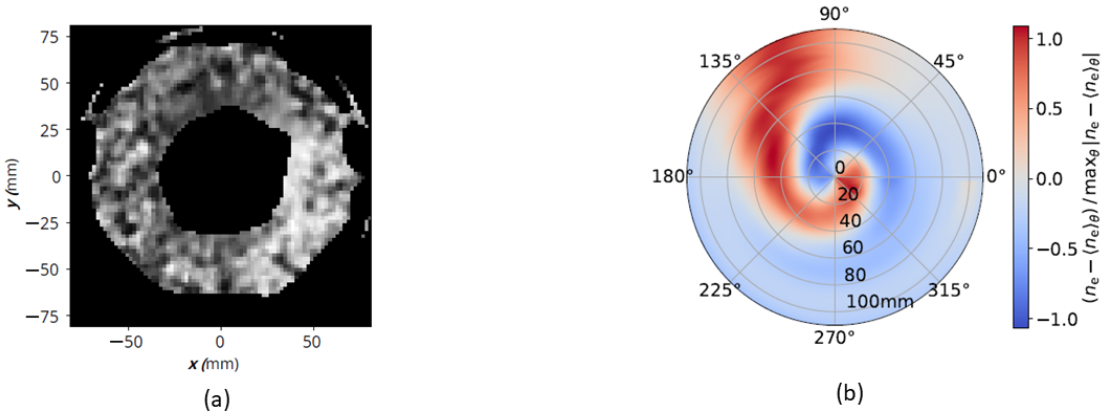

Figure 2.11.: (a). Fast camera image acquisition synchronized to the rotating spoke with a dedicated polarised probe and (b). normalized fluctuations of electron density for Configuration I. Here $< . >_\theta$ denotes the azimuthal mean and max_θ denotes the maximum corresponding to the variable θ.

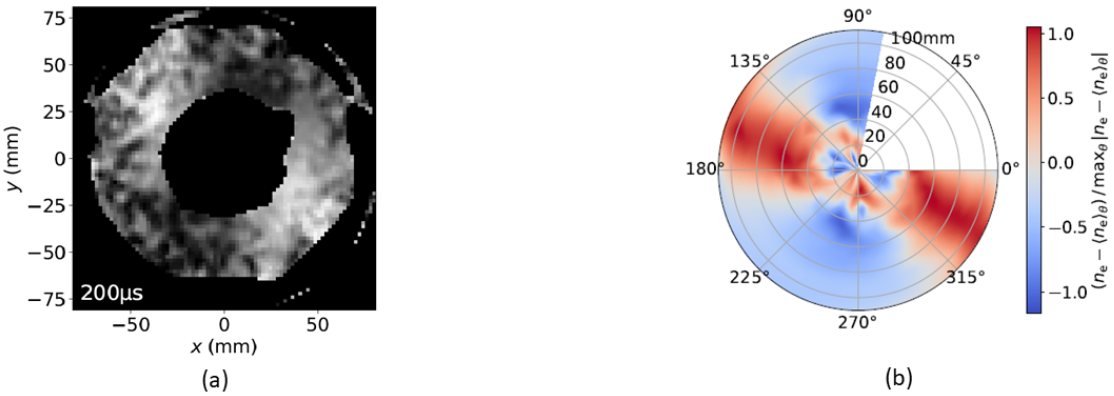

Figure 2.12.: (a). Fast camera image acquisition synchronized to the rotating spoke with a dedicated polarised probe and (b). normalized fluctuations of electron density for Configuration II.

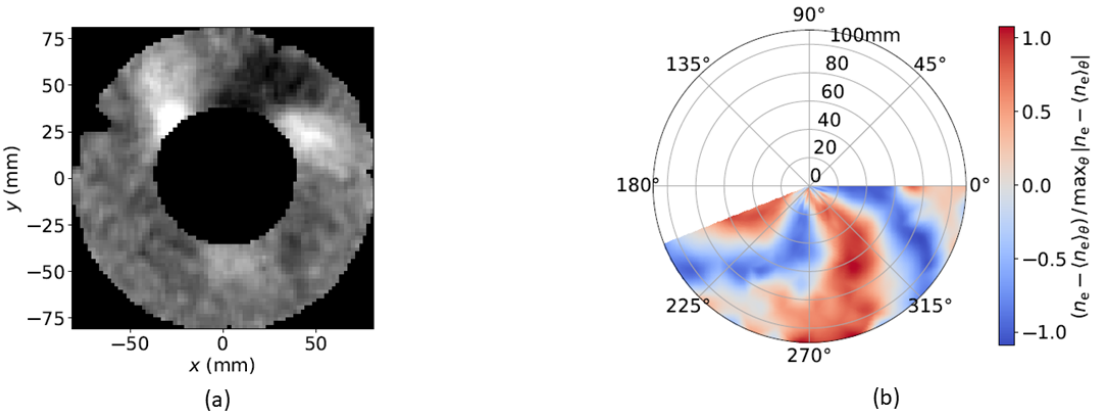

Figure 2.13.: (a). Fast camera image acquisition synchronized to the rotating spoke with a dedicated polarised probe and (b). normalized fluctuations of electron density for Configuration III.

The modes $m = 1,3$ appear to have a spiral shape whereas this is not the case for mode $m = 2$ obtained for the Configuration II.

In addition to the experimental investigation, theoretical modeling is required to investigate the physics behind the existence of coherent rotational modes in MISTRAL. Knowing the range of different plasma parameters can be useful in figuring out what assumptions are necessary to develop and validate the theoretical model. The next section details the measurement of these variables required for the theoretical modeling discussed in Chapter 4 and Chapter 5. The time-averaged radial profiles of electron density and electron temperature at various pressure values and magnetic field strengths provide a range of the necessary values.

2.5. Reference experimental conditions

In the present investigation, a specific configuration is employed for a particular reference case. Unless otherwise stated, Ar gas is used for generating the plasma.

The description of the employed configurations along with the variable and fixed parameters used to determine the range of plasma characteristics is given in table 2.3,

Schematic	Reference cases
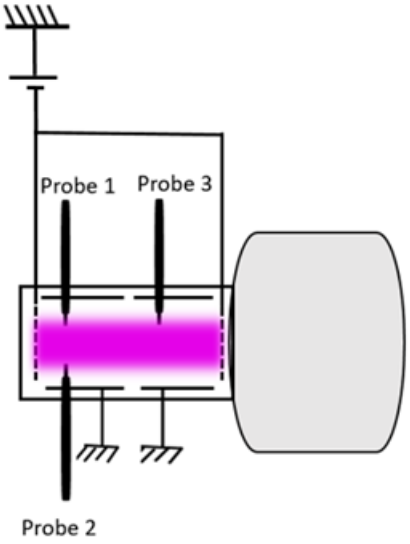	For this case, the separating and collecting grids are connected and polarized at -30 V, and both the half cylinders were kept at the ground as shown in the corresponding image. The other parameters were fixed as given below: • V_{anode}= 20 V, I_{anode}= 3.9 A • V_{dis}= 50 V, I_{dis}= 4.54 A • V_{fil}= 16.4 V, I_{fil}= 122.2 A Two reference cases are discussed based on this configuration: 1. Reference case A: • B→varied, P≈ 10^{-4} mbar. 2. Reference case B: • B=160 G, P→varied.

Table 2.3.: Schematic for the experimental configuration with the required parameters relevant to the measurements given in section 2.5.

2.6. Time averaged profiles

Time-averaged radial profiles of electron density n_e and plasma potential V_p corresponding to the experimental configurations shown in table 2.3 are depicted in this section. The time-averaged plasma characteristics are measured using a motorized Impedans Langmuir probe system. To determine the exact center position of the plasma column, the calibration was performed with the help of a laser. An error of ±3 mm can still be accounted for the probe placement over the range of 10 cm.

2.6.1. Radial profiles for reference case A: magnetic field scan

To observe the impact of the change in the magnetic field on plasma parameters, radial variation in electron density and plasma potential at different magnetic field intensities was observed. This factor could potentially affect the measured plasma characteristics. Fig. 2.14 and Fig. 2.15 shows the radial variation of electron density n_e and plasma potential V_p at various magnetic field intensities.

The electron density and plasma potential both were found to decrease with the

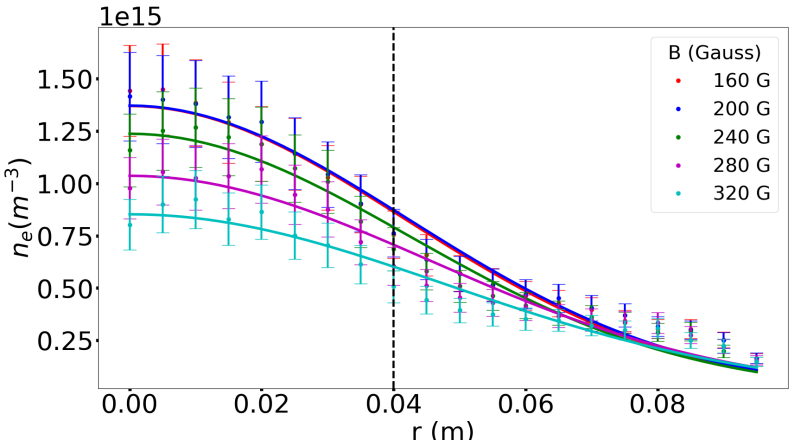

Figure 2.14.: Radial variation of electron density n_e for increasing magnetic field. The dashed black line represents the location of the limiter. The dots represent the experimental measurements and the solid lines represent the theoretical fits.

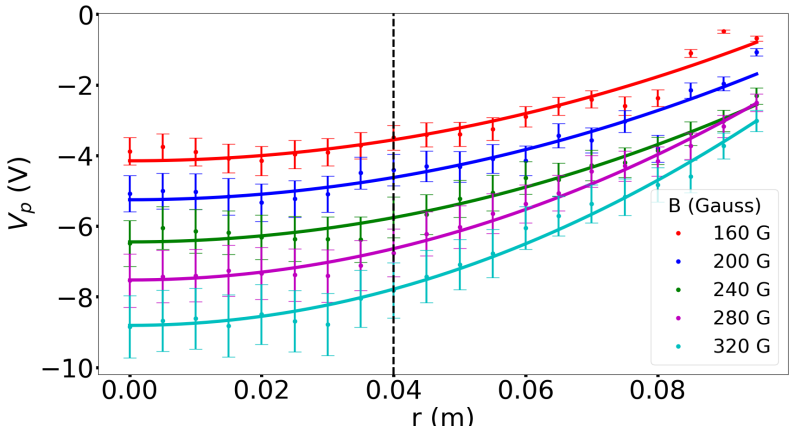

Figure 2.15.: Radial variation of plasma potential V_p for increasing magnetic field. The dashed black line represents the location of the limiter. The dots represent the experimental measurements and the solid lines represent the theoretical fits.

increase in the magnetic field intensity. However, one would expect an increase in electron density near the axis of the plasma column with the increase in magnetic field strength. It will be shown in Section 2.8.2 that with the increase in magnetic field intensity, the plasma oscillations became relatively unstable which may lead to an outward radial transport. It is important to note that while conducting these measurements, only the current in the coils surrounding the linear cylindrical column was changed. The current in the compensating coils that govern the trajectory of primary electrons in the source chamber remains unchanged. Additionally, the pressure of the plasma column noticeably changed when the magnetic field was being varied. These factors could potentially contribute to the unexpected behavior of electron density as the magnetic field strength of the plasma column increases. However, a complete expla-

nation is currently unavailable and further investigation is required to understand this.

As the plasma potential is increasing radially, the electric field is centripetal or is acting radially inwards. Due to this centripetal electric field, ions will experience a force directed towards the center of the column. This confinement force acts to keep the ions within the central region of the plasma column. Electrons being negatively charged, will experience a force away from the center of the column due to the inward electric field. This force will tend to push the electrons towards the outer region of the plasma column.

2.6.2. Radial profiles for reference case B: pressure scan

Electron density and plasma potential profiles were measured at various pressure values. The magnetic field was fixed at B = 160 G. Fig. 2.16 and Fig. 2.17 illustrate the radial variation of electron density n_e and plasma potential V_p at different pressure values.

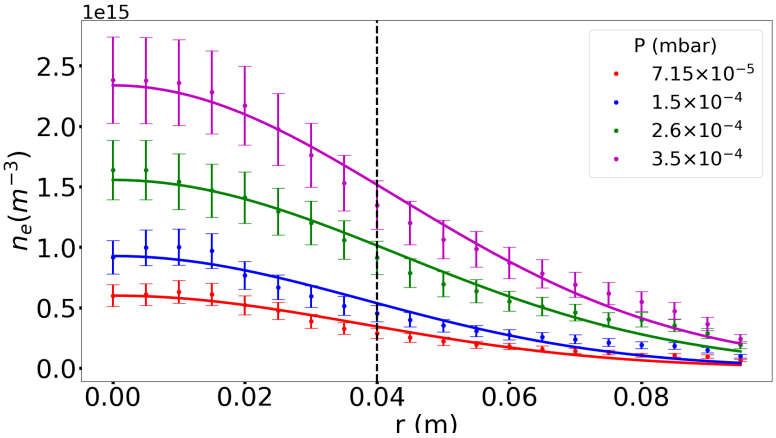

Figure 2.16.: Radial variation of electron density n_e for increasing pressure. The dashed black line represents the location of the limiter. The dots represent the experimental measurements and the solid lines represent the theoretical fits.

Contrary to what was observed with the change in magnetic field, the electron density and plasma potential were found to increase with the increase in pressure. As in the magnetic field scan, the electric field is radially inward. All the potential profiles observed so far are parabolic within the measured uncertainties. However, this is not systematic. At higher pressure, deviations from a parabolic profile are observed (see Fig. 2.18). The plasma potential profiles exhibit non-monotonic behavior closer to the location of the limiter where the electric field is directed outwards.

Corresponding to these configurations, the electron temperature and floating potential profiles are shown in Appendix A. In the following chapters, we will see that only these two parameters (electron density and plasma potential) are necessary to

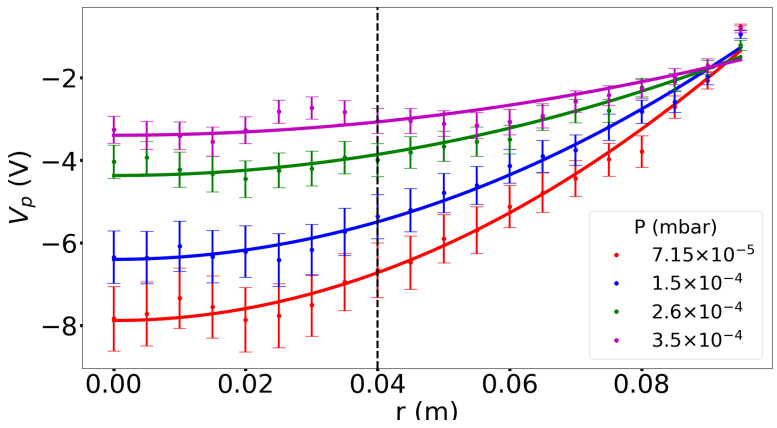

Figure 2.17.: Radial variation of plasma potential V_p for increasing pressure. The dashed black line represents the location of the limiter. The dots represent the experimental measurements and the solid lines represent the theoretical fits.

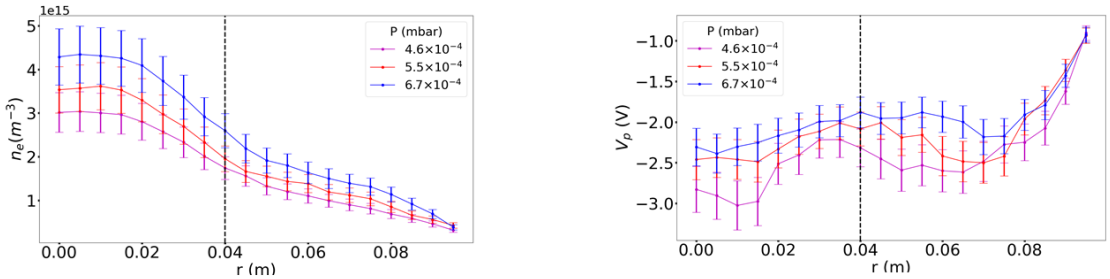

Figure 2.18.: Radial variation of electron density (n_e) (left) and plasma potential V_p (right) for increasing pressure. The dashed black line represents the location of the limiter.

investigate the dynamics of the plasma generated in the linear cylindrical column. One of the factors leading to the observed radial density gradient can be attributed to the presence of a limiter at the input of the plasma column. Furthermore, the controlling factors for the plasma potential are likely related to the biasing of separating and collecting grids which aid in maintaining axial symmetry, and the biasing of linear cylindrical column, which governs the radial boundaries of the plasma. A more comprehensive investigation is required to delve deeper into these factors and their influence on plasma characteristics.

2.6.3. Radial profiles for Configuration I

Fig. 2.19 shows the radial profiles of n_e and V_p corresponding to Configuration I in Table 2.2. The electron density is following a Gaussian distribution with a peak around r=3 cm. The radially increasing plasma potential indicates a centripetal electric field as obtained in ref. cases A and B. One thing to note here is that in this case, the cylinder is polarized at the same voltage as that of the grids. This results in bringing the plasma potential closer to the polarization of the cylinder at the edge of the plasma column.

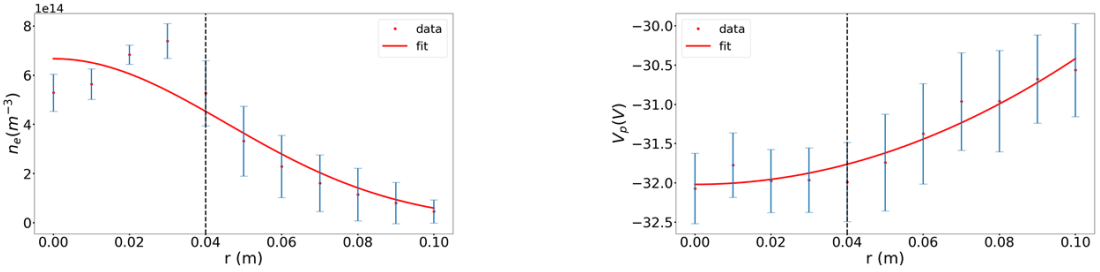

Figure 2.19.: Radial variation of electron density (n_e) (left) and plasma potential V_p (right) for ref. case C. The dots represent the experimental measurements and the solid lines represent the theoretical fits.

In the ref. cases A and B where the cylinder was at the ground, the plasma potential also approaches the same polarization at the edge of the column.

2.6.4. Radial profiles for Configuration III

Time-averaged radial profiles of n_e and V_p for Configuration III are provided in this section [Vid21]. The experimental configuration for this case is given in table 2.2.

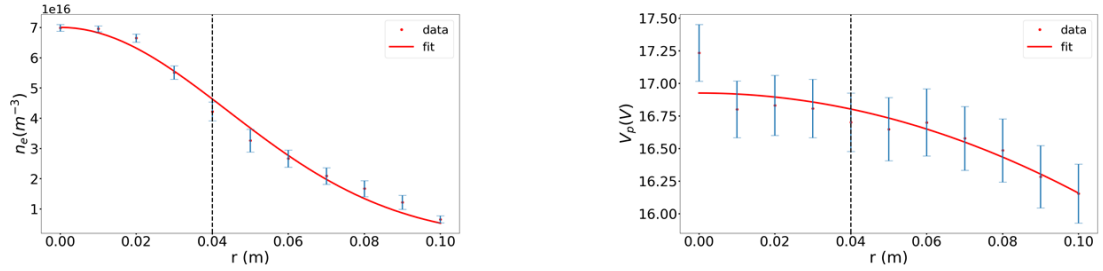

Figure 2.20.: Radial variation of electron density (n_e) (left) and plasma potential V_p (right) for ref. case D.

The electron density is following a Gaussian distribution as before. The electron density obtained in this configuration is greater by a factor of 10 than that obtained in ref. cases A and B due to the positive polarization of the collecting grid. The plasma potential is following a parabolic profile and is decreasing from the center towards the edge of the plasma column. This trend of the variation in plasma potential makes the electric field act radially outwards or centrifugal. This implies that the ions within the central region of the plasma column will experience a force resulting in outward radial transport. Since the electrons are negatively charged, they will be directed towards the center of the plasma column, opposing the outward radial electric field.

2.7. Parameterization of electron density and plasma potential profiles

In the aforementioned cases (showing the variation of plasma characteristics with pressure and magnetic field), the electron density follows a Gaussian distribution and the plasma potential follows a parabolic profile. These curves can be parameterized using the Gaussian distribution for electron density and parabolic distribution for plasma potential given as,

$$n_e(r) = n_{e0}\ exp\left(-\frac{r^2}{r_0^2}\right);\ \ \phi_0 = p_1 r^2 + p_2 \tag{2.4}$$

where n_{e0}, p_1 and p_2 are constants. Here r is the radial coordinate and r_0 is the width of the Gaussian used to parametrize the density profile; r_0 characterizes how fast the plasma density decays to zero when moving radially outward. Such parameterizations provide a convenient mathematical representation, enabling the calculation of various quantities necessary for plasma modeling and analysis.

2.7.1. Magnetic field scans

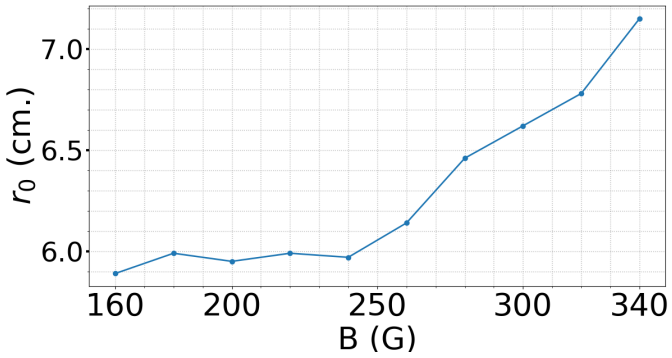

Figure 2.21.: Variation of parameter r_0 for increasing magnetic field strength.

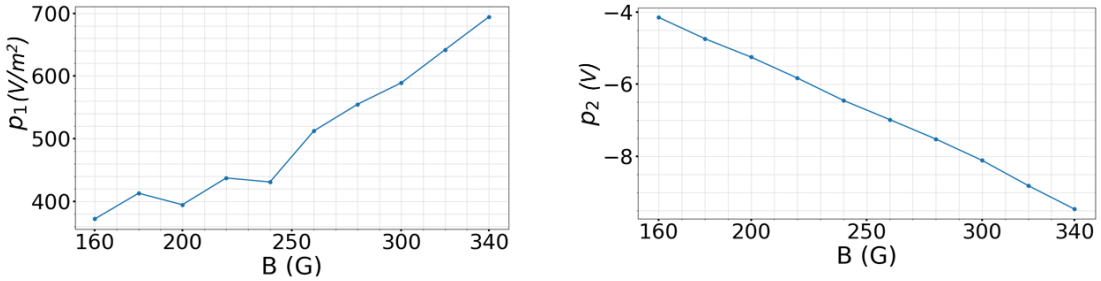

Figure 2.22.: Variation of parameters p_1 (left) and p_2 (right) for increasing magnetic field strength.

The curve fits for the electron density (n_e) and plasma potential (V_p) shown in Section 2.6.1 are performed using Eq. 2.4 for various magnetic field intensities. Fig. 2.21 and 2.22 shows the variation of the parameters r_0, p_1 and p_2 with magnetic field obtained by fitting the experimental data. It can be seen that r_0 varies slowly until B = 240 G and as $B > 240$ G, it starts increasing. The increase in r_0 with the increase in B simply indicates that the Gaussian profile is broadening and the density is decaying to zero more slowly at higher B values in comparison to smaller B values as we move away from the center.

The parameter p_1 is increasing whereas p_2 is decreasing with the increase in magnetic field strength. p_1 represents the steepness of the potential profile and is positive for the inward electric field. The parameter p_2 determines the value of the potential on the axis.

2.7.2. Pressure scans

On a similar basis as done for various magnetic field strengths, the experimental data for n_e and V_p obtained for various pressure values at different radial positions (Figs. (2.16,2.17) is parameterized using Eq. 2.4 and is shown in Figs. 2.23 and 2.24. The plasma potential profiles obtained at $P < 2.6 \times 10^{-4}$ mbar are not completely parabolic which makes it challenging to fit the plasma potential profile with the parabolic fit. However, the parameters calculated from the approximative fit can be used to have an estimate of p_1 and p_2.

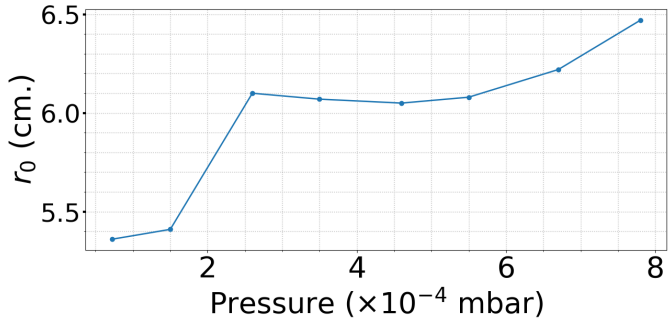

Figure 2.23.: Variation of parameter r_0 for increasing pressure.

The parameter r_0 is increasing abruptly until $P = 2.6 \times 10^{-4}$ mbar. From $P = 2.6 \times 10^{-4}$ mbar onwards, the increase in r_0 gets slower and the increase in r_0 with the increase in pressure follows a parabolic behavior. The parameter p_1 is exponentially decreasing with the increase in pressure whereas the parameter p_2 is exponentially increasing with the increase in pressure.

In conclusion, the variations in r_0 are moderate (20%) and the width of the density profile is mostly determined by the limiter diameter.

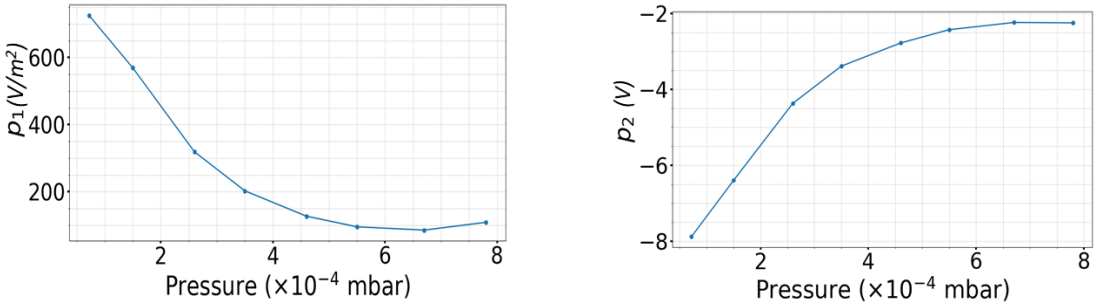

Figure 2.24.: Variation of parameters p_1 (left) and p_2 (right) for increasing pressure.

2.7.3. Parametrization results for Configurations I and III

Even though for Configurations I and III, the scans in pressure and magnetic field were not performed, still the parameters can be computed from the parameterization of the radial profiles for the respective cases shown in Fig. 2.19 and Fig.2.20.

For Configuration I, the parameters are $r_0 = 6.4$ cm, $p_1 = 160.2$, and $p_2 = -32.02$. Regarding Configuration III, the parameters are $r_0 = 6.2$ cm, $p_1 = -76.8$, and $p_2 = 16.9$. The negative value of p_1 and the positive value of p_2 for configuration III is due to the difference in the shape of the plasma potential profile.

2.8. Parametric study of mode frequency

2.8.1. Pressure induced variations on mode frequency

Fig. 2.25 represents the variation of mode frequency with pressure for the ref. case B. The plasma oscillations and frequency are measured at a position of $r \approx 5$ cm from the center of the plasma column using the set-up of two Langmuir probes as shown in Fig. 2.10.

The mode frequency was found to decrease with the increase in pressure. At lower pressure, the mode exhibited a regular frequency, and the amplitude of the oscillation remained relatively stable over time. The mode exhibited clearly a parity of $m = 1$ until P= 5.5×10^{-4} mbar. However, as the pressure increases, the oscillation of the plasma displayed a more erratic pattern, with the amplitude of the oscillation varying significantly over time and no clear indication of mode parity. An example of these two plasma behaviors is given in Fig. 2.26.

Fig. 2.27 displays the Fast Fourier transform (FFT) spectra of the plasma oscillations shown in Fig. 2.26. In Fig. 2.27 (a), the dominant frequency component is present at 4 kHz accompanied by visible harmonics at 8 kHz and 12 kHz. At higher pressure, i.e. in Fig. 2.27 (b), two components are observed at low frequency: one at 2 kHz and another at 3 kHz. The 3 kHz component is smaller but nevertheless sizeable, resulting

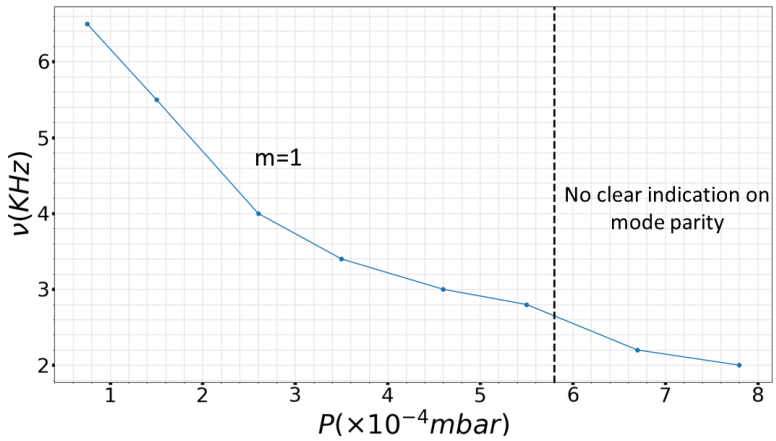

Figure 2.25.: Variation of mode frequency with Pressure

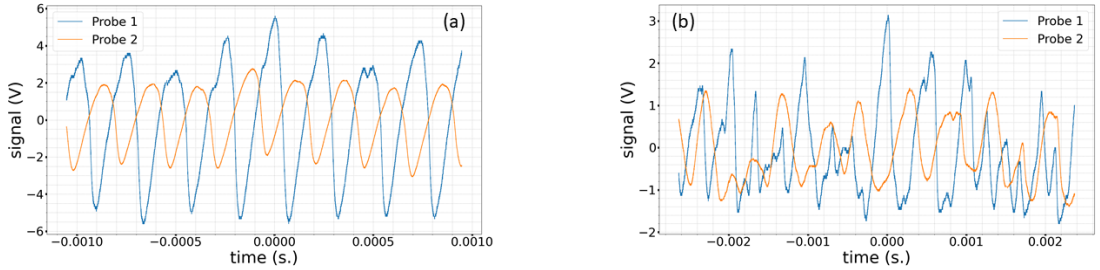

Figure 2.26.: (a). Plasma oscillations for $m = 1$ at $P = 2.6 \times 10^{-4}$ mbar and (b). at $P = 7.8 \times 10^{-4}$ mbar

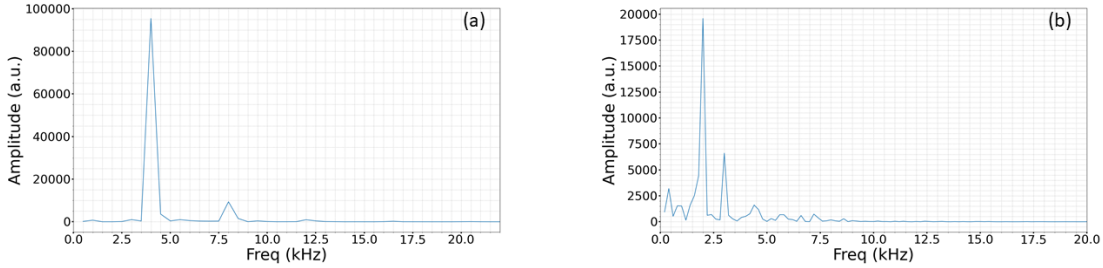

Figure 2.27.: FFT spectrum for plasma oscillations given in Fig. 2.26 at (a). $P = 2.6 \times 10^{-4}$ mbar and (b). at $P = 7.8 \times 10^{-4}$ mbar

in the more chaotic behavior observed in the time trace in Fig. 2.26 (b).

2.8.2. Impact of magnetic field on mode frequency

Fig. 2.28 represents the variation of mode frequency with the increase in the magnetic field for ref. case A. The mode frequency was found to increase linearly with the increase in magnetic field intensity. At low magnetic field values i.e. from B=160 G to 240 G, the plasma oscillations were relatively stable over time. The mode parity $m = 1$ was therefore determined with the use of Langmuir probes placed at the same

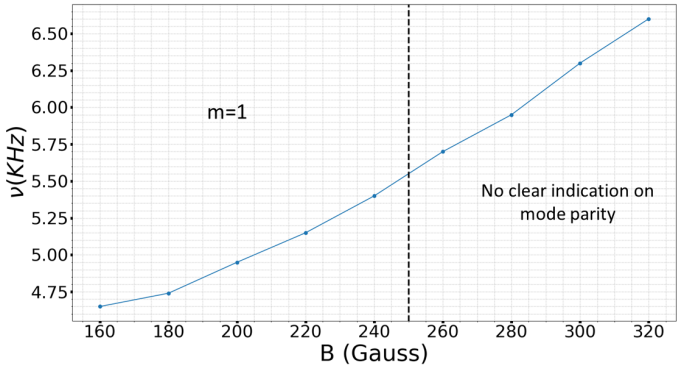

Figure 2.28.: Variation of mode frequency with magnetic field

distance from the center but at the opposite ends as shown in Fig. 2.10 (b). At B>240 G, the plasma oscillations exhibited abrupt temporal variations, rendering the prediction of mode parity using the probes unfeasible. Nevertheless, a dominant frequency persisted at high magnetic field intensities, indicating a consistent trend of the mode frequency with the change in the magnetic field.

2.9. Fluctuation measurements

To study the characteristics of instabilities or turbulent transport, it is necessary to measure the fluctuations of certain plasma quantities, such as those of the density $\tilde{n}$ or of the potential $\tilde{\phi}$. The normalized fluctuations in density and potential can be written as,

$$\frac{\tilde{n}}{n_0} = \frac{n_{emax} - < n_e >}{< n_e >}, \quad \frac{e\tilde{V}_p}{k_B T_{e0}} = \frac{e\left(V_{p_{max}} - < V_p >\right)}{k_B < T_{e0} >} \tag{2.5}$$

The time-averaged electron density $< n_e >$ measured by using a Langmuir probe is subtracted from the maximum electron density of the recorded time series data. It is then normalized using the time-averaged electron density $< n_e >$. The same has been done for potential fluctuations. The only difference being the normalization of the potential fluctuations with the average electron temperature ($< T_{e0} >= 3$ eV). This way, a radial map for electron density and plasma potential fluctuations is obtained.

2.9.1. Configuration I

The radial variation of the fluctuating quantities $\tilde{n}/n_0$ and $e\tilde{V}_p/k_B T_{e0}$ for Configuration I is shown in Fig. 2.29. We will define two quantities here $\left|\frac{e\tilde{V}_p}{k_B T_{e0}}\right|_{max}$ and $\frac{\left|\frac{e\tilde{V}_p}{k_B T_{e0}}\right|}{\left|\frac{\tilde{n}}{n_0}\right|}$

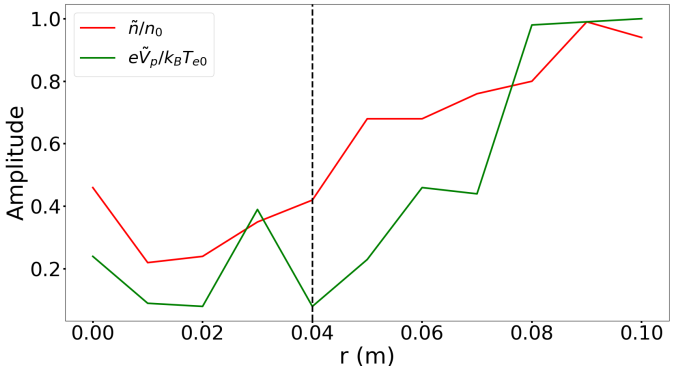

Figure 2.29.: Radial variation of $\tilde{n}/n_0$ and $e\tilde{V}_p/k_BT_{e0}$ for Configuration I. The black dashed line represents the location of the limiter.

which for the present case are given as,

$$\left|\frac{e\tilde{V}_p}{k_BT_{e0}}\right|_{max} \approx 0.9, \quad \frac{\left|\frac{e\tilde{V}_p}{k_BT_{e0}}\right|}{\left|\frac{\tilde{n}}{n_0}\right|} \approx [0.3, 1] \tag{2.6}$$

The normalized quantities determine an important criterion for instability identification as given by [Jas72]. This will be explained later in Chapter 3.

2.9.2. Configuration III

Fig. 2.30 represents the radial variation of fluctuating quantities $\tilde{n}/n_0$ and $e\tilde{V}_p/k_BT_{e0}$ for Configuration III.

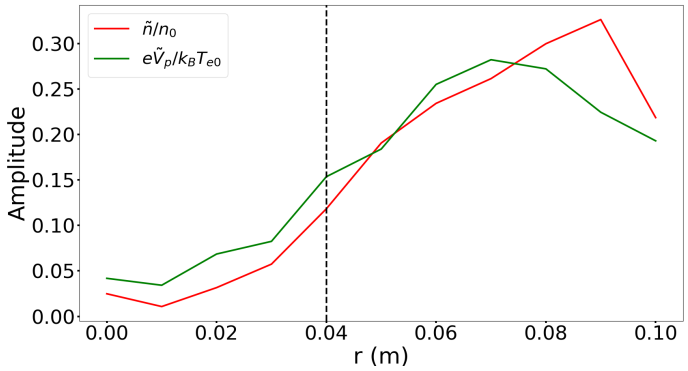

Figure 2.30.: Radial variation of $\tilde{n}/n_0$ and $e\tilde{V}_p/k_BT_{e0}$ for Configuration III. The black dashed line represents the location of the limiter.

The normalized fluctuations in density exhibit a close correlation with the fluctuations in potential. Notably, the magnitude of these fluctuations is significantly smaller at the center of the plasma column compared to the edge.

In this case,

$$\left|\frac{e\tilde{V}_p}{k_B T_{e0}}\right|_{max} \approx 0.28, \quad \frac{\left|\frac{e\tilde{V}_p}{k_B T_{e0}}\right|}{\left|\frac{\tilde{n}}{n_0}\right|} \approx [0.8, 2] \tag{2.7}$$

2.10. Summary

This chapter mainly deals with the experimental work done in the framework of the thesis keeping in mind the theoretical work. It begins by providing a general overview of the linear plasma column experiment MISTRAL, along with a brief description of the available diagnostics. Three different configurations showing the existence of modes $m = 1$, 2 and 3 in the MISTRAL plasma column are presented. Subsequently, the chapter presents time-averaged radial profiles obtained at different magnetic field intensities and pressure values, enabling the characterization of various plasma parameters (n_e, V_p, V_f and T_e). The electron density decreased with the increase in magnetic field whereas it increased with the increase in the pressure. The electric field was found to act radially inwards for the employed configuration. Furthermore, the chapter investigates the influence of pressure and magnetic field on the mode frequency. It is found that the mode frequency decreases with increasing pressure, whereas it increases with the increase in magnetic field intensity. Two additional configurations were further explored for the measurement of density and potential fluctuations. This can be compared to the theoretical predictions in Chapter 5 for instability identification.

3. Modeling of instabilities in magnetized plasma

This chapter provides information on the different types of plasma modeling. A brief discussion of the instabilities that occur in rotating plasma systems is given. Furthermore, it provides an overview of previous theoretical frameworks used to characterize the stability plasmas in cross-field configuration.

3.1. Plasma modeling

The study of plasma behavior and the fundamental processes that govern it relies on a combination of theoretical modeling and experimental research. These complementary approaches are employed to gain a comprehensive understanding of plasmas and their intricate dynamics. Plasma modeling can be used as a tool to identify and characterize the instabilities and understand the formation of coherent rotating structures which is the goal of our thesis.

In contrast to a neutral gas, plasma is made up of various species of charged and neutral particles (neutrals, electrons, and ions) that interact with one another via electromagnetic fields in addition to collisions. The charged particles also react to external electromagnetic fields that are applied to the plasma by electrodes or magnets. Plasma modeling is the process of using mathematical equations and computer simulations to describe the behavior of the plasma. The modeling of plasmas can be challenging because of the complex interactions between charged particles. Several types of plasma models exist, utilizing various physical approximations and formulae. The two primary model types are either based on the kinetic theory or the fluid theory. Magnetohydrodynamics, (MHD), which is a specific fluid model, can also be used to model plasma systems.

3.1.1. Kinetic theory

In the kinetic description of the plasma [Den93], the particles of each species j (where j stands for electrons, ions, and neutrals) are represented by the distribution function $f_j(\mathbf{x},\mathbf{v},t)$ in the phase space $(\mathbf{x},\mathbf{v})$ where the independent variables $\mathbf{x}$, $\mathbf{v}$ and t are position, velocity and time respectively. To describe the evolution of the distribution function $f_j(\mathbf{x},\mathbf{v},t)$, the fundamental equation that is generally used in the kinetic

theory is the Boltzmann equation given by,

$$\frac{\partial f_j}{\partial t} + \mathbf{v}\cdot\nabla_{\mathbf{r}} f_j + \frac{q_j}{m_j}\left(\mathbf{E}+\mathbf{v}_j\times\mathbf{B}\right)\cdot\nabla_{\mathbf{v}} f_j = \left(\frac{\partial f_j}{\partial t}\right)_c \tag{3.1}$$

where $\nabla_{\mathbf{r}} = \hat{x}\partial/\partial x + \hat{y}\partial/\partial y + \hat{z}\partial/\partial z$, $\nabla_{\mathbf{v}} = \hat{x}\partial/\partial v_x + \hat{y}\partial/\partial v_y + \hat{z}\partial/\partial v_z$, q_j is the charge and m_j is the mass of the species j, $\mathbf{E}$ is the electric field and $\mathbf{B}$ is the magnetic field vector. The term $\left(\frac{\partial f}{\partial t}\right)_c$ is the collision term and thus includes the effect of collisions. However, if this term is neglected, the plasma can be considered collisionless and the Eq. 3.1 becomes the collisionless Boltzmann equation [Den93].

If the system is collisional with a collision frequency ν, then the process of thermalization tends to move the system towards a Maxwellian velocity distribution for which the distribution function f is given by,

$$f_j(\mathbf{x},\mathbf{v},t) = n_j\left(\frac{m_j}{2\pi k_B T_j}\right)^{3/2} exp\left(-v^2/v_{thj}^2\right) \tag{3.2}$$

where $v_{thj} = \sqrt{2T_j/m_j}$ is the thermal velocity characterizing the distribution and T_j defines the temperature of the species (in eV) which can be determined from the width of the distribution.

Eq. 3.1 describing the evolution of f_j is coupled with Maxwell's equations for electric and magnetic fields to form a closed system of equations describing our plasma. These are,

$$\nabla\cdot\mathbf{E} = \frac{\rho}{\epsilon_0},\quad \nabla\times\mathbf{E} = -\frac{\partial\mathbf{B}}{\partial t},\quad \nabla\cdot\mathbf{B} = 0,\quad \nabla\times\mathbf{B} = \mu_0\mathbf{J} + \frac{1}{c^2}\frac{\partial\mathbf{E}}{\partial t} \tag{3.3}$$

with ϵ_0 and μ_0 as the permittivity and permeability of the free space respectively. The charge density ρ and the current density $\mathbf{J}$ can be evaluated using the distribution function f_j,

$$\rho = \sum_j q_j\int_{-\infty}^{+\infty} f_j(\mathbf{x},\mathbf{v},t)d^3v,\quad \mathbf{J} = \sum_j q_j\int_{-\infty}^{+\infty}\mathbf{v}f_j(\mathbf{x},\mathbf{v},t)d^3v \tag{3.4}$$

The kinetic description of plasma accounts for the microscopic processes in the plasma and therefore can give a comprehensive description of plasma behavior. However, the high accuracy comes at the cost of high complexity and high computational needs.

3.1.2. Multi-fluid theory

A simplified treatment that describes the evolution of macroscopic plasma quantities is available in terms of fluid equations [Che16]. By averaging over the velocity coordinates of the distribution function f_j, one can derive equations that only depend on

the spatial coordinates and the time. These equations describe the evolution of the averaged quantities, e.g., density n_j and velocity $\mathbf{v}_j$ obtained by taking the velocity moments of the distribution function,

$$n_j(\mathbf{x},t) = \int_{-\infty}^{+\infty} f_j(\mathbf{x},\mathbf{v},t)d^3v \tag{3.5}$$

$$\mathbf{v}_j(\mathbf{x},t) = \frac{1}{n_j}\int_{-\infty}^{+\infty} \mathbf{v} f_j(\mathbf{x},\mathbf{v},t)d^3v \tag{3.6}$$

3.1.2.1. Continuity equation:

The continuity equation which denotes particle conservation can be obtained by integrating Eq. 3.1 over the velocity space for each species j and is given as,

$$\frac{\partial n_j}{\partial t} + \nabla\cdot(n_j\mathbf{v}_j) = S - L \tag{3.7}$$

where $j = i, e$ stands for either ions or electrons, n_j is the number density and v_j is the velocity of the species j. S and L are the source and loss terms that originate from the integration of the collision term in Eq. 3.1 [LL05]. If collisions are neglected, the right-hand side of Eq. 3.7 is zero.

For MISTRAL plasma [Jae10], the RHS of Eq. 3.7 represents the rate per unit volume at which particles of a considered species are produced or lost as a result of collisions and can be written as,

$$S_{ion} = n_{ep}\nu_{ion} \tag{3.8}$$

where n_{ep} is the number density of primary electrons and ν_{ion} is the ionization frequency. In case of MISTRAL, the ionization of neutral gas by a beam of primary electrons results in the creation of secondary electrons and ions. The loss term L which represents the frequency of collision for the recombination process is negligible as compared to ionization frequency for weakly ionized plasmas and thus can be neglected.

Note that Eq. 3.7 is not sufficient to give information about the evolution of density n_j as it involves another quantity $\mathbf{v}_j$. One needs an equation for $\mathbf{v}_j$ which can be used in the continuity equation.

3.1.2.2. Momentum equation:

Multiplying Eq. 3.1 with $m_j\mathbf{v}_j$ and then integrating over the velocity space, we have,

$$n_j m_j\left[\frac{\partial \mathbf{v}_j}{\partial t} + (\mathbf{v}_j\cdot\nabla)\mathbf{v}_j\right] = q n_j\left(\mathbf{E} + \mathbf{v}_j\times\mathbf{B}\right) - \nabla\cdot\mathbf{P} + \mathbf{R} \tag{3.9}$$

This equation describes the momentum flow with m_j as the mass of the species j. The detailed derivation to obtain the momentum equation is given in [Che16]. The first term on the left-hand side denotes mass density times the acceleration and the second term is called the “inertial" term which represents acceleration for a continuous fluid flow. The first term on the right-hand side is simply the Lorentz force. The term $\nabla \cdot \mathbf{P}$ represents the divergence of the pressure tensor, sometimes called as stress tensor with the components, $P_{\alpha\beta} = mn\overline{v_\alpha v_\beta}$, where α, β denote the components direction and the bar represents the velocity averaged over the distribution function. If the distribution function is assumed to be an isotropic Maxwellian, then $\mathbf{P}$ reduces to the form,

$$\mathbf{P} = \begin{pmatrix} p & 0 & 0 \\ 0 & p & 0 \\ 0 & 0 & p \end{pmatrix} \tag{3.10}$$

Thus, $\nabla \cdot \mathbf{P}$ can be simply written as ∇p.

The off-diagonal terms are typically linked to the viscosity of the fluid. When particles collide in a fluid, they transfer momentum to nearby fluid elements, leading to a resistance to shear flow and the equalization of fluid velocities. This process, known as viscosity, is influenced by the mean free path, with longer mean free paths resulting in larger viscosities. In plasma, a similar effect occurs even in the absence of collisions. The Larmor gyration of particles, especially ions, causes them to explore different regions of the plasma, thereby equalizing fluid velocities in those regions. This collisionless process, driven by the Larmor radius rather than the mean free path, can be seen as a type of viscosity in plasmas. This collisionless viscosity, known as finite-Larmor-radius (FLR) effect, complements the role of collisional viscosity.

The FLR effect is particularly important in the momentum equation of plasma fluid models because it introduces a new term, known as the gyroviscous stress tensor written as $\nabla.\pi$ resulting in $\nabla.\mathbf{P} = \nabla p + \nabla.\pi$. FLR effects arise when the gyroradius of a charged particle becomes comparable to or smaller than the perpendicular wave number $k_\perp$ of the instability. Fig. 3.1 explains this.

During the gyromotion, particles encounter varying local conditions in the plasma, including fluctuations in plasma parameters such as density and temperature. As particles gyrate, they sample these fluctuations at different points in their trajectory. The distance traveled by a particle during a single gyromotion, known as the Larmor radius, sets the scale for this sampling process. When the gyroradius of a particle is small compared to the perpendicular wavenumber ($k_\perp \rho_i << 1$), the particle experiences a constant density throughout a single gyro-period and FLR effects can be neglected (Fig. 3.1 (a)). When the gyroradius is comparable to $k_\perp$, the particle encounters multiple perturbations per gyro-period, which can influence its growth rate as it averages over these fluctuations (Fig. 3.1 (b)). In the case where the gyroradius is large compared to the perpendicular wavenumber (Fig. 3.1 (c)), the particle observes a rapidly changing density resulting in a significant decrease in the growth rate of the

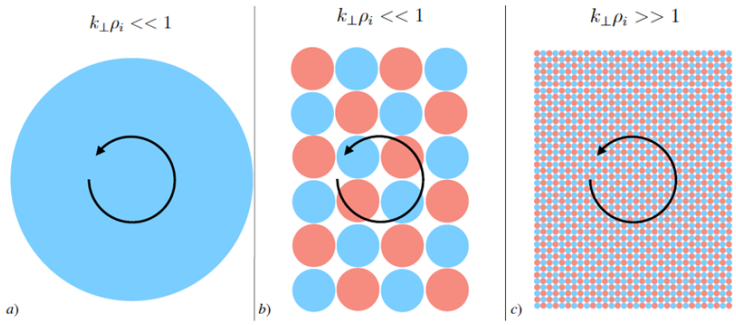

Figure 3.1.: Variation of FLR effect at different perpendicular wavenumber. The red and blue blobs represent the regions of overdensities and under densities respectively. The black arrow represents the direction of the particle's gyromotion. Extracted from [Par20].

instability.

The last term on the R.H.S of Eq. 3.9 represents the rate of momentum transfer per unit volume through collisions within the species and can be written as,

$$R = -\sum_k m_j n_j \nu_{jk} \left(\mathbf{v}_j - \mathbf{v}_k\right) \tag{3.11}$$

where the summation is performed over all the species, ν_{jk} is the collision frequency of the species j with the species k and $\mathbf{v}_j - \mathbf{v}_k$ is the relative velocity of the species k w.r.t species j.

The more common form of Eq. 3.9 is therefore,

$$n_j m_j \left[\frac{\partial \mathbf{v}_j}{\partial t} + (\mathbf{v}_j \cdot \nabla)\mathbf{v}_j\right] = q n_j \left(\mathbf{E} + \mathbf{v}_j \times \mathbf{B}\right) - \nabla p - \nabla \cdot \pi - \sum_k m_j n_j \nu_{jk} \left(\mathbf{v}_j - \mathbf{v}_k\right) \tag{3.12}$$

All fluid models require an assumption for closure. For instance, one can use the thermodynamic equation of state $p = n_j T_j$, assuming constant temperature in space and time:

$$\nabla p = T_j \nabla n_j \tag{3.13}$$

This holds true for fast time variations i.e. $\frac{\partial T_j}{\partial t} = 0$ such as in waves, when the fluid does not exchange energy with its surroundings; hence an energy conservation equation is not required. For slow time variations, where temperatures are allowed to equilibrate, an energy conservation equation is also required to determine p and T. A more detailed explanation of the plasma modeling using two-fluid theory is available in the standard textbooks [Che16], [LL05], [KT73].

3.1.3. Magnetohydrodynamics (MHD)

MHD provides a dynamical description of an electrically conducting fluid in the presence of magnetic fields at a macroscopic level. Instead of using two separate variables for ions and electrons as done in the multi-fluid description, the plasma is described as a simply charged fluid of total mass density $\rho = \sum_\sigma m_\sigma n_\sigma$, the center of mass velocity $\mathbf{U} = \sum_\sigma m_\sigma n_\sigma \mathbf{u}_\sigma / \rho$ and current density $\mathbf{J} = \sum_\sigma n_\sigma q_\sigma \mathbf{u}_\sigma$ which results in the following continuity and momentum equations,

$$\frac{\partial \rho}{\partial t} + \nabla \cdot (\rho \mathbf{U}) = 0 \tag{3.14}$$

$$\rho \left(\frac{\partial \mathbf{U}}{\partial t} + (\mathbf{U} \cdot \nabla)\mathbf{U} \right) = -\nabla p + \mathbf{J} \times \mathbf{B} \tag{3.15}$$

where p is the pressure. When coupled with the Maxwell equations, these equations result in a set of equations for the evolution of the electric field (Ohm's law equation) and the magnetic field (induction equation). The detailed description of MHD modeling can be found in [Bel06].

3.1.4. Kinetic vs. fluid modeling

For analytical and numerical treatment, solving the full kinetic Boltzmann equation (Eq. 3.1) is challenging. Additionally, the evolution of the distribution function in six-dimensional phase space could be too intricate for some issues. Fluid modeling is often useful for macroscopic global simulations of plasma as its reduced form and lower dimensionality allow faster simulations. Another advantage is that certain physical effects can be easily added or removed because of the “flexibility" of fluid equations. Keeping these advantages in mind, the physical phenomenon observed in the plasmas of interest has been explored using two-fluid modeling within the scope of this thesis.

The plasma modeling discussed above is employed as a tool to study instabilities in the given plasma system. The next section details the problem of instabilities in the plasma along with different types of instabilities already observed in the linear plasma columns.

3.2. Why study instabilities?

The first and foremost problem in tokamaks, as well as laboratory plasma devices, is the confinement of plasma. The presence of gradients perpendicular to the magnetic field represents a source of free energy in the plasma which can lead to the excitation of instabilities. These free energy sources cause the amplification of minor perturbations or fluctuations. In the linear phase, these perturbations grow exponentially in time.

As the linear instabilities grow in amplitude, they can eventually reach a point where nonlinear effects become significant. Nonlinear effects arise due to the interactions between different modes or waves, resulting in the transfer of energy between different scales and the nonlinear evolution of the plasma system. These interactions can lead to a redistribution of energy and the onset of plasma turbulence. Plasma turbulence refers to the state of a plasma where fluctuations occur across a broad range of scales and exhibit complex, irregular behavior. The broad consensus is that turbulence, appearance of coherent structures, and anomalous transport are caused by these instabilities. Controlling these instabilities could therefore be of great importance for enhancing the efficiency of magnetic fusion devices, laboratory plasma experiments, and for industrial applications as well.

In the scrape-off layer (SOL) of tokamaks, instabilities similar to those observed in linear devices have been identified to trigger radial transport by the creation of blobs, which are large, elongated plasma structures along magnetic field lines [MRD08], [Sug+10]. It is advantageous to use linear devices to study these instabilities because of their simple geometry than tokamaks.

3.3. Classification of instabilities

On a broader scale, instabilities appearing in plasmas with cross-field configurations can be classified depending on their parallel wave vector ($k_{||}$): flute instability and drift wave instability (see Fig. 3.2). Here $k_{||} = \mathbf{k}.\mathbf{B}/\mathrm{B}$ represents the component of the wave vector parallel to the magnetic field direction. In the case of flute waves, the dominant motion occurs perpendicular to the magnetic field lines. Therefore, $k_{||}$ is often small or negligible compared to the perpendicular wave number ($k_{\perp}$). Drift waves, on the other hand, are associated with non-zero parallel wavenumber i.e. $k_{||} > 0$.

Another criterion to identify flute and drift waves is based on the phase difference (ϕ_p) between density ($\tilde{n}$) and electric potential perturbation ($\tilde{\phi}$). The growth of instability depends critically on the phase shift between the two perturbations, as will be shown in Table 3.1. The initial perturbation does not grow in the case of a pure drift wave as $\phi_p = 0$ or π which consequently makes the $\mathbf{E}\times\mathbf{B}$ particle flux zero [Jas72]. In contrast, when $\phi_p = \pi/2$, which is a flute wave characteristic, the growth is maximum as the $\mathbf{E}\times\mathbf{B}$ fluxes act to amplify the initial perturbation.

Instabilities can further be divided into four main categories on the basis of free energy available to drive them [Che16]. A discussion of the various kinds of instabilities which have been observed in general is outside the scope of this work. However, a few of them relevant to the existing work will be discussed.

Drift waves, centrifugal instability, Kelvin - Helmholtz instability, and neutral drag instability have been observed in a number of laboratory plasma experiments [Bro+06],

Figure 3.2.: (a). Flute mode with $k_{\parallel} = 0$ (Source [Che16])(b). Screw mode with $k_{\parallel} > 0$ (Source [Che16]).

[Jas72], [MEW86], [Ili+73], [Leh71], [WP73]. Centrifugal instability, Kelvin - Helmholtz instability and neutral drag instability are associated with zero parallel wavenumber ($k_{\parallel}$), classifying as flute wave instabilities. The following section briefly discusses the general mechanism of these instabilities to give an intuition of how these instabilities develop.

3.3.1. Drift waves

The drift wave develops from a density gradient and the parallel motion of the electrons. The coupling between the density perturbation $\tilde{n}$ and the potential perturbation $\tilde{\phi}$ gives rise to drift wave instability. It is called '*universal instability*' by Chen because its main ingredients exist in most magnetically confined plasmas.

3.3.1.1. General characteristics

First considering the case of adiabatic electrons, i.e. neglecting the impact of collisions on the motion of electrons, the density of electrons is given by Boltzmann relation [LL05],

$$n = n_0 \; exp\left(\frac{e\tilde{\phi}}{k_B T_e}\right) \tag{3.16}$$

where n_0 is the equilibrium density and $\tilde{\phi}$ is the perturbed potential. Writing $n = n_0 + \tilde{n}$ where n_0 is the equilibrium component and $\tilde{n}$ denotes the fluctuating component of number density and assuming that $e\tilde{\phi} << k_B T_e$, one gets:

$$\tilde{n} = n - n_0 = n_0 \left(exp\left(\frac{e\tilde{\phi}}{k_B T_e}\right) - 1\right) \tag{3.17}$$

$$\tilde{n} \approx n_0 \frac{e\tilde{\phi}}{k_B T_e} \tag{3.18}$$

A perturbation in density is therefore directly associated with a perturbation in potential and an electric field is created between the density perturbation and the surrounding plasma. When a zone of higher density appears in a plasma, the ions and electrons move in such a way as to counter this excess of particles. Both species diffuse outside the high-density zone. But since ions have a lot more inertia than

electrons, the disturbance will be positively charged. In the presence of a magnetic field perpendicular to this electric field, an $\mathbf{E} \times \mathbf{B}$ force will act on the density perturbation and induces the rotation of the plasma. The situation is described in Fig. 3.3 (a).

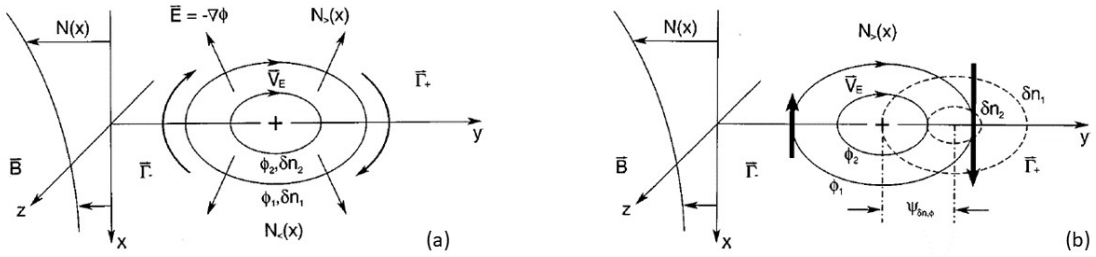

Figure 3.3.: Drift wave mechanism (a). When density and potential fluctuations are in phase (b). When density and potential fluctuations are out of phase. Source [Hor99]

When finite dissipation of the parallel electron momentum is included, the electrons can lose momentum to the background plasma as they move parallel to the magnetic field. The potential perturbations are phase shifted relative to the density fluctuations with

$$\tilde{n} \approx n_0 \frac{e\tilde{\phi}}{k_B T_e} (1 + i\delta) \tag{3.19}$$

where $\delta \neq 0$. This phase shift introduces a net convection of density by $\mathbf{E}\times\mathbf{B}$ flow associated to the initial perturbation which tends to amplify it. The situation is shown in Fig. 3.3 (b). A more detailed explanation of drift wave instability and its mechanism can be found in [Hor99], [GM09].

3.3.2. Centrifugal/Rayleigh-Taylor instability

As the name suggests, this instability arises due to the interaction between the centrifugal force, which acts to move objects (plasma) away from the axis of rotation, and other forces or gradients in the system. Centrifugal instability is analogous to Rayleigh-Taylor (RT) instability [Sha84] developed in fluids.

Fig. 3.4 illustrates the physical mechanism of RT instability. Imagine that the plasma vacuum surface is perturbed. The ions are electrons initially drift along the x-direction due to gravitational force and equilibrium magnetic field with a velocity, $\mathbf{v}_{gj} = \frac{m_j \mathbf{g}\times\mathbf{B}}{q_j B^2}$ where $j = i, e$ stands for ions and electrons respectively. Since this velocity is directly proportional to mass to charge ratio (m_j/q_j), ions and electrons will drift apart causing a charge imbalance. This will result in the formation of the perturbed electric field E_1 and the ions and electrons will drift in the y-direction due to the force of the electric field and equilibrium magnetic field with a velocity, $v_E = \frac{\mathbf{E_1}\times\mathbf{B_0}}{B^2}$. The $\mathbf{E_1}\times\mathbf{B}$ will be directed in such a way as to drive the areas of high density upwards and the areas of lower density downwards which amplifies the initial disturbance. This will

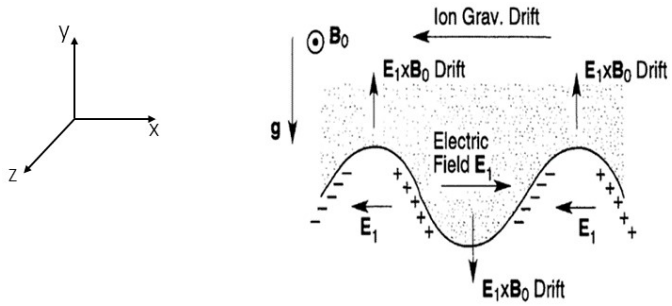

Figure 3.4.: Physical mechanism of Rayleigh-Taylor instability in cartesian coordinates. Extracted from [KT73].

create a phase difference between density and potential perturbation. It can be noted that the movement of electrons along the magnetic field lines does not intervene in the explanation of the mechanism of the Rayleigh-Taylor instability. Indeed, this instability has a zero wave number along the field lines and therefore comes under the category of “flute" modes.

In RT instability as explained above, plasma from high-density regions and low-density regions tend to interchange their position, therefore, it is also called interchange instability. Another common term is centrifugal instability, which emphasizes on the difference in the rotational speed between two fluids.

3.3.3. Kelvin-Helmholtz instability

The Kelvin-Helmholtz (KH) instability is another type of flute instability that develops from a sheared $\mathbf{E} \times \mathbf{B}$ flow [DAn65], [KJC69]. When there is a large velocity shear between two layers of matter, the faster layer will drive a minor disturbance at the interface between the layers, which will then expand in spiral wraps. The instability develops because the kinetic energy of the system is higher when the two layers of fluid remain separated than when they mix and move forward at a common speed. Examples of the K-H instability in nature include wind-induced water waves, water flow in the river in different directions and cloud vortices formed by strong airflow.

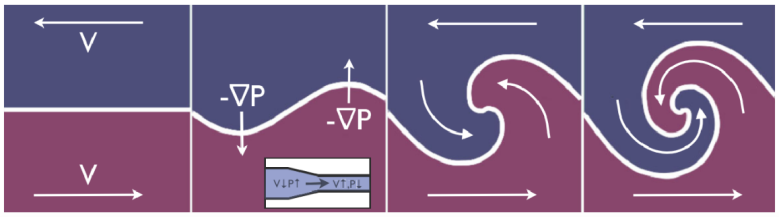

Figure 3.5.: The Kelvin-Helmholtz Instability growing on a shear boundary. Source [JWD14]

The mechanism of K-H instability at the interface between two fluids with velocity shear is shown in Fig. 3.5. According to the Bernoulli principle, when a boundary

is perturbed into a flowing fluid, it generates a constriction that increases velocity and decreases pressure, while when the boundary is expanded, the flow is reduced and the pressure is increased. As a result, when the boundary between two flowing fluids gets perturbed, there is a pressure gradient in the direction opposite to that of the boundary deformation, which creates a pressure force in the same direction. As a result, the boundary deformation will increase and eventually cause the K-H instability [JWD14].

3.3.4. Neutral drag instability

This type of instability was first identified by Simon[Sim63] and Hoh[Hoh63a] in cross field plasmas. They showed that a charge separation occurs in the azimuthal direction as a result of the plasma rotating due to a radial electric field and the associated drag force from ion-neutral collisions. The resulting electric field can drive the plasma outwards and amplifies the perturbation. The discussed mechanism is presented in the Fig. 3.6.

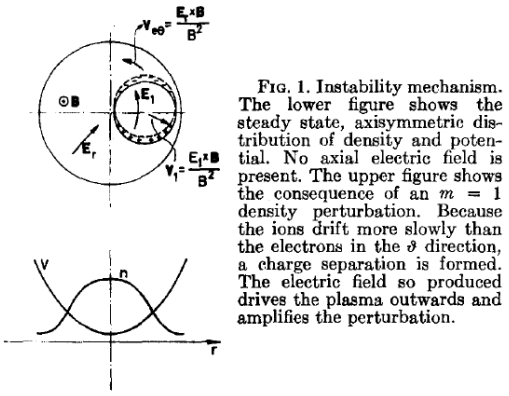

FIG. 1. Instability mechanism. The lower figure shows the steady state, axisymmetric distribution of density and potential. No axial electric field is present. The upper figure shows the consequence of an $m = 1$ density perturbation. Because the ions drift more slowly than the electrons in the ϑ direction, a charge separation is formed. The electric field so produced drives the plasma outwards and amplifies the perturbation.

Figure 3.6.: Mechanism of neutral drag instability.Source[Hoh63a]

3.4. Overview of existing models to study instabilities in cross-field plasmas

When studying instabilities in plasma physics, we are interested in the conditions under which a wave will grow in amplitude. The dispersion relation (see section 4.2.2) allows us to determine the conditions under which a particular wave mode will grow, and the growth rate of the instability. By analyzing the dispersion relation, we can determine whether a plasma is stable or unstable and how it will evolve over time in the initial phase of the instability. Additionally, dispersion relations can provide insight into the physical mechanisms responsible for the instabilities in a plasma. By understanding the dispersion relation, we can identify the driving forces behind the

instability and develop strategies for controlling or mitigating the instability.

Before delving into the intricacies of the dispersion relation, it is worth noting which models already exist for studying instabilities in **E**×**B** plasma systems and why the existing models do not provide adequate information for the instability description of weakly magnetized plasma devices like MISTRAL.

In the past decades, many models have been proposed to study instabilities in $\mathbf{E}\times\mathbf{B}$ plasmas. The centrifugal instability and its stabilization by finite Larmor radius effects were first explained by Rosenbluth et al. [RKR62]. They explained the stability of a rotating cylindrical plasma column in the frame of kinetic theory, valid for low β plasma for $k\rho_i < 1$ and $\omega/\omega_{ci} \approx (k\rho_i)^2$ where ω is the plasma perturbation frequency, ω_{ci} is the ion cyclotron frequency, k is the wave vector of the perturbation and ρ_i is the ion Larmor radius. Terms of the order of $(k\rho_i)^2$ have been retained and higher-order terms have been neglected. Rotating plasma columns were shown to be prone to centrifugal instability that stems from the difference between the azimuthal velocity of ions and electrons caused by inertia.

Roberts et al. [RT62] and Lehnert [Leh62] explained the centrifugal instability in rotating plasmas using the fluid magnetohydrodynamic (MHD) equations in the slab geometry. [RT62] neglected the Coriolis force whereas [Leh62] neglected all the pressure gradients. The results were based on a strong assumption that the equilibrium flow frequency (ω_0) is negligible in comparison to the ion-cyclotron frequency i.e. $\omega_0 \ll \omega_{ci}$.

Chen [Che66] verified the results of [RKR62] using a two-fluid model, under the low-frequency assumption (LFA) i.e. $\omega_{ph} \ll \omega_{ci}$ where ω_{ph} is the Doppler shifted frequency given by $\omega_{ph} = \omega - m\omega_0$. Here m is the azimuthal mode number. In this treatment, both the mode frequency and equilibrium flow frequency are ordered small, with $\omega_{ph}/\omega_{ci} = O(\rho^2)$, $\rho << 1$ is the magnetization parameter defined as $\rho = \rho_i/l$ where l is the scale length of macroscopic gradients. Chen studied the influence of finite Larmor radius and magnetic shear on linear stability. He also extended the model to the regime of fast rotation by assuming $\omega_{ph}/\omega_{ci} = O(\rho)$.

As an extension of the above-referenced work, Rognlien [Rog73] gave analytical and numerical solutions of low-frequency electrostatic waves ($\omega << \omega_{ci}$) in a radially bounded plasma column for lower azimuthal mode numbers ($m = 1, 2$) for uniform as well as non-uniform rotation.

Recently, Gueroult et al. [GRF17] have studied the centrifugal instability for an $\mathbf{E}\times\mathbf{B}$ plasma column in the regime of fast rotation ($|\omega_0 - \omega_{0e}|/\omega_{ci} \approx O(1)$ where ω_{0e} is the equilibrium flow frequency of electrons) with no constraint on the perturbation frequency ω. The analysis was performed in the radially local limit and focused on the case of a radially outward electric field, $E_r > 0$.

A few attempts were also made to study the influence of ion-neutral collisions on uniformly as well as non-uniformly rotating plasma systems. A local, single-fluid theory that incorporates the effects of Coriolis and centrifugal force, finite Larmor radius effects, and ion-neutral collisions was derived by Wheeler and Pyle [WP73] using the slab geometry. However they excluded the terms that cause the destabilization by ion-neutral collisions, therefore simply reporting a stabilizing collisional effect. D'Ippolito and Krall [DK74] extended the work done by [WP73] by providing a theory that includes both centrifugal and neutral drag instability modified by Coriolis and finite Larmor radius effects. They use the rectangular slab geometry and the local approximation as well.

Chu et al. [Chu+69] derived the same differential equation to explore the linear stability of uniformly rotating plasmas as derived by [Che66] using the two-fluid model. They also include the effect of ion collisional viscosity and finite parallel wavenumber which introduces the additional phenomenon of stabilization of drift waves by ion collisional viscosity. Perkins and Jassby [PJ71] extended the work done by [Chu+69] by including the non-uniformity of electric field and hence including the effect of shear on the linear stability of rotating plasmas.

Jassby [Jas72] extended the work done in [PJ71] by offering a thorough examination of the applicability of the low-frequency fluid equations and a careful comparison with the measured characteristics of instabilities caused by shear in the rotation frequency. He also provided a detailed criterion to compare several properties of the three types of low-frequency instabilities and is shown in Table 3.1.

Property	Kelvin-Helmholtz	Centrifugal	Resistive drift
$k_{\|\|}$ for maximum growth	0	0	$\approx L^{-1}$
$\|e\tilde{V}_p/k_B T_e\|/\|\tilde{n}/n\|$	$>>1$	≥ 1	≤ 1
local radial phase shift	$90^\circ - 180^\circ$	$45^\circ - 90^\circ$	$< 45^\circ$
$\|e\tilde{V}_p/k_B T_e\|_{max}$	$>>1$	1	1

Table 3.1.: Comparison of low-frequency instability properties. Source[Jas72].

Lastly, Sosenko et al. [SP00] use the two-fluid model to study analytically the linear and nonlinear properties of collective oscillations in a cylindrical magnetized laboratory plasma. They also employed the LFA while deriving the differential equation to have a solution for the global drift modes. They came to the conclusion that the fundamental local and global dispersion relations for the low-frequency drift waves are not generally valid in the reported observations as the unstable modes occur at

frequencies in the range of the ion-cyclotron frequency and its harmonics.

As explained above, most of the models formulated so far to study $\mathbf{E} \times \mathbf{B}$ plasmas are based on the LFA ($\omega_{ph} << \omega_{ci}$) and therefore not suitable for weakly magnetized linear plasma devices such as MISTRAL [Jae10], RAID [Fur+17], and VKP [Pli+14] where the frequency values, ω, and ω_0, are typically comparable to the ion cyclotron frequency ω_{ci}. Therefore, it is possible that if the LFA is eliminated, the criterion provided by [Jas72] in Table 3.1 might not satisfy the instability description.

In MISTRAL, one requires a description that is applicable without any frequency limitations as the equilibrium frequency and mode frequency can vary from a small to a large fraction of the cyclotron frequency. Furthermore, the finite Larmor radius effects (FLRE) and the collisions of charged particles with neutrals are important for the modelization of plasma instabilities in these laboratory devices as will be shown in Section 4.1.2 and 4.1.3.

3.5. Exploring potential instabilities in MISTRAL plasma column

The axial wave number on MISTRAL has been measured to be at least significantly less than $2\pi/L$, where L is the length of the plasma column, suggesting flute modes [Jae10], therefore omitting the possibility of the existence of drift waves. In most of the cases discussed in Chapter 2 the plasma potential profile is parabolic (rigid body rotation) indicating uniform $\mathbf{E}\times\mathbf{B}$ rotation. In these cases, the absence of sheared $\mathbf{E}\times\mathbf{B}$ rotation rules out the possibility of K-H instability as well.

Considering the aforementioned flute instabilities, the focus narrows down to the centrifugal and neutral drag instability or a combination of both as the prime candidates. To initiate the investigation, the characteristics of the centrifugal instability will be examined first, followed by an exploration of the neutral drag instability.

3.6. Summary

Different types of modeling techniques employed to study plasma behavior are discussed. Various class of instabilities that can exist in weakly magnetized plasma columns is given. Based on the discussion, centrifugal and neutral drag instabilities are found to be the potential candidates to develop in MISTRAL plasmas.

4. Fluid modeling of MISTRAL

In this Chapter, the range of plasma parameters essential for analyzing plasma dynamics is established in line using the plasma characteristics obtained with standard experimental conditions in Chapter 2. Then the fluid modeling for the instability description is discussed solving the equilibrium flow for ions and electrons for the given plasma system.

4.1. Range of plasma parameters in MISTRAL plasma column

To build a model appropriate for the description of MISTRAL plasmas, knowledge of the typical plasma conditions encountered in the device is required. In MISTRAL, the plasma density of the column varies from 10^{14} to a few 10^{16} m^{-3} and the electron temperature varies from 2 - 6 eV, depending on the configuration of the experiment.

Number density (n)	$10^{14} - 10^{16}$ m^{-3}
Electron temperature (T_e)	2-6 eV
Ion temperature (T_i)	0.2 eV

Table 4.1.: Range of number density, electron temperature, and ion temperature in MISTRAL plasma column

The ion temperature is typically measured slightly above the room temperature by LIF measurements [Reb10]. In the following, we will use T_i=0.2 eV and derive typical time and length scale characteristics of MISTRAL plasma.

4.1.1. Plasma beta

In order to comprehend plasma dynamics, plasma beta is an essential physical quantity. It explains how magnetic processes as opposed to thermodynamic ones, dominate plasma motion. It is given by the ratio of plasma pressure $p = nT_j$ and the magnetic pressure $B^2/2\mu_0$,

$$\beta = \frac{nT_j}{B^2/2\mu_0} \tag{4.1}$$

where $\mu_0 = 1.257 \times 10^{-6}\ mKgs^{-2}A^{-2}$ is the permeability of free space. Using $n \approx 3 \times 10^{15}\ m^{-3}$, $T_e \approx 3\ eV$ at B=160 G,

$$\beta \approx 1.4 \times 10^{-6} \tag{4.2}$$

As β is low, the plasma pressure is not strong enough to significantly affect the magnetic field structure. As a result, the magnetic field remains relatively unperturbed, and plasma dynamics are mainly determined by electric fields and the motion of charged particles. Under these conditions, the electrostatic model provides a reasonable approximation for studying the behavior of the plasma.

4.1.2. Collisions

As the plasma of interest in this thesis is weakly ionized [SPR09] i.e. the fraction of charged particles is small as compared to neutral particles. The electron-neutral and ion-neutral collisions are, therefore, important in this case. The collisions between electrons and ions with neutrals can be divided into two categories: elastic and inelastic collisions. In an elastic collision, the total kinetic energy of the colliding particles remain conserved. If the total kinetic energy is not conserved during the process, the collision is considered inelastic.

In an elastic collision between an electron or ion with a neutral gas particle, the charged particle transfers some of its momentum to the neutral keeping the total kinetic energy conserved. This results in a deviation in the trajectory of the charged particle due to its impact with the neutral.

In an inelastic collision, the total kinetic energy is not conserved. When a charged particle collides with a neutral particle, it can transfer energy to excite or ionize the neutral. This can lead to a cascade of ionization, resulting in the creation of more charged particles.

The type of collision that occurs depends on various factors, such as temperature, density, charge, and mass of the particles involved. In weakly ionized plasmas, where the number of charged particles is relatively low, collisions between charged and neutral particles are more likely to be elastic, but inelastic collisions can also occur, leading to further ionization and excitation of neutral particles.

4.1.2.1. Collision frequency

The cross-section σ is a fundamental quantity that characterizes the probability of collision between the particles. It is the measure of the effective area of interaction between two particles. This can be well understood with the help of the Fig. 4.1,

If an incident particle 'a' with a velocity v_a is moving towards the field of target

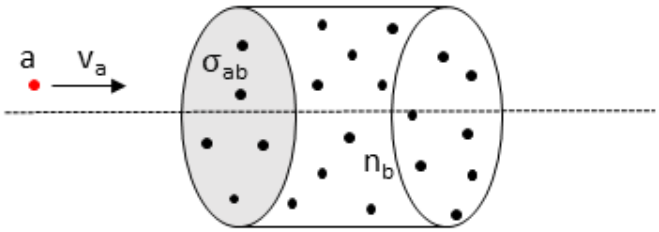

Figure 4.1.: Interaction of an incident particle 'a' with the population of target particles 'b' within the area σ_{ab}

particle 'b' with the number density n_b, then the collision between two particles is possible only if 'a' undergoes an interaction with 'b' within the surface σ_{ab}. From σ_{ab}, another parameter, the mean free path λ can be defined which gives the average distance traveled by the particle between two successive collisions and is given by,

$$\lambda = \frac{1}{n_b \sigma_{ab}} \tag{4.3}$$

As the velocity of the incident particle is v_a, the mean time between the interactions is,

$$\tau_{int} = \frac{\lambda}{v_a} \tag{4.4}$$

The inverse of this interaction time is the collision frequency,

$$\nu_{ab} = n_b \sigma_{ab} v_a \tag{4.5}$$

One thing to note here is that the above formula defines the collision frequency at the particle level. The expression for macroscopic collision frequency can be obtained by taking an average of the above expression,

$$\nu_{ab} = n_b < \sigma_{ab} v_a >_v = n_b K \tag{4.6}$$

where $K =< \sigma_{ab} v_a >_v$ is the reaction rate constant in $m^3 s^{-1}$ with $< . >_v$ as the velocity average of the bracketed quantity over f which is often assumed to be a Maxwellian distribution with the temperature T in eV.

4.1.2.2. Orders of magnitude

To calculate the electron-neutral and ion-neutral collision frequencies required thereafter, information about the number density of neutrals and rate constant is required. Using the LIF diagnostic, the velocity distribution function for neutrals was measured

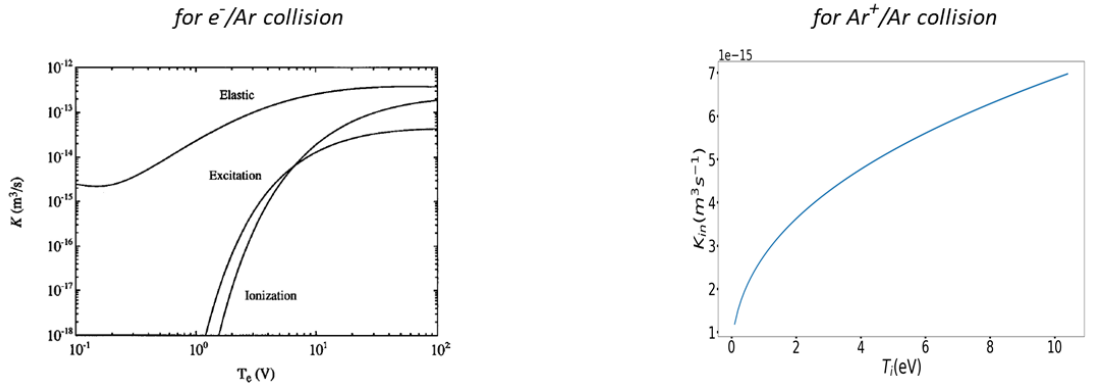

Figure 4.2.: Rate constant for elastic momentum transfer cross-section for e^- / Ar collision [LL05] as a function of electron temperature T_e (left). The rate constant for elastic momentum transfer cross-section for Ar^+ / Ar collision as a function of ion temperature T_i (right).

in the previous works on MISTRAL and it was observed that the neutrals remain at an ambient temperature. Therefore, considering the neutrals at an ambient temperature T_n = 300 K corresponding to the pressure range of $P_n = 10^{-5}$ mbar - 10^{-3} mbar = 10^{-3} Pa - 10^{-1} Pa , the number density of neutrals n_n can vary from,

$$n_n = \frac{P_n}{k_B T_n} \approx 2.4 \times 10^{17} \ \ m^{-3} - 2.4 \times 10^{19} \ \ m^{-3} \tag{4.7}$$

The rate constant K_{in} for Ar^+ / Ar collisions is evaluated by integrating over the velocity distribution functions of ions,

$$K_{in}(T_i) = \left(\frac{m}{2\pi k_B T_i}\right)^{3/2} \int_0^\infty \sigma(T_i)\ v\ \exp\left(-\frac{m v^2}{2 k_B T_i}\right) 4\pi v^2 dv \tag{4.8}$$

where $\sigma(T_i)$ is the elastic momentum transfer cross-section for Ar^+ / Ar collision given in [Phe94] as,

$$\sigma(T_i) = 1.15 \times 10^{-18} (T_i^{-0.1})(1 + 0.015/T_i)^{0.6} \tag{4.9}$$

with T_i as the ion temperature in eV. For electrons, direct reference has been taken from the data about the rate constant for e^- / Ar elastic collision given in [LL05].

Using this information, the rate constant for Ar^+ / Ar elastic collision (K_{in}) corresponding to $T_i \approx 0.1 \ \ eV$ and for e^- / Ar elastic collisions (K_{en}), corresponding to $T_e \approx 3$ eV is ,

$$K_{in} \approx 1.5 \times 10^{-15} \ m^3 s^{-1}, \ \ K_{en} \approx 10^{-13} \ m^3 s^{-1} \tag{4.10}$$

which on using together with Eq. 4.7 in Eq. 4.6 gives a range of ion-neutral and electron-neutral collision frequencies for a given pressure range as,

$$\nu_{in} = 0.36 \text{ kHz} - 36.2 \text{ kHz}, \ \ \nu_{en} = 24 \text{ kHz} - 2.4 \text{ MHz} \tag{4.11}$$

Coulomb collisions

Coulomb collisions refer to the long-range scattering events between charged particles due to the mutual exchange of the Coulomb force. The average Coulomb collision frequency between charged particles can be calculated by the formulae given by [GR95] which gives electron-ion and electron-electron collision frequencies as,

$$\nu_{ee}^{C} \simeq \nu_{ei}^{C} \simeq \frac{2^{1/2} n e^4 ln\Lambda}{12\pi^{3/2}\epsilon_0^2 m_e^{1/2} T_e^{3/2}} \tag{4.12}$$

where the Coulomb logarithm $ln\Lambda$ is given by,

$$ln\Lambda = ln\left(\frac{\lambda_D}{b}\right) \tag{4.13}$$

$$\text{with} \quad \lambda_D = \sqrt{\frac{\epsilon_0 k_B T_e}{n e^2}}, \quad \text{the Debye length} \tag{4.14}$$

$$\text{and} \quad b = \frac{e^2}{4\pi\epsilon_0 m_e v_{the}}, \quad \text{the impact parameter} \tag{4.15}$$

Using $n \approx 10^{14} \ \ m^{-3} - 10^{16} \ \ m^{-3}$, $T_e \approx 3$ eV and other required parameters, the range of electron-ion coulomb collision frequency is,

$$\nu_{ee}^{C} \simeq \nu_{ei}^{C} \simeq 760 \text{ Hz} - 76 \text{ kHz} \tag{4.16}$$

The ion-ion Coulomb collision frequency (ν_{ii}^{C}) is,

$$\nu_{ii}^{C} \simeq \frac{n Z^4 e^4 ln\Lambda}{12\pi^{3/2}\epsilon_0^2 m_i^{1/2} T_i^{3/2}} \tag{4.17}$$

For Ar^+ ions, taking $n \approx 10^{14} - 10^{16} \ m^{-3}$, $T_i \approx 0.2$ eV, $Z = 1$, ν_{ii}^{C} evaluates to,

$$\nu_{ii}^{C} \simeq 125 \text{ Hz} - 10.6 \text{ kHz} \tag{4.18}$$

4.1.3. Magnetization

As the plasma column is subjected to an external magnetic field, the trajectories of the charged particles can be significantly altered as they rotate around the magnetic field lines direction executing circular Larmor radius or gyroradius which is given by,

$$\rho_j = \frac{v_{thj}}{\omega_{cj}} \tag{4.19}$$

where ω_j is the cyclotron frequency also known as gyrofrequency,

$$\omega_{cj} = \frac{|q|B}{m_j} \tag{4.20}$$

The resulting helical orbits are more tightly wound as the field intensity rises, thereby binding particles to magnetic field lines. For a species j to be magnetized in the plasma system, the Larmor radius ρ_j should be smaller than the characteristic length l of the system which gives the condition of magnetization as,

$$\delta = \frac{\rho_j}{l} << 1 \tag{4.21}$$

where δ is the magnetization parameter. Here the characteristic length l refers to the length perpendicular to the magnetic field direction i.e. the radius of the plasma column.

Another parameter that determines the magnetization condition is the collision frequency. The trajectory of a charged particle can be changed by a collision with another particle before completing a gyro-orbit which can lead to a change in direction of motion. An ion, for example, travels in a different direction after colliding with a neutral atom as shown in Fig. 4.3.

Another condition for magnetization is thus,

$$\nu_{jk} << \frac{\omega_{cj}}{2\pi} \tag{4.22}$$

Therefore, for electrons and ions to be magnetized in a given plasma system, both the spatial and temporal conditions should be satisfied. Plasmas exhibiting these two forms of magnetization are referred to as Larmor magnetized ($\rho_j/l << 1$) and collisionally magnetized ($2\pi\nu_{jk}/\omega_{cj} << 1$), respectively. If ($2\pi\nu_{jk}/\omega_{cj} \approx 1$), the plasma can be considered partially magnetized.

The Larmor magnetization level inside the MISTRAL plasma column where the magnetic field B ranges from 100 G - 340 G has been computed for electrons and ions for Ar plasma as shown in Fig. 4.4 and for He, Kr, and Xe ions in Fig. 4.5. As $\rho_e << l$ where l = 10 cm is the characteristic length scale of the perpendicular dynamics, the electrons can be considered strongly magnetized for the given range of magnetic field. The magnetization condition is fulfilled for ions only at high magnetic field.

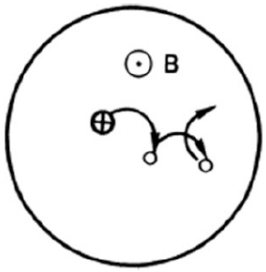

Figure 4.3.: Diffusion of gyrating particles by collisions with neutral atoms. Source[Che16]

As the number density of neutrals is high in the present plasma system, the trajectory of electrons and ions can be changed by colli-

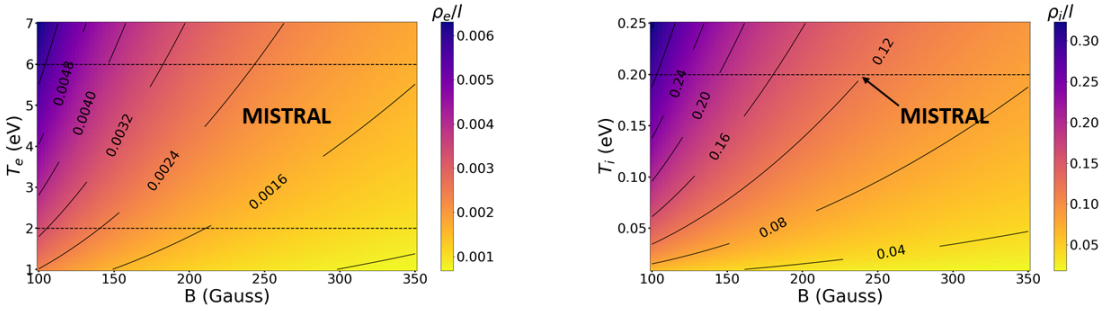

Figure 4.4.: Variation of normalized Larmor radius of electron (ρ_e/l) with the magnetic field B and electron temperature (T_e) (left) and Variation of normalized Larmor radius of ion (ρ_i/l) with the magnetic field B and ion temperature (T_i) (right) for Ar. The dashed region in curves indicates the region relevant to MISTRAL.

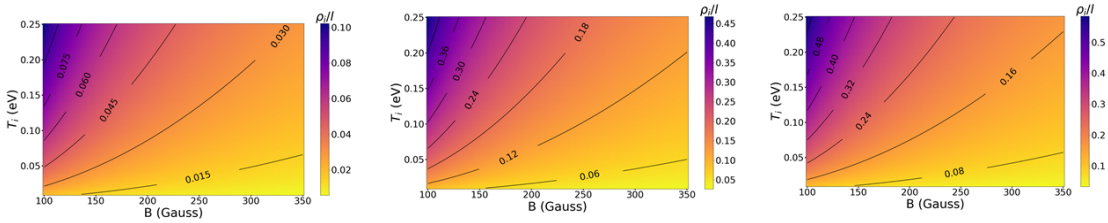

Figure 4.5.: Variation of normalized Larmor radius of ion (ρ_i/l) with the magnetic field B and ion temperature (T_i) for He (left), Kr (middle), and Xe (right).

sion with the neutral particles which can lead to demagnetization of the given charged species (see Fig. 4.3). The condition on the collision frequencies has also been checked for collisions between electrons and ions with neutrals for Ar as shown in Fig. 4.6 and for He, Kr, and Xe in Fig. 4.7 for a given range of pressure range and magnetic field.

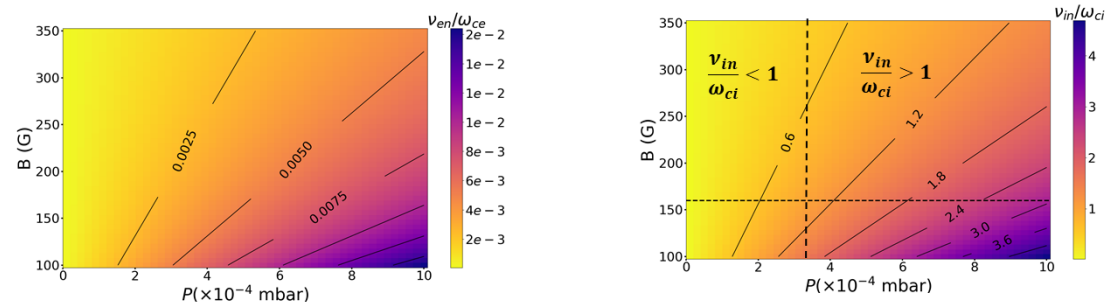

Figure 4.6.: Variation of electron-neutral collision frequency normalized to electron cyclotron frequency (ν_{en}/ω_{ce}) (left) and Variation of ion-neutral collision frequency normalized to ion cyclotron frequency (ν_{in}/ω_{ci}) (right) for Ar for a given range of pressure and magnetic field. The dashed lines on the right figure indicate low collisionality ($\nu_{in}/\omega_{ci} < 1$) and high collisionality regimes ($\nu_{in}/\omega_{ci} > 1$).

The collision frequency of electrons with neutrals is of the order of MHz in compar-

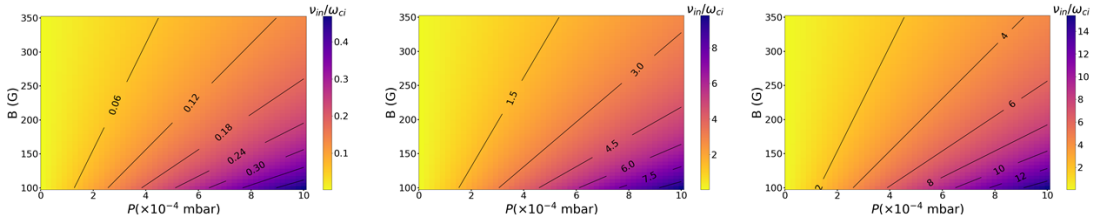

Figure 4.7.: Variation of ion-neutral collision frequency normalized to ion cyclotron frequency (ν_{in}/ω_{ci}) for He (left), Kr (middle), and Xe (right) for a given range of pressure and magnetic field.

ison to electron cyclotron frequency which is of the order of GHz and thus $\nu_{en} \ll \omega_{ce}$. The temporal condition is only partially satisfied for collisions between ions and neutrals for Ar and He at low pressure and not at all satisfied in the case of Kr and Xe.

Note: It should be noted that there exists a pressure range for which plasma potential shows a monotonic behavior at a fixed magnetic field strength (see Fig. 2.18) as shown for reference case B in Chapter 2. After analyzing Fig. 4.6 (right), it seems that the non-monotonicity in the plasma potential occurs when the ion-neutral collision frequency surpasses the ion-cyclotron frequency or in other words when $\nu_{in}/\omega_{ci} > 1$. For the pressure range at a fixed magnetic field for which $\nu_{in}/\omega_{ci} < 1$, the plasma potential follows a parabolic profile (see Fig. 2.17). The two regions have been highlighted in Fig. 4.6 (right) with two dashed lines. A more detailed investigation should be done in this regard.

4.1.4. Quasi-neutrality

A quasi-neutral plasma model assumes the electron density to be equal to the ion density at every point in space and time [Che16]. A plasma can be considered as a quasi-neutral medium if the Debye length λ_D is much smaller than the typical length scales of the phenomenon to be studied and the inverse of the frequencies involved are much smaller than the plasma frequency $\omega_{pi,e}$. The Debye length and plasma frequency are given by [Che16],

$$\lambda_D = \sqrt{\frac{\epsilon_0 T_e}{ne^2}}, \quad \omega_{pj} = \frac{v_{thj}}{\lambda_D} \quad \text{with} \quad v_{thj} = \sqrt{\frac{T_j}{m_j}} \tag{4.23}$$

where $\epsilon_0 = 8.854 \times 10^{-12}\ Fm^{-1}$ is the permittivity of free space, e is the electronic charge, v_{thj} is thermal speed and m_j is the mass of the species. Substituting the required values in Eq. (4.23) from Table 4.1, we obtain the range of various lengths and time scales of the plasma system under consideration.

Here $\lambda_D << R$ and the frequencies involved are much smaller than the corresponding plasma frequencies ($\omega_{pi,e}$) as shown in table 4.2. Therefore, one can ensure quasi-neutrality to be valid for MISTRAL plasmas and hence quasi-neutral plasma

Debye length	λ_D	1.3 mm - 0.13 mm
Ion thermal speed	v_{thi}	692 ms^{-1}
Electron thermal speed	v_{the}	593 kms^{-1} - 1027 kms^{-1}
Ion Larmor radius	ρ_i	18 mm
Electron Larmor radius	ρ_e	0.2 mm - 0.4 mm
Ion plasma frequency	ω_{pi}	0.53 MHz - 5.3 MHz
Electron plasma frequency	ω_{pe}	0.46 GHz - 7.9 GHz
Ion-neutral collision frequency	ν_{in}	0.36 kHz - 36 kHz
Electron neutral collision frequency	ν_{en}	24 kHz - 2.4 MHz
Electron-ion Coulomb collision frequency	ν_{ei}^C	760 Hz - 76 kHz
Electron-electron Coulomb collision frequency	ν_{ee}^C	760 Hz - 76 kHz
Ion-Ion Coulomb collision frequency	ν_{ii}^C	125 Hz - 10.6 kHz
Plasma column length	L	1 m
Cylinder radius	R	10 cm
Ionization rate	-	>> 1%

Table 4.2.: Typical length and time scales in MISTRAL plasma. To calculate the required range of λ_D, n is varied from $n \approx 10^{14} - 10^{16}\ m^{-3}$ as given in table 4.1 and $T_e \approx 3$ eV is used.

models can be considered as a good approximation to be used within the scope of this work.

The plasma conditions validated above will form the basis of the fluid model required for the description of MISTRAL plasma and will be the topic of the next section.

4.2. Fluid modeling for instability description

We use a two-fluid formalism to study the stability of weakly magnetized rotating plasma columns. We consider a cylindrical plasma bounded radially and immersed in a homogeneous magnetic field such that $\mathbf{B} = B\ \hat{e}_z$. Based on the experimental characteristics of MISTRAL and the plasma conditions discussed above, we make the following assumptions,

4.2.1. Assumptions and Model equations

- Electrostatic approximation is used such that $\frac{\partial B}{\partial t} = 0$.
- The magnetic field is uniform along the axial direction i.e. $\mathbf{B} = B\hat{e}_z$.
- The fluctuations along the axial direction are neglected i.e. $k_{||} = 0$.
- Parabolic profile for plasma potential, this assumption is not valid at high pressure.

- Ion temperature T_i is assumed to be radially uniform. The electron temperature varies radially following a Gaussian distribution such that $T_e = T_{e0}\ exp\ \left(-r^2/r_0^2\right)$.

- To keep an analytically tractable model, Gyro-viscosity is neglected, $\nabla \cdot \pi_i = 0,\ \nabla \cdot \pi_e = 0$.

- Electron inertia is neglected as a consequence of the small mass of electrons as compared to ions, $m_e/m_i \ll 1$.

- Like particle collisions won't alter the total momentum of the individual fluid within the framework of the two-fluid model. As a result, the outcome depends on how big the coulomb and neutral collisions are in comparison. Neutral collisions dominate Coulomb collisions for the regimes met in MISTRAL [Ann+11], [Pie16] where $\nu_{ei}^C, \nu_{en}/\omega_{ce} \ll 1$.

- Quasineutraliy, $n_i = n_e$.

- Rigid body equilibrium rotation.

Based on the given assumptions, the continuity equation for jth species is,

$$\frac{\partial n_j}{\partial t} + \nabla \cdot (n_j \mathbf{v}_j) = 0 \tag{4.24}$$

The momentum equation for ions and electrons is,

$$n_i m_i \left[\frac{\partial \mathbf{v}_i}{\partial t} + (\mathbf{v}_i \cdot \nabla)\mathbf{v}_i\right] = e n_i \left(-\nabla\phi + \mathbf{v}_i \times \mathbf{B}\right) - T_i \nabla n_i - m_i n_i \nu_{in} \mathbf{v}_i \tag{4.25}$$

$$0 = -e n_e(-\nabla\phi + \mathbf{v}_e \times \mathbf{B}) - \nabla(n_e T_e) \tag{4.26}$$

The system is closed by assuming T_e and T_i constant in time. The fluctuations in T_e have been observed with Langmuir probe measurements on MISTRAL but are neglected here. It should be noted that the gyroviscosity tensor term for ions ($\nabla \cdot \pi_i$) is omitted in the given system of equations. This choice is made to first establish the basis of a model relaxing the LFA in a comparatively simpler context. The impact of this assumption, not supported by experimental characterization will be discussed in Appendix D.

The next step after having the desired set of equations is to solve them to obtain the dispersion relation. The problem of instability can be better understood by dividing it into two parts: the problem of equilibrium and the problem of stability. An equilibrium is a situation when all the forces are in balance and a time-independent solution is possible. For the stability problem, one can linearize the equations of motion for small deviations from an equilibrium state. The next sections offer more details about this.

4.2.2. Linearization

For instability description, we employ the normal mode analysis method [KT73]. This method implies that if the equilibrium under consideration is perturbed, the linearized plasma equations for the time evolution of the perturbation can be solved, subjected to appropriate boundary conditions, assuming a time dependence.

In the procedure of linearization [Che16], the dependent variables are separated into two parts: an “equilibrium" part indicated by a subscript 0 and a “perturbed" part indicated by the superscript ~.

$$n = n_0 + \tilde{n} \tag{4.27}$$
$$\mathbf{v} = \mathbf{v_0} + \tilde{\mathbf{v}} \tag{4.28}$$
$$\phi = \phi_0 + \tilde{\phi} \tag{4.29}$$

The equilibrium part contains the information about the stationary state of plasma or in other words, it is the state of the plasma without any oscillations such that,

$$\frac{\partial n_0}{\partial t} = \frac{\partial \mathbf{v_0}}{\partial t} = \frac{\partial \phi_0}{\partial t} = 0 \tag{4.30}$$

The perturbed part contains information about the fluctuating quantities. Choosing a Fourier representation for the azimuthal direction, they are given by,

$$\tilde{n} = n_1(r)\ exp\ [i(m\theta - \omega t)] \tag{4.31}$$
$$\tilde{\mathbf{v}} = \mathbf{v}_1(r)\ exp\ [i(m\theta - \omega t)] \tag{4.32}$$
$$\tilde{\phi} = \phi_1(r)\ exp\ [i(m\theta - \omega t)] \tag{4.33}$$
$$\tag{4.34}$$

where $n_1(r)$, $\mathbf{v}_1(r)$ and $\phi_1(r)$ give the perturbation amplitude of density (n), velocity and potential (ϕ) in the radial direction, m is the azimuthal mode number, and $\mathbf{v}_1(r) = v_{r_1}\hat{e}_r + v_{\theta_1}\hat{e}_\theta$. The azimuthal mode number m is an integer and it corresponds to the azimuthal wavevector $k_\theta = m/r = 2\pi r/\lambda$. When representing a wave in the plasma column, m corresponds to the number of minima and maxima on the circumference of the plasma column.

The linear stability is investigated by assuming that the amplitude of the oscillations is small as compared to the equilibrium quantities ($\tilde{n} << n_0, |\tilde{\mathbf{v}}| << |\mathbf{v}_0|$ and $\tilde{\phi} << \phi_0$). The equations are then divided into two parts. The zeroth order part gives the equilibrium. The first order part gives the linear stability. The solutions are the fluctuations which are the eigenfunctions of the system, having frequencies ω as eigenvalues. After reformulating and simplifying the equations, we arrive at an equation giving ω. This equation is called the dispersion relation, which links the pulsation ω and the wave number k of the oscillations. The last step consists in separating the real part and the imaginary part of ω. Here, $\omega = \omega_r + i\gamma$ where ω_r is the real part of the perturbed

frequency and γ is the imaginary part giving growth rate. If $\gamma = 0$, the plasma is stable and all the perturbation variables oscillate harmonically. If $\gamma > 0$, the system is unstable and these normal modes will grow in time.

The study of the linear regime gives information about the onset of instability and the parametric dependencies of the growth rate and mode frequency. If unstable modes are present, they grow exponentially and after some time, the assumption, $\tilde{n} << n_0$ is violated. Perturbations become comparable to the equilibrium and start to interact with each other: this is the non-linear regime. The study of non-linear regime is out of the scope of this thesis.

4.2.3. Equilibrium flow

To study the ion and electron equilibrium flow, the equilibrium velocity $\mathbf{v}_{j0}$ is written as,

$$\mathbf{v_{j0}} = v_{jr_0}\hat{e}_r + v_{j\theta_0}\hat{e}_\theta \tag{4.35}$$

where v_{jr_0} is the radial component and $v_{j\theta_0}$ is the azimuthal component of velocity. The equilibrium flow is derived assuming rigid body rotation such that $v_{j\theta_0} = r\omega_{j0}$ with $\omega'_{j0} = \omega''_{j0} = 0$ where $'$ represents $\partial/\partial r$ and $''$ represents $\partial^2/\partial r^2$.

The equilibrium density (n_0) and plasma potential (ϕ_0) are assumed to have Gaussian and parabolic profiles, respectively. This is compatible with typical profiles measured in MISTRAL (see Section 2.6.2, 2.6.1),

$$n_0(r) = n_{00}\ exp\left(-\frac{r^2}{r_0^2}\right);\ \ \phi_0 = p_1 r^2 + p_2 \tag{4.36}$$

where n_{00}, p_1 and p_2 are constants. Reminding that, here r is the radial coordinate and r_0 is the width of the Gaussian used to parametrize the density profile These equilibrium profiles are consistent with the rigid body rotation assumption used for the equilibrium.

4.2.3.1. Ion equilibrium flow

The ion inertial term $\mathbf{v_{i0}} \cdot \nabla \mathbf{v_{i0}}$ entering Eq. (4.25) becomes,

$$(\mathbf{v}_{i0} \cdot \nabla)\,\mathbf{v}_{i0} = \left(v_{ir_0}\frac{\partial v_{ir_0}}{\partial r} - r\omega_0^2\right)\hat{e}_r + 2\omega_0 v_{ir_0}\hat{e}_\theta \tag{4.37}$$

Substituting Eqs. (4.35) and (4.37) in the ion momentum equation, assuming $\partial \mathbf{v}_{i0}/\partial t = 0$, taking the cross product with $\mathbf{B}$ and then projecting along $\hat{e}_r$, one gets,

$$v_{ir_0} = \frac{-\nu_{in} r\omega_0}{\omega_{ci} + 2\omega_0} \tag{4.38}$$

Variable	Notation	Definition
Normalized frequencies	$\bar{\omega}, \bar{\omega}_0$	$\omega/\omega_{ci}, \omega_0/\omega_{ci}$
Normalized lengths	$\bar{r}, 1/\bar{L}_n$	$r/\rho_i, \rho_i/L_n$
Normalized perturbed density	$\bar{n}_1$	n_1/n_0
Normalized perturbed potential	$\bar{\phi}_1$	$e\phi_1/T_{e0_{ref}}$
Normalized velocities	$\bar{v}_{i,e}$	$v_{i,e}/v_{thi}$
Temperature ratio	τ	$T_{e0_{ref}}/T_i$

Table 4.3.: Normalized parameters and their definitions. Here $T_{e0_{ref}}$ is the reference value of the electron temperature, taken to be the electron temperature on the axis.

The equation above is normalized by dividing v_{ir_0} with $v_{th_i} = \sqrt{T_i/m_i}$; r with $\rho_i = m v_{th_i}/eB$; ν_{in}, ω_0 with $\omega_{ci} = eB/m_i$ and the normalized quantities are noted with an overbar, see Table 4.3,

$$\bar{v}_{ir_0} = \frac{-\bar{\nu}_{in}\bar{r}\bar{\omega}_0}{1+2\bar{\omega}_0} \tag{4.39}$$

which is the equilibrium flow of ions in the radial direction. The only mechanism which can impart a radial component to the equilibrium velocity is collisions.

Using Eq. (4.38) in Eq. (4.25) and projecting along $\hat{e}_\theta$, the equation for azimuthal flow frequency $\omega_0 = v_{i\theta_0}/r$ is given by:

$$\left(\frac{\nu_{in}\omega_0}{2\omega_0+\omega_{ci}}\right)^2 - \omega_0^2 = -\omega_{ci}\omega_{E0} + \omega_{ci}\omega_0 - \omega_{ci}\omega_{*0} + \left(\frac{\nu_{in}^2\omega_0}{2\omega_0+\omega_{ci}}\right) \tag{4.40}$$

Here ω_{E0} is the $E \times B$ drift frequency,

$$\omega_{E0} = \frac{\mathbf{B}\times\nabla\phi_0}{rB^2}\cdot\hat{e}_\theta = \frac{\phi_0'}{rB} \tag{4.41}$$

and ω_{*0} is the ion diamagnetic drift frequency,

$$\omega_{*0} = \frac{T_i}{en_0B}\frac{\mathbf{B}\times\nabla n_0}{rB}\cdot\hat{e}_\theta = \frac{T_i}{erB}\frac{n_0'}{n_0} \tag{4.42}$$

$$= -\frac{T_i}{erB}\frac{1}{L_n} \tag{4.43}$$

where $1/L_n = -n_0'/n_0 = 2r/r_0^2$ is the logarithmic density gradient. It should be noted that ω_{E0} and ω_{*0} are independent of r due to the choice of n_0 and ϕ_0 given by Eq. (4.36).

The rotation direction for positive $\mathbf{E}\times\mathbf{B}$ and diamagnetic frequency is illustrated in Fig. 4.8. Azimuthal flows are counted positive in the direction of increasing θ.

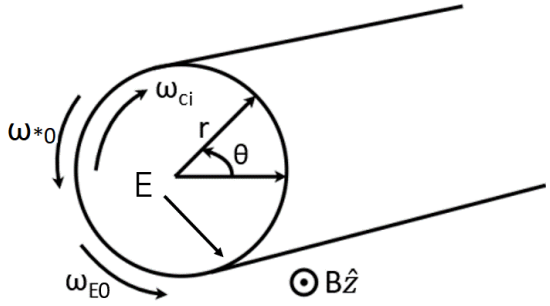

Figure 4.8.: Cylindrical coordinate system and direction of rotation for ion cyclotron frequency ω_{ci}, positive **E**×**B** frequency ($\omega_{E0} > 0$) and positive diamagnetic frequency ($\omega_{*0} > 0$).

Rearranging the terms and then normalizing, Eq. (4.40) is,

$$\boxed{4\left(\bar{\omega}_0 + \frac{1}{2}\right)^4 - \left(1 - \bar{\nu}_{in}^2 + 4(\bar{\omega}_{E0} + \bar{\omega}_{*0})\right)\left(\bar{\omega}_0 + \frac{1}{2}\right)^2 - \frac{\bar{\nu}_{in}^2}{4} = 0} \tag{4.44}$$

which is a fourth order polynomial in $\bar{\omega}_0$ whose solutions are given by,

$$\bar{\omega}_0 = \pm\frac{1}{2}\sqrt{\frac{1}{2}\left[b + \sqrt{b^2 + 4\bar{\nu}_{in}^2}\right]} - \frac{1}{2} \tag{4.45}$$

where $b = 1 + 4(\bar{\omega}_{*0} + \bar{\omega}_{E0}) - \bar{\nu}_{in}^2$. Eq. (4.44) has four roots. Only two roots will be considered since the other two are imaginary and the equilibrium flow is undefined. Eq. (4.45) gives the remaining two roots. The branch for which $\bar{\omega}_0$ increases with increasing $\bar{\omega}_{E0} + \bar{\omega}_{*0}$ is the slow rotation mode and the one that decreases with increasing $\bar{\omega}_{E0} + \bar{\omega}_{*0}$ is the fast rotation mode [Rax+15].

The normalized equilibrium flow $\bar{\omega}_0$ is shown in Fig. 4.9 as a function of the sum of the normalized **E**×**B** and diamagnetic flows, $\bar{\omega}_{E0} + \bar{\omega}_{*0}$, for different values of $\bar{\nu}_{in}$.

For zero collisionality i.e. $\bar{\nu}_{in} = 0$, Eq. (4.44) reduces to,

$$\bar{\omega}_0^2 + \bar{\omega}_0 - (\bar{\omega}_{E0} + \bar{\omega}_{*0}) = 0 \tag{4.46}$$

and the equilibrium flow $\bar{\omega}_0$ is given by [Che66], [Jas72], [GRF17],

$$\bar{\omega}_0 = \frac{-1 \pm \sqrt{1 + 4(\bar{\omega}_{E0} + \bar{\omega}_{*0})}}{2} \tag{4.47}$$

Eq. (4.47) shows that for the equilibrium to exist at $\bar{\nu}_{in} = 0$, the following condition should be satisfied,

$$\bar{\omega}_{E0} + \bar{\omega}_{*0} > -\frac{1}{4} \tag{4.48}$$

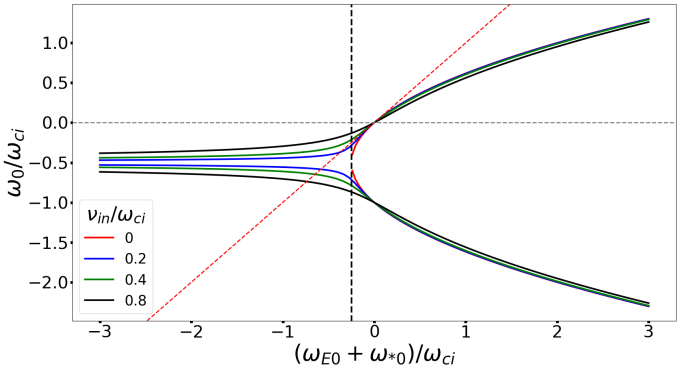

Figure 4.9.: Normalized equilibrium flow frequency (ω_0/ω_{ci}) as a function of normalized $\mathbf{E}\times\mathbf{B}$ drift frequency (ω_{E0}/ω_{ci}) and ion diamagnetic drift frequency (ω_{*0}/ω_{ci}) for different values of normalized ion-neutral collision frequency ($\nu_{in}/\omega_{ci} = 0, 0.2, 0.4$ and 0.8). The black dashed line presents the stability limit for $\bar{\nu}_{in} = 0$. The red dashed line is the diagonal and represents the case when $\bar{\omega}_0 = \bar{\omega}_{E0} + \bar{\omega}_{*0}$.

For finite collisionality, $\bar{\omega}_{E0} + \bar{\omega}_{*0} > -1/4$ is no longer required for the equilibrium to exist. From Fig. 4.9, it is seen that collisions increase the angular frequency of the fast rotation mode and decrease the angular frequency of the slow rotation mode. A more detailed discussion of collisional and non-collisional equilibrium flow can be found in [Rax+15].

If inertial effects are neglected, one obtains,

$$\bar{\omega}_0 = \frac{\bar{\omega}_{E0} + \bar{\omega}_{*0}}{1 + \bar{\nu}_{in}^2} \tag{4.49}$$

If both inertial effects and ion-neutral collisions are ignored, the equilibrium flow is simply, $\bar{\omega}_0 = \bar{\omega}_{E0} + \bar{\omega}_{*0}$. The red dashed line in Fig. 4.9 represents this case with $\bar{\nu}_{in} = 0$ and no inertial effects.

4.2.3.2. Electron equilibrium flow

Writing the equilibrium flow velocity for electrons $\mathbf{v}_{e0}$ as given by Eq. (4.35) and then solving the Eq. (4.26) in the same way as for equilibrium flow of ions, the radial component of the equilibrium flow velocity of electrons is,

$$\bar{v}_{er_0} = 0 \tag{4.50}$$

The absence of electron-neutral collisions ($\bar{\nu}_{en} \approx 0$) is the cause of the zero component of the electron's radial velocity. The azimuthal component for the equilibrium flow velocity of electrons is,

$$\bar{v}_{e\theta_0} = \bar{r}\bar{\omega}_{0e} \quad \text{with} \quad \bar{\omega}_{0e} = \bar{\omega}_{E0} + \bar{\omega}_{*e} \tag{4.51}$$

where $\bar{\omega}_{0e}$ is the electron equilibrium flow frequency and $\bar{\omega}_{*e}$ is the electron diamagnetic drift frequency ω_{*e} normalized to the ion cyclotron frequency, with

$$\omega_{*e} = -\frac{1}{en_0B}\frac{\mathbf{B}\times\nabla(n_0T_{e0})}{rB}\cdot\hat{e}_\theta \tag{4.52}$$

As given by Eq. 4.44, in order to determine the equilibrium flow frequency (ω_0), it is necessary to know the values of ω_{E0}, ω_{*0} and ν_{in}. The range of ν_{in} that is relevant for the MISTRAL plasma column has already been given in Section 4.1.2. The next section determines the range of ω_{E0}, ω_{*0} and thus ω_0 for the MISTRAL plasma column.

4.3. Frequency range in MISTRAL determined by parameterization of experimental profiles

To estimate the range of $\mathbf{E}\times\mathbf{B}$ drift frequency (ω_{E0}) and ion diamagnetic drift frequency (ω_{*0}), the parameters p_1 and r_0 obtained by the parameterization of density and potential profiles in Chapter 2 are used. They are then used in the following equations to find the desired range of frequencies,

$$\omega_{E0} = \frac{2p_1}{B};\quad \omega_{*0} = -\frac{2T_i}{eBr_0^2} \tag{4.53}$$

4.3.1. At different magnetic field intensities

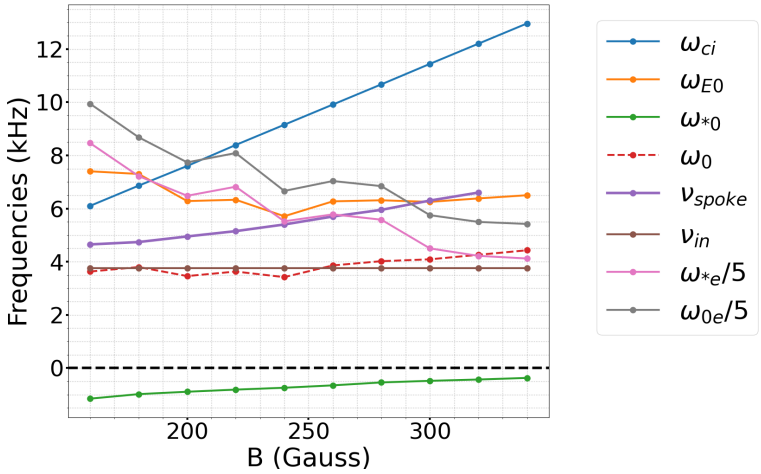

Figure 4.10.: Variation of ion-cyclotron frequency (ω_{ci}), $\mathbf{E}\times\mathbf{B}$ drift frequency (ω_{E0}), ion diamagnetic drift frequency (ω_{*0}), equilibrium flow frequency (ω_0), spoke frequency (ν_{spoke}), ion-neutral collision frequency (ν_{in}), electron diamagnetic drift frequency (ω_{*e}) and electron equilibrium flow frequency (ω_{0e}) for various magnetic field intensities.

Fig. 4.10 shows how various frequencies vary with the increase in magnetic field strength for ref. case A (Sec. 2.6.1). As expected, the ion-cyclotron frequency (ω_{ci})

is increasing linearly with the increase in magnetic field. The ion diamagnetic drift frequency (ω_{*0}) is increasing and the **E**×**B** drift frequency (ω_{E0}) is decreasing with the increase in the magnetic field intensity. The equilibrium flow frequency (ω_0) closely follows the **E**×**B** drift frequency but with a lower value due to inertial effects and ion-neutral friction. The spoke frequency (ν_{spoke}), was determined for various magnetic field intensities in Chapter 2. The electron diamagnetic drift frequency (ω_{*e}) stemming from the temperature and density gradients is substantial, and it significantly contributes to the electron equilibrium flow frequency (ω_{0e}). Both ω_{*e} and ω_{0e} show a decrease with the increase in magnetic field strength.

4.3.2. At different pressure values

The variation of characteristic frequencies in the pressure scan performed for the ref. case B (Sec. 2.6.2) is shown in Fig. 4.11. As the ion-cyclotron frequency (ω_{ci}) is independent of pressure for a given magnetic field, therefore, its value at B=160 G is, $\omega_{ci} \approx 6.1$ kHz. The ion diamagnetic drift frequency (ω_{*0}) does not vary much over the given pressure range. The **E** × **B** drift frequency (ω_{E0}) and the ion equilibrium flow frequency (ω_0) decreases with the increase in pressure. As expected, the ion-neutral collision frequency (ν_{in}) increases linearly with the increase in pressure. The equilibrium flow frequency ω_0 is comparable to ω_{ci} especially at lower values of pressure. The electron diamagnetic drift frequency (ω_{*e}) and electron equilibrium flow frequency (ω_{0e}) are decreasing with the increase in pressure.

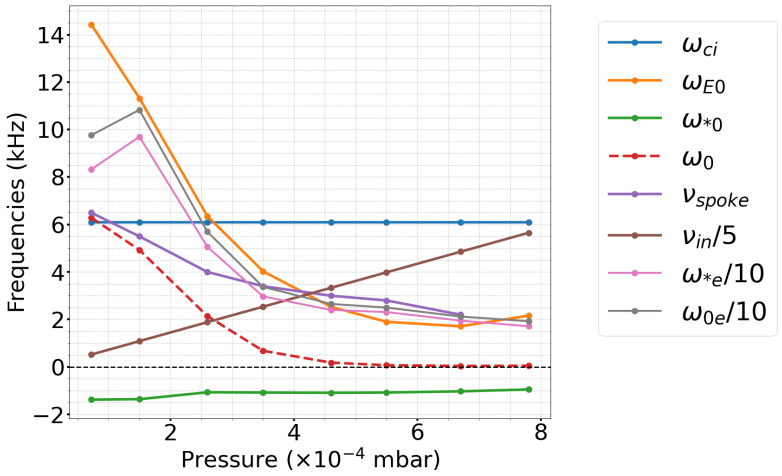

Figure 4.11.: Variation of ion-cyclotron frequency (ω_{ci}), **E** × **B** drift frequency (ω_{E0}), ion diamagnetic drift frequency (ω_{*0}), equilibrium flow frequency (ω_0), spoke frequency (ν_{spoke}), ion-neutral collision frequency (ν_{in}), electron diamagnetic drift frequency (ω_{*e}) and electron equilibrium flow frequency (ω_{0e}) for various values of Pressure at B=160 G.

Although in the configurations shown above, ω_{*0} has a far smaller impact on the equilibrium flow than ω_{E0}, there can exist some configurations where diamagnetic

drift can have a significant influence on the equilibrium flow frequency depending on the width of the density profile.

4.4. LFA not applicable for MISTRAL like plasmas

Fig. 4.10 and Fig. 4.11 clearly indicate that the LFA according to which $\omega_0 << \omega_{ci}$ and $\nu_{spoke} << \omega_{ci}$ is not valid for the plasma system into consideration. Therefore, it is imperative to consider higher-order terms that were neglected in previous models to fully comprehend the linear stability of weakly magnetized plasma columns.

4.5. Summary

In this chapter, the basis of the fluid model has been laid based on the properties of MISTRAL plasma. The range of various parameters relevant to MISTRAL plasma is given. The ordering of different time scales and length scales involved in plasma dynamics forms the basis of appropriate modeling and assumptions to be used in the fluid model. It is shown that the plasma under investigation is quasineutral. The electrons can be considered strongly magnetized whereas ions are weakly magnetized. The validity of various assumptions such as quasi-neutrality, high ion-neutral collisionality, strongly magnetized electrons, weakly magnetized ions, and low plasma beta support the application of the hypotheses used to model the plasmas of interest.

Then the equilibrium flow for ions and electrons has been derived. Unlike for electrons, where the equilibrium flow only occurs in the azimuthal direction; for ions, it occurs both in the radial and azimuthal directions due to the inclusion of finite collisionality. Inertial effect in addition to $\mathbf{E} \times \mathbf{B}$ flow, diamagnetic flow, and ion-neutral collisions modify the equilibrium flow for ions. The electron equilibrium flow is simply the $\mathbf{E} \times \mathbf{B}$ flow and diamagnetic flow. The range of various frequencies which are important factors in determining the equilibrium flow and solution of dispersion relation (see Chapter 5) are provided. It has also been confirmed that the LFA is questionable for the MISTRAL plasma column and should be relaxed.

After discussing the equilibrium flow, the next step in the instability description is to derive the dispersion relation which will be the subject of the next chapter.

5. Linear stability (collisionless case)

The radially global dispersion relation without collisions is derived in this Chapter [Agg+23]. It is then compared to the dispersion relations obtained in the local limit and in the limit of LFA.

To proceed with the derivation of the dispersion relation, we first linearize the momentum equations, Eq. (4.25) and Eq. (4.26), to express the ion and electron flow in the continuity equation. The system of equations is then closed by using the quasi-neutrality approximation, and we are left with a linear differential equation.

5.1. Linear electron response

From the electron momentum equation, Eq. (4.26), the electron flow is written in the customary form:

$$\mathbf{v}_e = \frac{\mathbf{b}\times\nabla\phi}{B} + \frac{1}{en_e}\frac{\mathbf{b}\times\nabla(n_eT_e)}{B} \tag{5.1}$$

When $\mathbf{B}$ is homogeneous and straight (linear plasma column), for any function A, we have:

$$\nabla\cdot(\mathbf{b}\times\nabla A) = 0 \tag{5.2}$$

Therefore, on multiplying Eq. (5.1) with n_e and taking the divergence on both sides,

$$\nabla\cdot(n_e\mathbf{v}_e) = \nabla\cdot\left(n_e\frac{\mathbf{b}\times\nabla\phi}{B}\right) + \frac{1}{eB}\nabla\cdot(\mathbf{b}\times\nabla(n_eT_e)) \tag{5.3}$$

Using the fact that $\nabla\cdot(\mathbf{b}\times\nabla\phi) = 0$ and $\nabla\cdot(\mathbf{b}\times\nabla(n_eT_e)) = 0$, above equation further reduces to,

$$\nabla\cdot(n_e\mathbf{v}_e) = \frac{\mathbf{b}\times\nabla\phi}{B}\cdot\nabla n_e \tag{5.4}$$

The linearized form of the above equation using the Fourier representation of fluctuating quantities given by Eq. 4.34 is,

$$\nabla\cdot(n_e\mathbf{v}_e)|_1 = \frac{im}{rB}\left[-\phi_1 n_0' + \phi_0' n_1\right] \tag{5.5}$$

$$= -im\frac{\phi_1}{rB}n_0' + im\omega_{E0}n_1 \tag{5.6}$$

Combining Eq. (5.6) and the electron continuity equation Eq. (4.24), one obtains the relationship between perturbed density (n_1) and perturbed potential (ϕ_1),

$$\frac{n_1}{n_0} = \frac{m}{rL_n}\frac{1}{\omega - m\omega_{E0}}\frac{\phi_1}{B} \tag{5.7}$$

Normalizing length to ion Larmor radius (ρ_i) and frequencies to the ion cyclotron frequency (ω_{ci}), the normalized form of the above equation is,

$$\boxed{\bar{n}_1 = \frac{m}{\bar{r}\bar{L}_n}\frac{1}{\bar{\omega} - m\bar{\omega}_{E0}}\tau\bar{\phi}_1} \tag{5.8}$$

where $\tau = T_{e0_{ref}}/T_{io}$ with $T_{e0_{ref}}$, the reference value of the electron temperature. It should be noted that the radial variation of the electron temperature is retained here but since the diamagnetic flux is divergence-free (Eqs. (5.1)-(5.4)), it does not enter the continuity equation. The relation between the perturbed density of electrons and perturbed potential given by Eq. (5.8) is therefore identical to that of [Che66], [Rog73] and [GRF17] where the electron diamagnetic flow was neglected.

5.2. Linear ion response

The linearized ion-momentum equation without ion-neutral collision writes,

$$-i\omega\mathbf{v}_{i1} + (\mathbf{v}_{i0}\cdot\nabla)\mathbf{v}_{i1} + (\mathbf{v}_{i1}\cdot\nabla)\mathbf{v}_{i0} = \frac{e}{m_i}\left[-\nabla\phi + \mathbf{v}_{i1}\times\mathbf{B}\right] - \frac{T_i}{m_i}\nabla\frac{n_1}{n_o} \tag{5.9}$$

For a background rigid body rotation, $\mathbf{v}_{i0} = r\omega_0\hat{e}_\theta$, the inertial terms can be written as:

$$(\mathbf{v}_{i0}\cdot\nabla)\mathbf{v}_{i1} = im\omega_0\mathbf{v}_{i1} - \omega_0\mathbf{v}_{i1}\times\mathbf{b} \tag{5.10}$$

and

$$(\mathbf{v}_{i1}\cdot\nabla)\mathbf{v}_{i0} = v_{ir1}\frac{\partial\mathbf{v}_{i0}}{\partial r} + \frac{v_{i\theta1}}{r}\frac{\partial\mathbf{v}_{i0}}{\partial\theta} = -\omega_0\mathbf{v}_{i1}\times\mathbf{b} \tag{5.11}$$

When included in the linearized ion momentum equation (Eq. (5.9)), it yields:

$$-i(\omega - m\omega_0)\mathbf{v}_{i1} = -\frac{\omega_{ci}}{B}\nabla\phi + (\omega_{ci} + 2\omega_0)\mathbf{v}_{i1}\times\mathbf{b} - \frac{\omega_{ci}T_i}{eB}\nabla\frac{n_1}{n_o} \tag{5.12}$$

The background flow enters in the Doppler shifted frequency, $\omega - m\omega_0$, on the left-hand side and in the linearized Coriolis force, $F_{co} = 2m_i\mathbf{v}_{i1}\times\omega_0\mathbf{b}$, on the right-hand side.
Upon normalization, we get,

$$-i(\bar{\omega} - m\bar{\omega}_0)\bar{\mathbf{v}}_{i1} = (1 + 2\bar{\omega}_0)\bar{\mathbf{v}}_{i1}\times\mathbf{b} - \nabla\Phi_1 \tag{5.13}$$

Writing, $C = 1+2\bar{\omega}_0$, the factor by which the Laplace force is modified due to the inertial force, $\bar{\omega}_{ph} = \bar{\omega} - m\bar{\omega}_0$, the normalized Doppler shifted frequency and combining the perturbed density and potential terms into $\Phi_1 = \bar{n}_1 + \tau\bar{\phi}_1$, the linearized ion momentum equation then writes:

$$-i\bar{\omega}_{ph}\bar{\mathbf{v}}_{i1} = -\nabla\Phi_1 + C\bar{\mathbf{v}}_{i1}\times\mathbf{b} \tag{5.14}$$

Taking first the cross-product of Eq. (5.14) with $\mathbf{b}$ and using again Eq. (5.14) to replace $\mathbf{v}_{i1}\times\mathbf{b}$ in that new equation, we get:

$$\bar{\mathbf{v}}_{i1} = \frac{C}{C^2-\bar{\omega}_{ph}^2}\left[\mathbf{b}\times\nabla\Phi_1 + i\frac{\bar{\omega}_{ph}}{C}\nabla\Phi_1\right] \tag{5.15}$$

The first term in the bracket is the combination of the perturbed $\mathbf{E}\times\mathbf{B}$ and diamagnetic flows. The second one is the polarisation flow. Inertial effects are included in the factor C. The polarisation flow matters when the mode frequency ω is comparable to ω_{ci}, which is precisely the regime of interest here. Note that the polarization flow makes the plasma compressible ($\nabla\cdot\bar{\mathbf{v}}_{i1}\neq 0$).

The final step needed before obtaining the dispersion relation is to compute the linearized divergence of the ion particle flux:

$$\nabla\cdot(n_i\bar{\mathbf{v}}_i)|_1 = n_0\nabla\cdot\bar{\mathbf{v}}_{i1} + \bar{\mathbf{v}}_{i1}\cdot\nabla n_0 + \bar{\mathbf{v}}_{i0}\cdot\nabla n_1 \tag{5.16}$$

These terms are given by:

$$n_0\nabla\cdot\bar{\mathbf{v}}_{i1} = n_0\frac{i\bar{\omega}_{ph}}{C^2-\bar{\omega}_{ph}^2}\nabla^2\Phi_1 \tag{5.17}$$

$$\bar{\mathbf{v}}_{i1}\cdot\nabla n_0 = \frac{C}{C^2-\bar{\omega}_{ph}^2}\left[-\frac{im}{\bar{r}}\Phi_1 n_0' + i\frac{\bar{\omega}_{ph}}{C}\Phi_1' n_0'\right] \tag{5.18}$$

$$\bar{\mathbf{v}}_{i0}\cdot\nabla n_1 = im\bar{\omega}_0 n_1 \tag{5.19}$$

where $\nabla^2\Phi_1 = \Phi_1'' + \Phi_1'/r - m^2/r^2\Phi_1$.

5.3. Dispersion relation

Combining quasi-neutrality, $n_e = n_i$, and the continuity equations yields:

$$\nabla\cdot(n_e\bar{\mathbf{v}}_e)|_1 = \nabla\cdot(n_i\bar{\mathbf{v}}_i)|_1 \tag{5.20}$$

which implies:

$$\frac{m}{\bar{r}}\frac{1}{\bar{L}_n}\tau\bar{\phi}_1 + m\bar{\omega}_{E0}\bar{n}_1 = \frac{C}{C^2-\bar{\omega}_{ph}^2}\left[\frac{m}{\bar{r}}\frac{1}{\bar{L}_n}\Phi_1 - \frac{\bar{\omega}_{ph}}{C}\frac{1}{\bar{L}_n}\Phi_1' + \frac{\bar{\omega}_{ph}}{C}\nabla^2\Phi_1\right] + m\bar{\omega}_0\bar{n}_1 \tag{5.21}$$

Now, using the electron continuity equation, Eq. (5.8), to express $\bar{n}_1$ as a function of $\bar{\phi}_1$ in $\Phi_1 = \bar{n}_1 + \tau\bar{\phi}_1$, we get:

$$\Phi_1 = (1+\alpha_*)\tau\bar{\phi}_1 \tag{5.22}$$

with

$$\alpha_* = -\frac{m\bar{\omega}_{*0}}{\bar{\omega}_{ph} - m\,(\bar{\omega}_{E0} - \bar{\omega}_0)} \tag{5.23}$$

Note that when the ion pressure gradient is neglected in the ion momentum equation ($T_i = 0$), we get $\alpha_* = 0$ and $\Phi_1 = \tau\bar{\phi}_1$.

Using Eq. (5.22) to express $\tau\bar{\phi}_1$ and $\bar{n}_1$ as a function of Φ_1 and reminding that from the equation dictating the equilibrium flow, $\bar{\omega}_0 + \bar{\omega}_0^2 = \bar{\omega}_{*0} + \bar{\omega}_{E0}$, Eq. (5.21) can be written as:

$$\Phi_1'' + \left[\frac{1}{\bar{r}} - \frac{1}{\bar{L}_n}\right]\Phi_1' - \frac{m^2}{\bar{r}^2}\Phi_1 + \frac{1}{\bar{r}\bar{L}_n}N\Phi_1 = 0 \tag{5.24}$$

where

$$N = m\left[\frac{C}{\bar{\omega}_{ph}} - \frac{C^2 - \bar{\omega}_{ph}^2}{\bar{\omega}_{ph} - m\bar{\omega}_0^2}\right] \tag{5.25}$$

Eq. (5.24) and (5.25) provide an extension of the model derived in [Che66] for arbitrary frequency values but in the limit of vanishing gyro-viscosity. The low-frequency expansion involved in [Che66] consists in approximating $C^2 - \bar{\omega}_{ph}^2 \sim C^2$. In this limit,

$$N = m\left[\frac{C}{\bar{\omega}_{ph}} - \frac{C^2}{\bar{\omega}_{ph} - m\bar{\omega}_0^2}\right] \tag{5.26}$$

and one exactly recovers Eq. (25) in [Che66] for $\nabla\cdot\pi_i = 0$. Note that N is radially constant because of the assumption of rigid body rotation. The differential equation (5.24) can be solved by the method used in [RKR62], [Che66] and [Rog73] by exploiting the change of variables,

$$z = r^2/r_0^2 \tag{5.27}$$

where r_0 is the width of the Gaussian used to parametrize the density profile defined by Eq. (2.4), and enters Eq. (5.24) through $1/L_n = 2r/r_0^2$, combined with

$$\Phi_1 = z^{-\frac{1}{2}}e^{\frac{z}{2}}W(z), \tag{5.28}$$

to obtain the Whittaker's equation [WW],

$$\frac{d^2W}{dz^2} + \left\{-\frac{1}{4} + \frac{N+1}{2z} + \frac{1-m^2}{4z^2}\right\}W = 0 \tag{5.29}$$

The non-singular solution of this equation is given by,

$$W_{N,m}(z) = z^{\frac{m+1}{2}}e^{-\frac{z}{2}}F\left(\frac{m-N}{2}, 1+2m, z\right) \tag{5.30}$$

where $F\left(\frac{m-N}{2}, 1+2m, z\right)$ is the confluent hyper-geometric function of the first kind known as Kummer's function. Imposing the boundary condition $\Phi(Z) = 0$, with $Z = r_b^2/r_0^2$ (where r_b is the outer radial boundary of the cylindrical vessel), fully determines the possible values of N, which for different mode numbers m are evaluated from the zeros of the Kummer function $F\left(\frac{m-N}{2}, 1+2m, Z\right)$. These zeros can be evaluated numerically. Alternatively, the asymptotic values of N ($Z \to \infty$) are $N = m+2n$ where $n = 0, 1, 2, 3, ...$ is the radial mode number [RKR62], [Che66]. The radial mode number n simply indicates which zero of F we are referring to; e.g. $n = 0$ implies the first value of N at which the function F goes to zero, $n = 1$ implies the second value of N at which the function F goes to zero and so on.

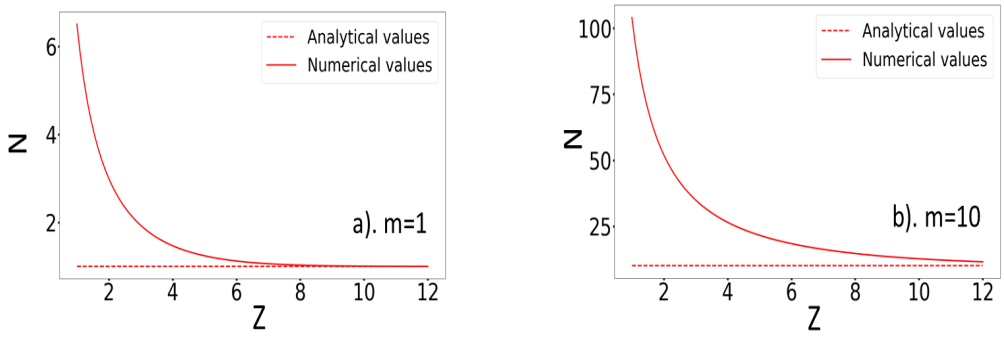

Figure 5.1.: Values of N corresponding to the first zero of Kummer's function for different values of $Z = r_b^2/r_0^2$. The solid line denotes the values evaluated numerically and the dashed line (−−) denotes the asymptotic values.

In Fig. 5.1, the numerical solutions for N, obtained using `whitm` function in the Python library `mpmath`, are compared to the asymptotic solutions for $n = 0$. Convergence is reached at $Z > 6$ for $m = 1$, but higher Z values are required at high m numbers. For practical applications like in MISTRAL where $r_b = 10$ cm and $r_0 \approx 3-6$ cm ($Z \approx 10.8-2.8$), it is, therefore, preferable to use the numerical solution. In the following discussion, we will only use the values of N evaluated numerically.

Note that for a given radial mode number n, the value of N and the eigenfunction shape only depends on the azimuthal mode number m and the value of Z, which represents the ratio of the cylinder radius to the plasma radius. The eigenfunctions are therefore independent of the background flow $\bar{\omega}_0$. Eigenfunctions obtained for $m = 1, 2, 5$ and 10 for different Z values and $n = 0$, are shown in Fig. 5.2. For $Z = 2.8$, the modes are more concentrated towards the center as compared to what we observe for $Z = 10.8$. The solutions of Eq. (5.28) are purely real, therefore, there is no radial variation of the phase of the eigenfunctions.

However, if the radial mode number n is changed, the eigenfunction changes shape for a fixed azimuthal mode number m and the value of Z. This situation has been

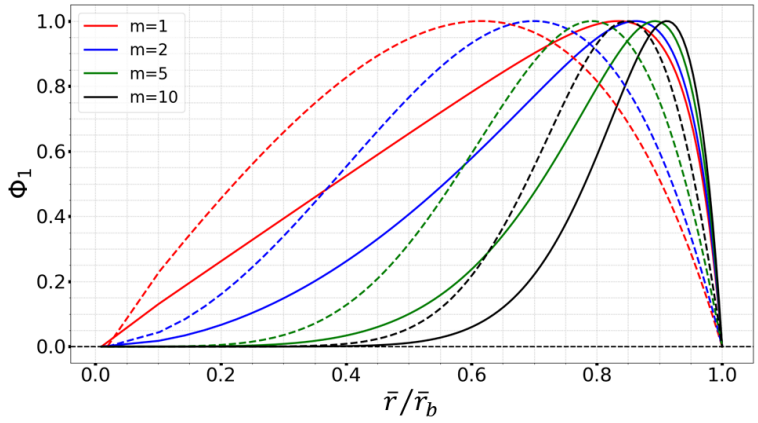

Figure 5.2.: Eigenfunction Φ as a function of $\bar{r}/\bar{r}_b$ for $m = 1, 2, 5$ and 10. The solid lines represent the case when $Z = 10.8$ and the dashed lines represent the case when $Z = 2.8$. Only the first radial harmonic $n = 0$ is shown.

shown in Fig. 5.3. The radial mode number n represents the number of radial nodes.

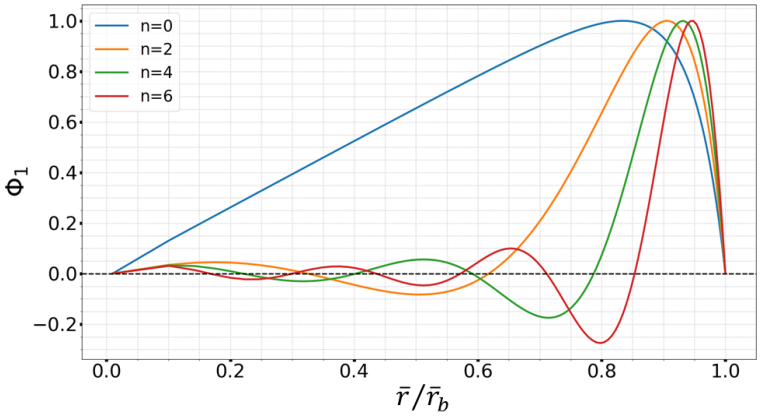

Figure 5.3.: Eigenfunction Φ as a function of $\bar{r}/\bar{r}_b$ for $n = 0, 2, 4$ and 6 corresponding to $m = 1$ and $Z = 10.8$.

Once N is known, rearranging Eq. (5.25) gives the cubic dispersion relation,

$$\bar{\omega}_{ph}^3 - \frac{N}{m}\bar{\omega}_{ph}^2 + \left(N\bar{\omega}_0^2 - 2C\bar{\omega}_0\right)\bar{\omega}_{ph} - mC\bar{\omega}_0^2 = 0 \tag{5.31}$$

from which the mode growth rate and frequency can be computed.

5.4. Specific limits of the dispersion relation

5.4.1. For $\bar{\omega}_0 = -0.5$ i.e. C=0

If $\bar{\omega}_0 = -0.5$ then $C = 0$ i.e. the Coriolis force factor is zero, in Eq. 5.31 which reduces to:

$$\bar{\omega}_{ph}^2 - \frac{N}{m}\bar{\omega}_{ph} + N\bar{\omega}_0^2 = 0 \tag{5.32}$$

The roots of the above equation are given by,

$$\bar{\omega}_{ph} = \frac{N}{2m} \pm \frac{1}{2}\sqrt{\frac{N^2}{m^2} - 4N\bar{\omega}_0^2} \tag{5.33}$$

As $\bar{\omega}_0 = -0.5$, the instability condition is given as:

$$N < m^2 \tag{5.34}$$

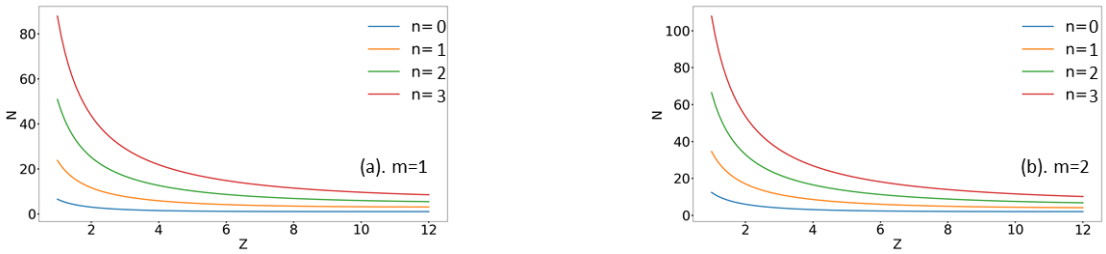

Figure 5.4.: Values of N corresponding to $n = 0, 1, 2, 3$ for different values of $Z = \bar{r}_b^2/\bar{r}_0^2$ for (a). $m = 1$ and (b). $m = 2$.

The value of N for a given m depends on the radial mode number n and radial boundary Z. It is shown in Fig. 5.4 by solving Eq. 5.29 numerically for various values of Z. For $m = 1$, the condition given by Eq. 5.4 is not satisfied for the given range of Z and n. For $m = 2$ and $n = 0$, the instability condition is satisfied when $Z > 3$ and does not hold for other values of n. On a similar basis, the instability condition can be checked for higher azimuthal mode numbers.

5.4.2. For $\bar{\omega}_0 = 0$ i.e. C=1

If $\bar{\omega} = 0$ i.e. $C = 1$, then the dispersion relation given by Eq. 5.31 reduces to,

$$\bar{\omega}_{ph} = \frac{N}{m} \tag{5.35}$$

This implies that for $\bar{\omega}_0 = 0$, no instability exists and the existing modes propagate with a frequency of N/m.

5.4.3. Solution at large values of Z

At large values of Z, N can be approximated as equivalent to m. However, the largeness of Z depends on two quantities, the parameter r_0 and the radial boundary r_b. Even though Z is large, another two parameters that determine if N can be approximated equivalent to m are the radial mode number n and azimuthal mode number m. As can be seen from Fig. 5.1, the value of Z at which N converges to the value of m for the radial mode number $n = 0$ differs for different azimuthal mode numbers. Keeping this point in mind and substituting $N = m$ (given that $n = 0$), Eq. 5.31 becomes,

$$\bar{\omega}_{ph}^3 - \bar{\omega}_{ph}^2 + \left(m\bar{\omega}_0^2 - 2C\bar{\omega}_0\right)\bar{\omega}_{ph} - mC\bar{\omega}_0^2 = 0 \tag{5.36}$$

which on factorization reduces to,

$$\left(\bar{\omega}_{ph} - C\right)\left(\bar{\omega}_{ph}^2 + 2\bar{\omega}_0\bar{\omega}_{ph} + m\bar{\omega}_0^2\right) = 0 \tag{5.37}$$

The equation given above yields the most unstable solution,

$$\bar{\omega}_{ph} = -\bar{\omega}_0 + i\left(\sqrt{m-1}\right)|\bar{\omega}_0| \tag{5.38}$$

This implies that for a fixed mode number m and at large radial boundaries for which $N = m$, the growth rate only depends on $|\bar{\omega}_0|$.

5.5. Low-frequency approximation (LFA) and Local limit

5.5.1. Low-frequency approximation

If the LFA is applied i.e. if $C^2 - \bar{\omega}_{ph}^2 \approx C^2$, Eq. 5.31 becomes,

$$\frac{N}{m}\bar{\omega}_{ph}^2 - \left(N\bar{\omega}_0^2 - 2C\bar{\omega}_0\right)\bar{\omega}_{ph} + mC\bar{\omega}_0^2 = 0 \tag{5.39}$$

which is exactly equivalent to Eq. (30) in [Che66] if the terms with $1/r_0^2$ entering because of the gyro-viscosity tensor are dropped.

5.5.2. Local limit

The local limit assumes small perturbations around a local equilibrium, neglects or approximates spatial variations, and focuses on the behavior within a restricted region. To make the link with previous work, e.g. [Che66] and [GRF17], the local limit

is obtained by assuming $\Phi_1' = 0$, $\Phi_1'' = 0$ in Eq. (5.24),

$$\bar{\omega}_{ph}^3 - \frac{m\bar{r}_0^2}{2\bar{r}^2}\bar{\omega}_{ph}^2 + \left(-2C\bar{\omega}_0 + m^2\bar{\omega}_0^2\frac{\bar{r}_0^2}{2\bar{r}^2}\right)\bar{\omega}_{ph} - mC\bar{\omega}_0^2 = 0 \tag{5.40}$$

This is the same as the dispersion relation obtained by equating Eqs. 17(a) and 17(b) in [GRF17]. Note that in [GRF17], the diamagnetic drift of ions was neglected. It is kept here but only enters the equation by modifying the equilibrium azimuthal flow $\bar{\omega}_0$.

5.5.3. Low-frequency approximation + Local limit

Using the LFA in Eq. (5.40), leads to the following dispersion relation,

$$\bar{\omega}_{ph}^2 + \left(\frac{4\bar{r}^2C\bar{\omega}_0}{m\bar{r}_0^2} - m\bar{\omega}_0^2\right)\bar{\omega}_{ph} + \frac{2\bar{r}^2C\bar{\omega}_0^2}{\bar{r}_0^2} = 0 \tag{5.41}$$

5.6. Linear Stability analysis

5.6.1. Radial mode number n

We first examine the role of the radial mode number n on linear stability.

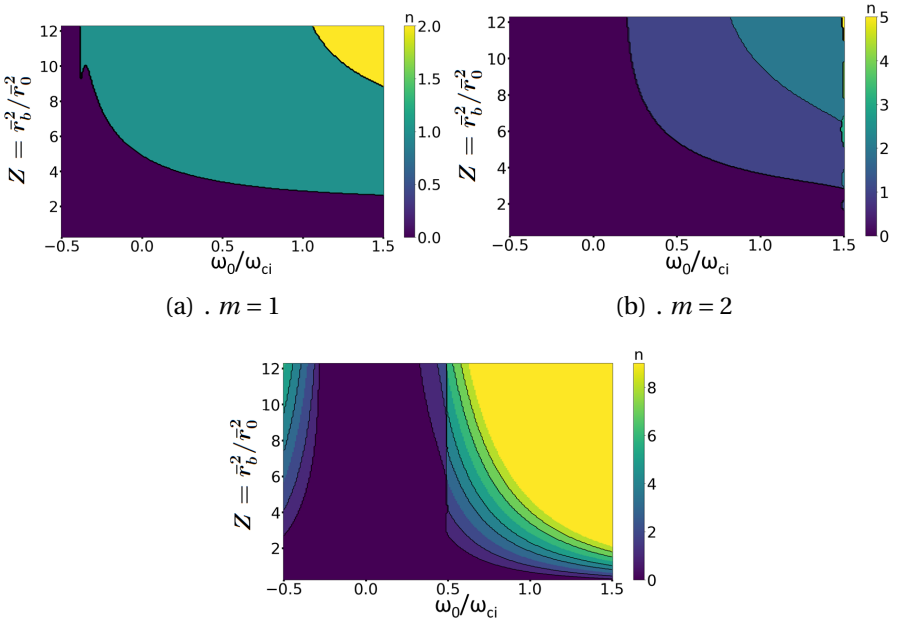

(a) . $m = 1$ (b) . $m = 2$

(c) . $m = 10$

Figure 5.5.: Radial mode number n corresponding to the largest growth rate $\bar{\gamma}$ as a function of $Z = \bar{r}_b^2/\bar{r}_0^2$ and ω_0/ω_{ci}. The color bar represents the radial mode number n.

Fig. 5.5 represents the radial mode number n which yields the largest growth rate evaluated using the global dispersion relation (Eq. 5.31) for a given mode number m as a function of Z and ω_0/ω_{ci}. For $m = 1,2$ and for the given range of ω_0/ω_{ci}, the radial mode number $n = 0$ has the largest growth rate for $Z < 3$. For $Z > 3$, higher radial mode numbers are progressively dominating as $\bar{\omega}_0$ and Z increases. For $m = 10$, the lowest radial mode number $n = 0$ corresponds to the largest growth rate when $-0.3 \leq \omega_0/\omega_{ci} \leq 0.3$. For large values of $|\bar{\omega}_0|$, the radial mode number n that gives the largest growth rate also increases with $|\bar{\omega}_0|$ and Z. The situation is more clearly depicted in Fig. 5.6.

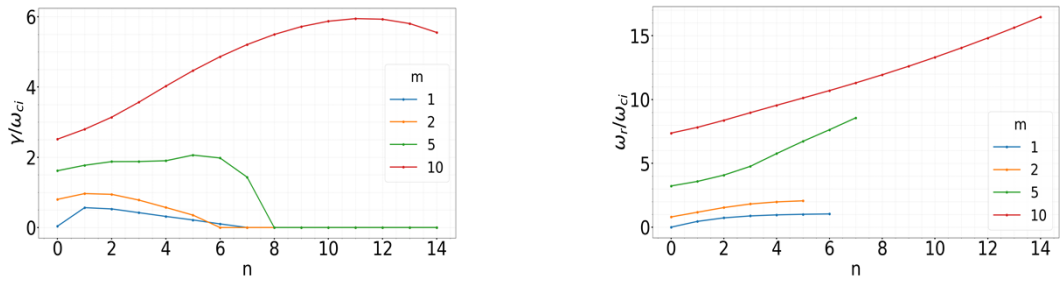

Figure 5.6.: Normalized growth rate (left) and normalized perturbed frequency (right) as a function of radial mode number n for different azimuthal mode numbers m. Here $Z \approx 10.8$ and $\bar{\omega}_0 = 0.8$.

Fig. 5.6 shows how the normalized growth rate and perturbed frequency vary with the increase in radial mode number for a fixed m. As m is increasing, the radial mode number that corresponds to the largest growth rate is also increasing. It should be noted that this increase in radial mode number for a given m is sensitive to the values of $\bar{\omega}_0$ and Z. Importantly, when the growth rate is evaluated using the global dispersion relation with LFA (Eq. 5.39), it is always the lowest radial mode number $n = 0$ that excites the azimuthal mode with the largest growth rate. In the following discussion, we will focus on the radial mode number $n = 0$. This lets us compare the growth rate corresponding to the same radial mode number n for the dispersion relations with and without LFA.

5.6.2. Effect of LFA

The most unstable mode obtained from the global dispersion relation without (Eq. (5.31)) and with LFA (Eq. (5.39)) for mode number $n = 0$ and $m = 1,2$ and 10 are shown in Fig. 5.7 as a function of ω_0/ω_{ci} and Z.

The two models predict the growth rate to increase with $|\bar{\omega}_0|$, with an asymmetry with respect to $\bar{\omega}_0$, originating from the inertial term in the effective magnetization factor C. The difference between two models increases with increasing m number

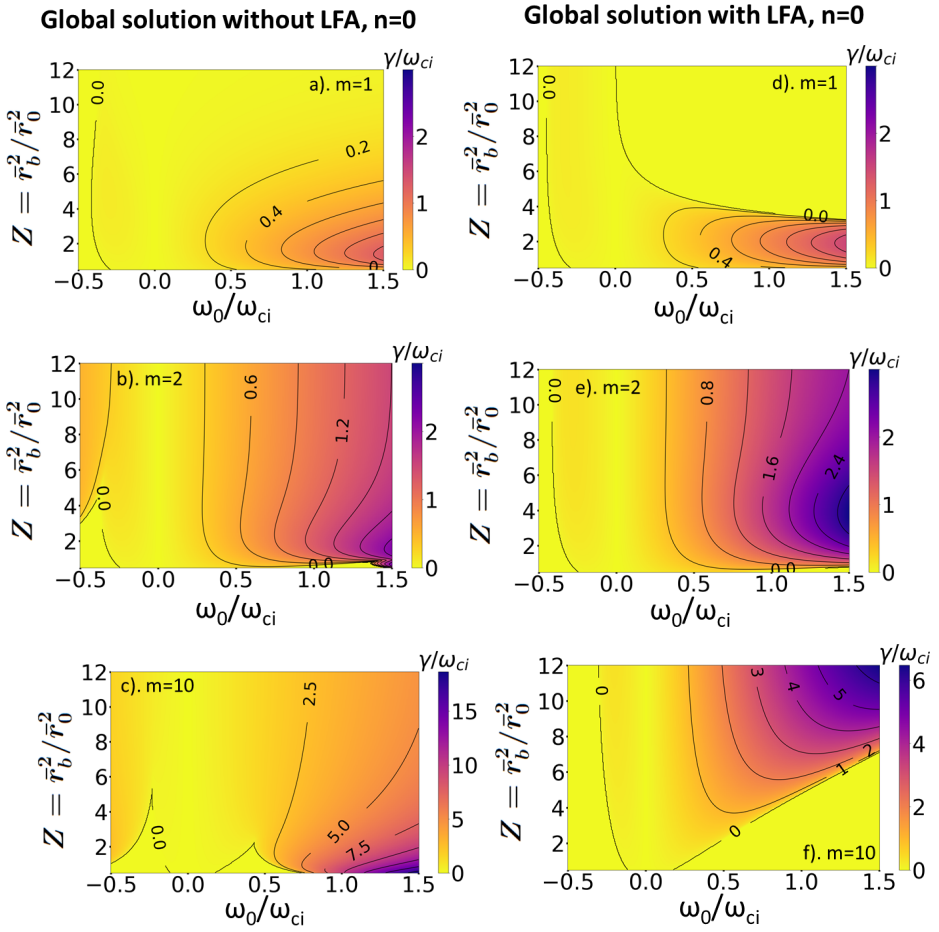

Figure 5.7.: Normalized growth rate γ/ω_{ci} as a function of normalized equilibrium flow frequency (ω_0/ω_{ci}) and $Z = \bar{r}_b^2/\bar{r}_0^2$ where $\bar{r}_b$ is the radial boundary and $\bar{r}_0$ is the width of the Gaussian normalized to Larmor radius ρ_i for the global dispersion relation given by Eq. (5.31) (Figs. (a,b,c)) and Eq. (5.39) (Figs.(d,e,f)). The color bar represents the normalized growth rate ($\bar{\gamma} = \gamma/\omega_{ci}$).

and equilibrium flow frequency $\bar{\omega}_0$. For $m = 10$, the region of higher growth rate, as well as the stability region are radically different with and without LFA. Without the LFA, the largest growth rate is obtained at low Z and large $\bar{\omega}_0$, whereas this becomes a stable region and the growth rate is maximum at large Z with the LFA. The difference in the stability region stems from the neglect of the terms of the order of $\bar{\omega}_{ph}^3$. For frequencies satisfying $\omega - m\omega_0 << \omega_{ci}$, the LFA is valid, and hence the dispersion relation with LFA (Eq. (5.39)) yields correct results, but as we move towards regimes with high-frequency values, the LF ordering fails. There is a common region that is stable ($\bar{\gamma} = 0$) for both the cases and that region corresponds to $\bar{\omega}_0 = 0$.

The validity domain of the LFA as a function of ω_0/ω_{ci} is emphasized in Fig. 5.8, where the solution without the LFA (Eq. (5.31)) with the red curve, is compared to the solution with the LFA valid when $\omega_{ph}/\omega_{ci} = O(\rho^2)$ (green curve, Eq. (5.39)) and to another solution with the LFA but valid at higher frequency i.e. $\omega_{ph}/\omega_{ci} = O(\rho)$ (blue curve, Eq. (38) in [Che66] with $\nabla \cdot \pi_i = 0$).

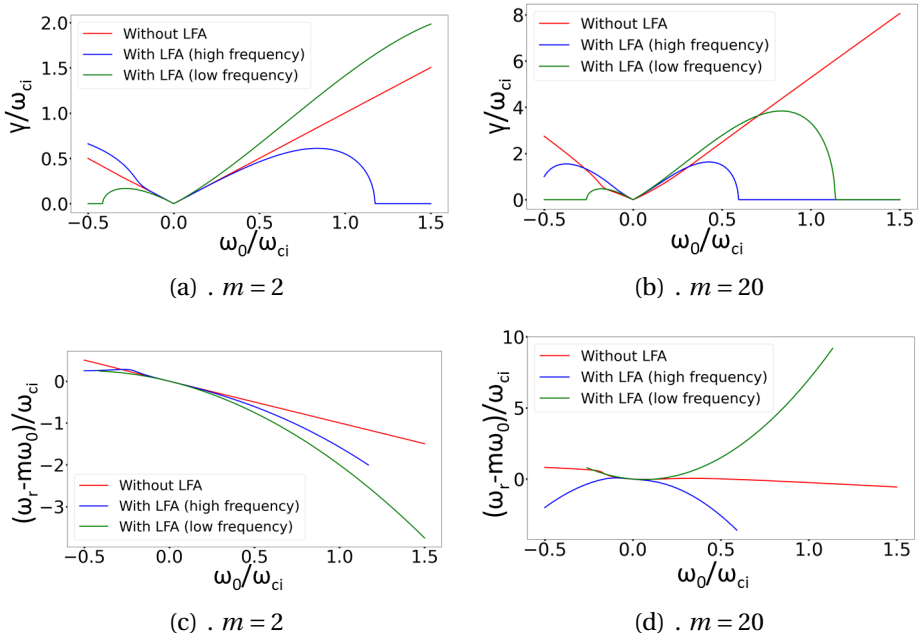

(a) . $m = 2$ (b) . $m = 20$

(c) . $m = 2$ (d) . $m = 20$

Figure 5.8.: Normalized growth rate γ/ω_{ci} and normalized Doppler shifted frequency $(\omega_r - m\omega_0)/\omega_{ci}$ as a function of normalized equilibrium flow frequency (ω_0/ω_{ci}) for (a,c). $m = 2$ and (b,d). $m = 20$ for $Z = 10.78$.

All three dispersion relations, predict the same growth rate $\bar{\gamma}$ and the real part of Doppler shifted frequency $\bar{\omega}_r - m\bar{\omega}_0$ when the values of $\bar{\omega}_0$ are close to zero. As $\bar{\omega}_0$ increases, the model predictions deviate, especially for higher mode numbers. This accounts from the fact that terms involving higher order of $\bar{\omega}_{ph} = \bar{\omega} - m\bar{\omega}_0$ i.e. the Doppler shifted frequency have been neglected in evaluating the dispersion relations in [Che66] and as the factor $m\bar{\omega}_0$ increases, the assumption is no longer valid.

5.6.3. Impact of radial boundary on growth rate

The position of the boundary also has a strong influence on the mode growth rate for a given value of $\bar{\omega}_0$. The growth rate and real part of the Doppler shifted frequency at different radial boundary positions $\bar{r}_b$ keeping $\bar{r}_0$ fixed, for various values of m evaluated by the global dispersion relation (Eq. (5.31)) is shown in Fig. 5.9.

At fixed plasma size, $\bar{r}_0$, increasing the cylinder radius $\bar{r}_b$, for which $\Phi(Z) = 0$ is imposed, first destabilizes all modes and then has limited to no impact on the growth

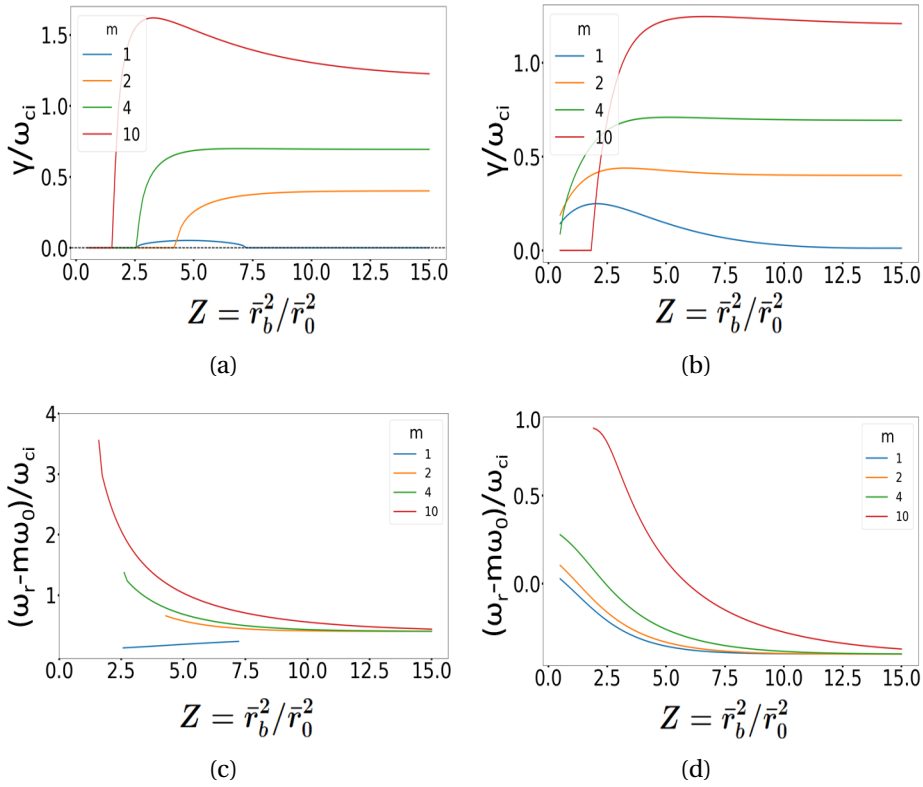

Figure 5.9.: Normalized growth rate $\bar{\gamma} = \gamma/\omega_{ci}$ and normalized Doppler shifted frequency $(\omega_r - m\omega_0)/\omega_{ci}$ as a function of $Z = \bar{r}_b^2/\bar{r}_0^2$ for various mode numbers m using dispersion relation (Eq. (5.31)). Figs (a,c). for $\bar{\omega}_0 = -0.4$ and Figs. (b,d). for $\bar{\omega}_0 = 0.4$

rate once $\bar{r}_b \sim 3\bar{r}_0$ ($Z \sim 9$). Note that $m = 1$ has a different behavior and gets fully stabilized when the bounding cylinder radius is increased.

For the real part of the normalized Doppler shifted frequency $\bar{\omega}_r - m\bar{\omega}_0$, for all the mode numbers, the frequency is maximum for small values of Z and then decreases as Z increases except for $m = 1$ when $\bar{\omega}_0 = -0.4$. The sign of $\bar{\omega}_0$ plays a critical role in determining the sign of Doppler shifted frequency $(\bar{\omega}_r - m\bar{\omega}_0)$.

Irrespective of the mode number, as Z approaches large values, the Doppler shifted frequency $(\bar{\omega}_r - m\bar{\omega}_0)$ tends to converge towards $-\bar{\omega}_0$ (Fig. 5.9 (c),(d)). This convergence indicates that all the modes exhibit a common rotational frequency, possibly allowing mode synchronization in the non-linear phase.

The growth rate saturates to the same level at large values of Z regardless of the direction of the equilibrium flow frequency, as depicted in Fig. 5.10 except for $m = 1$. When the equilibrium flow frequency is doubled, the saturated growth rate also gets doubled compared to its previous value. The reason being, the scaling of growth rate as $\sqrt{m-1}|\bar{\omega}_0|$ with $|\bar{\omega}_0|$ for fixed mode number m as given by Eq. 5.38. It is

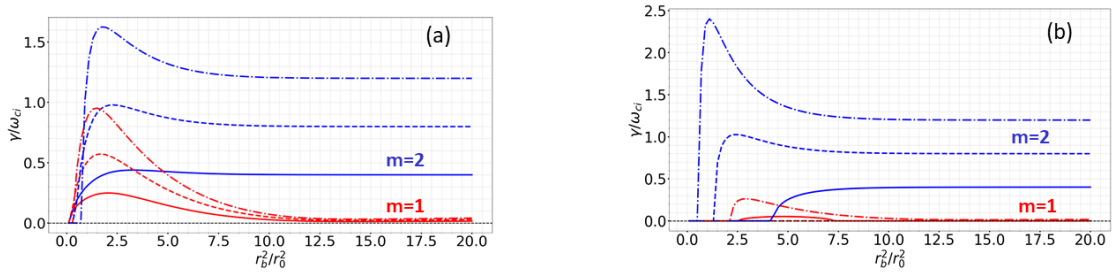

Figure 5.10.: Normalized growth rate $\bar{\gamma} = \gamma/\omega_{ci}$ as a function of $Z = \bar{r}_b^2/\bar{r}_0^2$ for mode numbers $m = 1,2$ using dispersion relation (Eq. (5.31)). Fig (a). represents the case when $\bar{\omega}_0 = 0.4$ (solid line), $\bar{\omega}_0 = 0.8$ (dashed line) and $\bar{\omega}_0 = 1.2$ (dashdot line). Fig (b). represents the case when $\bar{\omega}_0 = -0.4$ (solid line), $\bar{\omega}_0 = -0.8$ (dashed line) and $\bar{\omega}_0 = -1.2$ (dashdot line). The mode $m = 1$ is presented by red and mode $m = 2$ is presented by blue.

important to note that the solution plotted in Fig. 5.9 and Fig. 5.10 is evaluated using Eq. 5.24. However, for large values of Z, the same can be recovered using Eq. 5.38 which specifies the saturation of growth rate and convergence of Doppler shifted frequency at large values of Z.

5.6.4. Eigenfunction, relative fluctuation, and phase difference

5.6.4.1. Eigenfunction

The expression of eigenfunctions for the normalized perturbed density n_1/n_0 and perturbed potential $e\phi_1/T_{e0_{ref}}$ is obtained by using Eqs. (5.8) and (5.22),

$$\bar{n}_1 = \frac{m}{\bar{r}\bar{L}_n(\bar{\omega} - m\bar{\omega}_{E0})}\frac{\Phi_1}{(1+\alpha_*)} \tag{5.42}$$

$$\bar{\phi}_1 = \frac{\Phi_1}{(1+\alpha_*)\tau} \tag{5.43}$$

where α_* is given by Eq. (5.23). Using these expressions, the eigenfunctions $\bar{n}_1$ for $m = 1$ and 10 are shown in Fig. 5.11 for $\tau = 1$. The perturbations in density and potential are more spread out for $m = 1$ than for $m = 10$ or in other words, modes with higher azimuthal mode numbers are more localized towards the boundary region, as already discussed in Fig. 5.2.

5.6.4.2. Amplitude of potential fluctuations relative to density fluctuations

The ratio of potential to density fluctuation amplitudes i.e. $|\bar{\phi}_1/\bar{n}_1|$ is provided in the table 3.1 as a criterion for instability identification. It should be noted that the instability criteria given in table 3.1 is based on the analysis using LFA. Therefore, to check if the criteria is valid even if the analysis is done using the dispersion relation

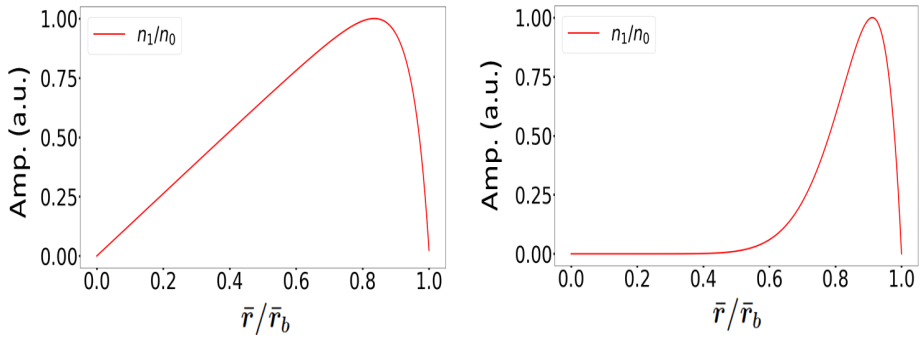

(a) . $m = 1$ (b) . $m = 10$

Figure 5.11.: Normalized perturbed density n_1/n_0 for (a). $m = 1$ and (b). $m = 10$ as a function $\bar{r}/\bar{r}_b$ using $Z = 10.8$. The parameters used to obtain these eigenfunctions are $\bar{\omega}_{E0} = 0.95$, $\bar{\omega}_{*0} = -0.35$, $\bar{\omega}_0 = 0.42$ and $\tau = 1$.

without LFA, we divide Eq. (5.43) by Eq. (5.42),

$$\frac{\bar{\phi}_1}{\bar{n}_1} = (\bar{\omega} - m\bar{\omega}_{E0})\,\frac{\bar{r}\bar{L}_n}{m\tau} \tag{5.44}$$

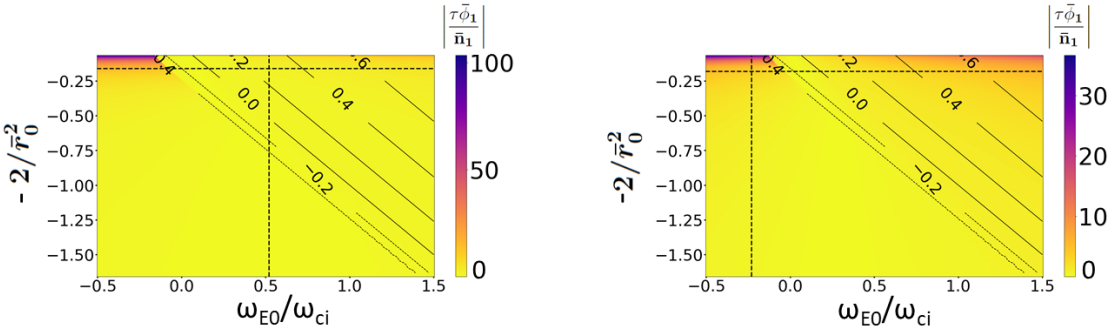

Figure 5.12.: The ratio of normalized fluctuations multiplied with τ ($|\tau\bar{\phi}_1/\bar{n}_1|$) for $m = 1$ (left) and for $m = 3$ (right) as a function of normalized $E \times B$ flow frequency (ω_{E0}/ω_{ci}) and $-2/\bar{r}_0^2$ where $\bar{r}_0$ is the normalized plasma size. The color bar represents ($|\tau\bar{\phi}_1/\bar{n}_1|$) and the constant lines on the contour represent $\bar{\omega}_0$. The dashed lines corresponds to the value of $-2/\bar{r}_0^2$ and ω_{E0}/ω_{ci} for which experimental measurements are presented in Chapter 2 for Configurations I and III.

Fig. 5.12 shows τ times the potential fluctuations $\bar{\phi}_1$ relative to density fluctuations $\bar{n}_1$ as a function of ω_{E0}/ω_{ci} and $-2/\bar{r}_0^2$ for $m = 1$ and $m = 3$. The parameter $\tau = T_{e0_{ref}}/T_{i0}$ varies depending on the experimental configuration, therefore the quantity $|\tau\bar{\phi}_1/\bar{n}_1|$ has been shown in the Fig. 5.12 instead of $|\bar{\phi}_1/\bar{n}_1|$.

The ratio $|\tau\bar{\phi}_1/\bar{n}_1|$ is closer to zero in the region where $(\bar{\omega} - m\bar{\omega}_{E0})$ approaches to zero and therefore $|\tau\bar{\phi}_1/\bar{n}_1|$ as well. This is valid for low azimuthal mode numbers. Additionally, the relative amplitude of the fluctuations increases as $-2/\bar{r}_0^2$ increases.

The analysis of Figure 5.12 reveals that establishing a fixed criterion for instability identification based on the ratio $|\bar{\phi}_1/\bar{n}_1|$, as previously proposed by [Jas72], is challenging. This ratio is influenced by various experiment-specific variables that can differ from one experimental setup to another.

Comparison with the experiment

This quantity $|\bar{\phi}_1/\bar{n}_1|$ has also been determined from the experimental measurements in Section 2.9 of Chapter 2 for Configurations I and III. Here $\bar{\phi}_1$ and $\bar{n}_1$ corresponds to $e\tilde{V}_p/k_B T_{e0}$ and $\tilde{n}/n_0$ respectively as given in Chapter 2. $T_{e0} \approx 3$ eV and $T_{i0} \approx 0.2$ eV for both reference cases which evaluates $\tau \approx 15$.

According to Eq. 5.44, $|\bar{\phi}_1/\bar{n}_1|$ is approximately 0.13 for $m = 1$ (Fig. 5.12 (a)), $\bar{\omega}_{E0} = 0.52$ and $-2/\bar{r}_0^2 = -0.16$. These values of $\bar{\omega}_{E0}$ and $-2/\bar{r}_0^2$ corresponds to the Configuration I given in Chapter 2. For Configuration III (in Chapter 2), the relative amplitude of the fluctuations ($|\bar{\phi}_1/\bar{n}_1|$) corresponding to $m = 3$ (Fig. 5.12 (b)), $\bar{\omega}_0 = -0.23$ and $-2/\bar{r}_0^2 = -0.18$ is approximately 0.24. There is a large discrepancy between the experimental values of $|\bar{\phi}_1/\bar{n}_1|$ obtained for the Configuration I and III in Chapter 2 and the theoretical values obtained here.

It has to be emphasized that the experimental measurements are conducted when the plasma is in a non-linear saturated state, whereas the model presented here is based on linear assumptions. As a result, there may be a discrepancy between the theoretical results and the observations obtained from experiments. Furthermore, the experiment was conducted under high-pressure conditions, where the influence of collisions becomes prominent. In contrast, the model presented in this study does not consider collisions.

5.6.4.3. Phase difference

Another essential information regarding the mode structure of the instability is the phase difference between density and potential fluctuations. This is a quantity that can be measured experimentally and which determines the level of particle flux driven by the fluctuations $\bar{n}_1\bar{\mathbf{v}}_{i1}$ and $\bar{n}_1\bar{\mathbf{v}}_{e1}$. To calculate the phase difference between $\bar{\phi}_1$ and $\bar{n}_1$, we write, $\frac{\bar{\phi}_1}{\bar{n}_1} = Ae^{i\phi_p}$, which gives the phase difference ϕ_p,

$$\phi_p = \tan^{-1}\left(\frac{\bar{\gamma}}{\bar{\omega}_r - m\bar{\omega}_{E0}}\right) \tag{5.45}$$

Fig. 5.13 shows the phase difference between $\bar{\phi}_1$ and $\bar{n}_1$ as a function of ω_{E0}/ω_{ci} and $-2/\bar{r}_0^2$ for $m = 1$ and $m = 3$. Note that $\bar{r}_0$ does not appear explicitly in Eq. (5.45) but comes in the expression for $Z = \bar{r}_b^2/\bar{r}_0^2$ and $\bar{\omega}_0$ which determines $\bar{\gamma}$ and $\bar{\omega}_r$. Therefore, by varying $\bar{r}_0$, the combined effect of Z as well as $\bar{\omega}_0$ on the phase difference can be

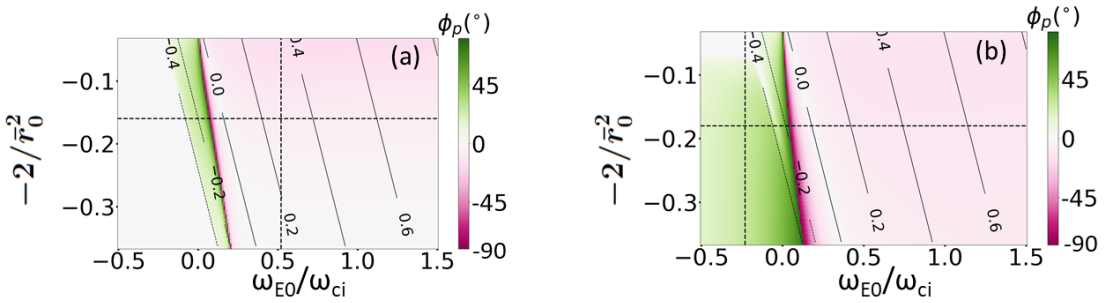

Figure 5.13.: Phase difference between $\bar{\phi}_1$ and $\bar{n}_1$ for (a). $m = 1$ and (b). $m = 3$ as a function of normalized $E \times B$ flow frequency (ω_{E0}/ω_{ci}) and $-2/\bar{r}_0^2$ where $\bar{r}_0$ is the normalized plasma size. The color bar represents the phase difference in degrees and the constant lines on the contour represent $\bar{\omega}_0$. The dashed lines corresponds to the value of $-2/\bar{r}_0^2$ and ω_{E0}/ω_{ci} for which experimental measurements are performed in Chapter 2 for ref. cases C and D.

observed.

The phase shift is close to zero except in a narrow region where $\bar{\omega}_r - m\bar{\omega}_{E0}$ is approaching zero. In this region, the phase shift becomes large, $|\phi_p| \sim 90°$ and changes sign. Furthermore, the critical value of $\bar{\omega}_{E0}$ at which the phase shift changes from negative to positive increases with decreasing $\bar{r}_0$.

5.6.5. Azimuthal mode number spectra

In Fig. 5.14, the normalized growth rate $\bar{\gamma}$, Doppler shifted frequency ($\bar{\omega}_r - m\bar{\omega}_0$), and normalized real frequency $\bar{\omega}_r$, computed numerically by solving the dispersion relation (Eq. (5.31)) are shown as a function of m. The growth rate is increasing with the mode number m irrespective of the sign of $\bar{\omega}_0$. At high m numbers, finite Larmor radius (FLR) effects are strongly stabilizing [Hoh63b] and should be taken into account. In a fluid description, they enter in the gyroviscosity tensor, neglected here, but shown to stabilize high m numbers in [Che66]. In other words, FLR effects are important when $k_\theta \rho_i \sim 1$ where $k_\theta = m/r$ is the azimuthal wave number. This corresponds to, $m \sim r/\rho_i$, which implies that the FLR stabilization ($\gamma \to 0$) comes into effect when $m > r/\rho_i$. This means that for MISTRAL plasma, at B=160 G and $T_i \approx 0.2$ eV, modes with azimuthal mode number $m > 5$ can possibly get stabilized due to FLR effects. This threshold on m at which the FLR effects become important increases with the increase in magnetic field strength.

Furthermore, the growth rate is zero for $\bar{\omega}_0 = 0$ as discussed in Fig. 5.7. For $m = 1$, $\bar{\gamma}$ is of the order of 10^{-2} for positive values of $\bar{\omega}_0$ and for $\bar{\omega}_0 = -0.2$, and zero for $\bar{\omega}_0 = -0.4$ and 0. For similar values of $\bar{\omega}_0$ but in opposite directions, there is a small difference in the growth rate up to $m = 5$ and this difference in the growth rate escalates with the increasing mode number m. Overall the growth rate increases with the increase in $\bar{\omega}_0$. The Doppler shifted frequency ($\bar{\omega}_r - m\bar{\omega}_0$) has the sign opposite to that of $\bar{\omega}_0$ for $\bar{\omega}_0 < 0$. For $\bar{\omega}_0 > 0$, the Doppler shifted frequency has the sign opposite to $\bar{\omega}_0$ until

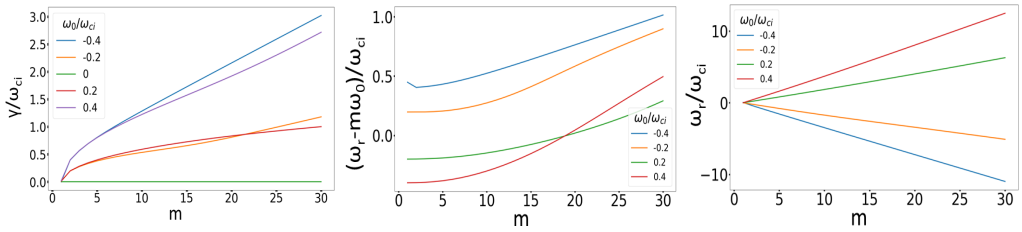

Figure 5.14.: (a). Normalized growth rate $\bar{\gamma} = \gamma/\omega_{ci}$, (b). Normalized Doppler shifted frequency $(\omega_r - m\omega_0)/\omega_{ci}$ and (c). Normalized frequency $\bar{\omega}_r = \omega_r/\omega_{ci}$ as a function of azimuthal mode number m for various values of normalized equilibrium flow frequency $\bar{\omega}_0 = \omega_0/\omega_{ci}$ used in the global dispersion relation (Eq. (5.31)). Here $Z \approx 10.8$.

$m < 20$. The real part of the frequency $\bar{\omega}_r$ in the laboratory frame has also been shown in Fig. 5.14(c) to show the dominance of the factor $m\bar{\omega}_0$.

5.6.6. Comparison of local and global dispersion relation

In this section, the impact of the local approximation (Eqs. (5.40)-(5.41)) is discussed. In Fig. 5.15, the mode growth rate obtained in the local approximation with and without LFA is shown as a function of $\bar{\omega}_0$ and $\bar{r}^2/\bar{r}_0^2$ for $m = 1, 2$ and 10. Similarly to the radially global results, the LFA assumption is shown to have a validity domain restricted to low $\bar{\omega}_0$ values and low m numbers. Relaxing the LFA opens up new instability regions, in particular at low m numbers where an unstable zone is obtained at $\bar{\omega}_0 < 0$. For $\bar{\omega}_0 = 0$, no instability exists and stable anti-drift modes with a propagation frequency $\bar{\omega}_r = m\bar{r}_0^2/2\bar{r}^2$ are predicted without the LFA [Fri64].

In contrast to the local dispersion relation which evaluates the growth rate at each radial position, the global dispersion relation describes the growth rate of an eigenmode extending over the whole cylinder radius. To compare the local and global model predictions, we show in Fig. (5.17), the maximum growth rate, $\bar{\gamma}_{max}$, obtained with the local model over the interval $0 \leq \bar{r} \leq \bar{r}_b$ as a function of $\bar{\omega}_0$ and $Z = \bar{r}_b^2/\bar{r}_0^2$, see Fig. 5.16 for an example. In Fig. 5.16, the growth rate obtained from the global solution (Eq. 5.31) is compared to the growth rate obtained from the local solution (Eq. 5.40) in blue.

This quantity $\bar{\gamma}_{max}$ is compared to the global model predictions in Fig. 5.17 (d,e,f). All results are shown without the LFA. In Fig. 5.17 (a,b,c), we see that for $\bar{\omega}_0 > 0$, the value of $\bar{\gamma}_{max}$ is largely independent of $Z = \bar{r}_b^2/\bar{r}_0^2$. This is because the radial position at which the maximum growth rate is obtained in the local model is close to zero, see Fig. 5.15(a,b,c). The situation is different for $\bar{\omega}_0 < 0$ and low m number where the local growth rate increases with $\bar{r}$ (see Fig. 5.15(a)). This is reflected by an increase of $\bar{\gamma}_{max}$ with $\bar{r}_b^2/\bar{r}_0^2$.

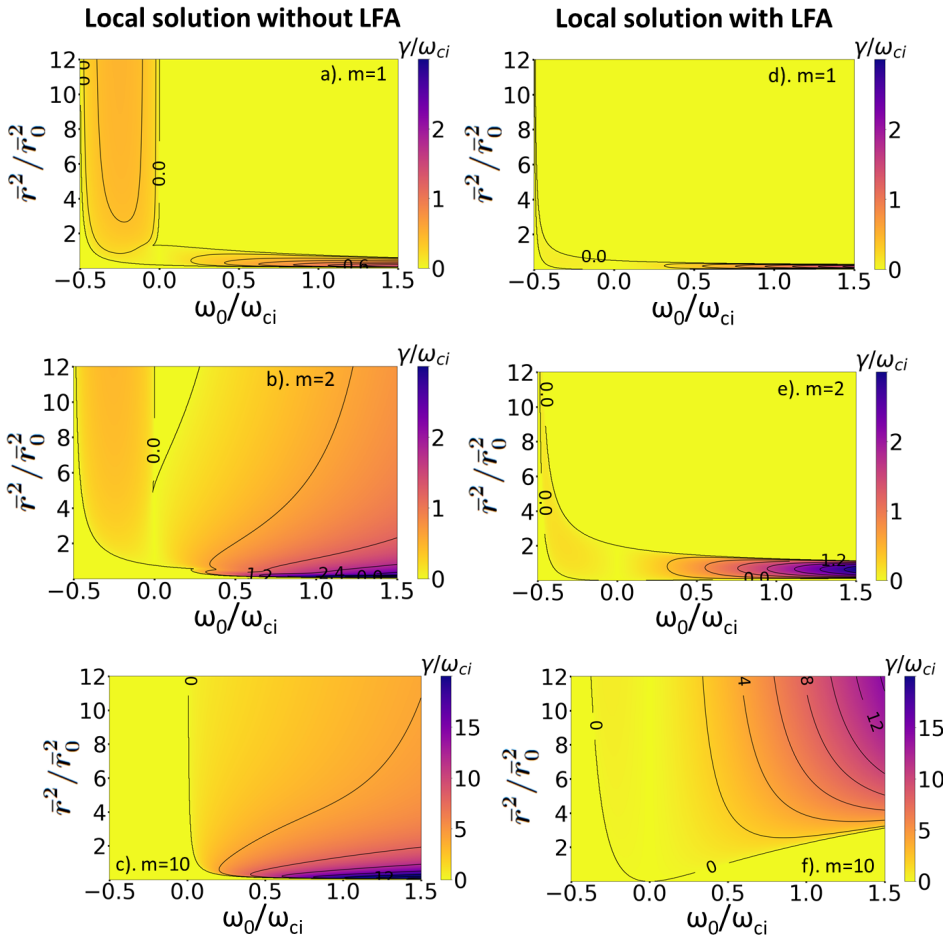

Figure 5.15.: Normalized growth rate γ/ω_{ci} as a function of normalized equilibrium flow frequency (ω_0/ω_{ci}) and $\bar{r}^2/\bar{r}_0^2$ for the local dispersion relation given by Eq. (5.40) (Figs. (a,b,c)) and Eq. (5.41) (Figs. (d,e,f)). The color bar represents the normalized growth rate ($\bar{\gamma} = \gamma/\omega_{ci}$).

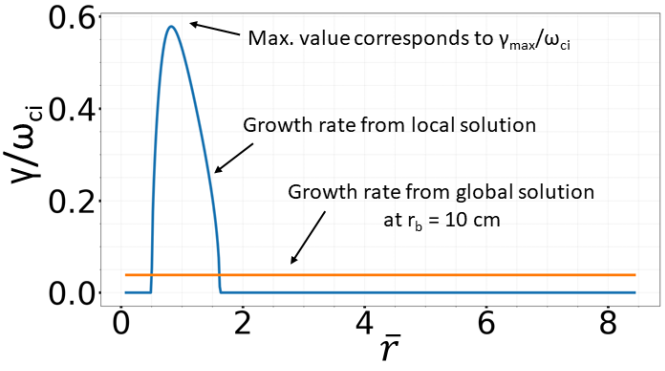

Figure 5.16.: Normalized growth rate $\bar{\gamma} = \gamma/\omega_{ci}$ as a function of the normalized radial position $\bar{r}$ for mode number $m = 1$ and $\bar{\omega}_0 = 0.6$. The blue curve represents the case when $\bar{\gamma}$ is evaluated using local dispersion relation (Eq. 5.40) and the orange curve corresponds to the global solution (Eq. 5.31).

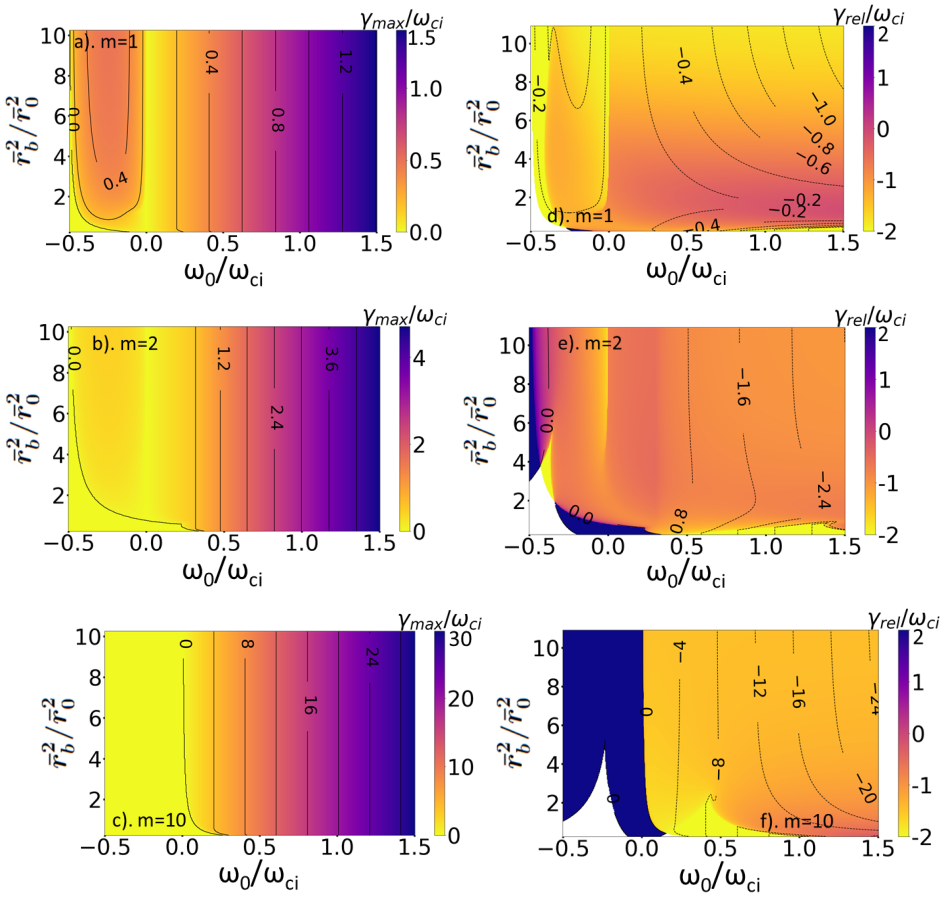

Figure 5.17.: Normalized maximum growth rate γ_{max}/ω_{ci} as a function of normalized equilibrium flow frequency (ω_0/ω_{ci}) and $\bar{r}_b^2/\bar{r}_0^2$ for the local dispersion relation given by Eq.(5.40) (Figs. (a,b,c)). Normalized relative growth rate γ_{rel}/ω_{ci} as a function of normalized equilibrium flow frequency (ω_0/ω_{ci}) and $\bar{r}^2/\bar{r}_0^2$ where $\bar{\gamma}_{rel} = 2(\bar{\gamma}_{max} - \bar{\gamma}_{global})/(\bar{\gamma}_{max} + \bar{\gamma}_{global})$ and $\bar{\gamma}_{global}$ is evaluated using Eq. (5.31) (Figs. (d,e,f)). The constant lines on Figs. (d,e,f) represents the difference between $\bar{\gamma}_{max}$ and $\bar{\gamma}_{global}$.

In both cases, $\bar{\gamma}_{max}$ is obtained close to the radial boundaries, either $\bar{r} = 0$ or $\bar{r} = \bar{r}_b$, where global effects are non-negligible. This is why the relative difference between the $\bar{\gamma}_{max}$ and $\bar{\gamma}_{global}$, shown in Fig. 5.17, is always significant, except perhaps when the growth rate is closer to zero. The dark blue region in Fig. 5.17(d,e,f) where $\bar{\gamma}_{rel}$ is maximum corresponds to the region where $\bar{\gamma}_{max} = 0$ but $\bar{\gamma}_{global}$ remains finite, leading to large value of $\bar{\gamma}_{max} - \bar{\gamma}_{global}$. The white region in Fig. 5.17(d,e,f) corresponds to the region where both $\bar{\gamma}_{max}$ and $\bar{\gamma}_{global}$ corresponds to zero. From the comparison, it is evident that the local dispersion relation cannot be used to study the global behavior of weakly magnetized rotating plasma systems having frequencies comparable to the ion-cyclotron frequency.

5.7. Summary

In this Chapter, the linearized momentum equations for ions and electrons are coupled with their respective continuity equations to establish a relationship between the perturbed normalized density ($\bar{n}_1$) and the perturbed normalized potential ($\bar{\phi}_1$). Then coupling the assumption of quasi-neutrality and the relation $\Phi_1 = \bar{n}_1 + \tau\bar{\phi}_1$, a linear differential equation is obtained for the collisionless case. The resulting differential equation corresponds to an eigenvalue problem. Its solution is obtained using Kummer's function, a special function that satisfies a specific second-order linear differential equation called the Whittaker equation. Determining the value of N using Kummer's function becomes instrumental in solving the cubic dispersion relation. This dispersion relation captures the global behavior of the system under consideration.

The linear stability analysis is then performed using the derived dispersion relation for MISTRAL-like plasma parameters. The growth rate is found to be strongly affected by the equilibrium azimuthal flow $\bar{\omega}_0$ which mainly depends on the $\mathbf{E}\times\mathbf{B}$ flow and diamagnetic flow. No instability is found for $\bar{\omega}_0 = 0$. For fixed $\bar{\omega}_0$ and density gradient, the azimuthal mode number m and the radial boundary limit $\bar{r}_b$ are the dominant factors affecting the growth rate. At a fixed radial boundary, the phase difference between normalized density fluctuations and potential fluctuations can vary significantly based on several factors, including the mode number, equilibrium flow frequency, $\mathbf{E}\times\mathbf{B}$ flow frequency, the parameter $\bar{r}_0$, and the radial boundary $\bar{r}_b$. Comparison between theoretical predictions and experimental results for the amplitude of normalized potential to density fluctuations revealed certain discrepancies. These discrepancies can be attributed to two main factors: ion-neutral collisionality and non-linear effects.

The comparison of the dispersion relation with and without low-frequency assumption (LFA), revealed that as soon as the equilibrium flow frequency is a fraction of the ion-cyclotron frequency, with the exact threshold depending on the parameters m and Z, relaxing the LFA is mandatory. More precisely the LFA becomes inaccurate when the Doppler shifted frequency, $\bar{\omega}_r - m\bar{\omega}_0$, becomes comparable to ω_{ci}.

The local solution of the dispersion relation was compared to the global solution showing that there is no parameter range where the local model is applicable. This is because the local mode predicts a maximum growth rate either close to the plasma axis or outer cylinder where boundary effects are essential. Rotating plasmas subject to centrifugal instability like MISTRAL, require a non-local treatment taking the boundary into account.

As ion-neutral collisionality can be significantly high in the present plasma system, the model is further developed to include ion-neutral collisions which will be the subject of next chapter.

6. Extension of the linear stability analysis to the collisional case

In this chapter, we obtain the dispersion relation by considering ion-neutral collisions with the approximation $\epsilon = \frac{\bar{\nu}_{in}\bar{\omega}_0}{C} << 1$. As a first step, the dispersion relation is then obtained using the approximation $\epsilon \to 0$ but with finite $\bar{\nu}_{in}$. The growth rate and perturbed frequency obtained from the dispersion relation with and without collisions are then compared to emphasize the impact of collisionality.

6.1. Linear ion response with ion-neutral collisions

Including the ion-neutral collisions (ν_{in}), the linearized ion-momentum equation (Eq. (5.14)) modifies to,

$$-i(\bar{\omega}_{ph} + i\bar{\nu}_{in})\bar{\mathbf{v}}_{i1} = C(\bar{\mathbf{v}}_{i1} \times \mathbf{b}) - \nabla\Phi_1 + \frac{\bar{r}\bar{\nu}_{in}\bar{\omega}_0}{C}\left(\bar{\mathbf{v}}'_{i1} + \frac{\bar{\mathbf{v}}_{i1}}{\bar{r}}\right) \tag{6.1}$$

Substituting $\bar{\nu}_{in} = 0$, one recovers the collisionless case as given by Eq. 5.14. The terms highlighted in red represent new quantities introduced by including ion-neutral collisionality. The term $\bar{\nu}_{in}\bar{\mathbf{v}}_{i1}$ arises from the frictional force term in the perturbed ion momentum equation (Eq. 4.25). The incorporation of ion-neutral collisions in the momentum equation of ions modifies the inertial force term, due to the radial component of the equilibrium flow (in red on the RHS of Eq. 6.1). The detailed expression for $(\bar{\mathbf{v}}_i \cdot \nabla)\,\bar{\mathbf{v}}_i$ can be found in Appendix E.

Eq. 6.1 writes:

$$-i\bar{\omega}_c\bar{\mathbf{v}}_{i1} = C\,(\bar{\mathbf{v}}_{i1} \times \mathbf{b}) - \nabla\Phi_1 + \epsilon\left(\bar{r}\bar{\mathbf{v}}'_{i1} + \bar{\mathbf{v}}_{i1}\right) \tag{6.2}$$

Noting $\bar{\omega}_c = \bar{\omega}_{ph} + i\bar{\nu}_{in}$ and $\epsilon = \bar{\nu}_{in}\bar{\omega}_0/C$. In MISTRAL plasmas, the parameter ϵ is observed to be small, typically of the order of 10^{-2}, see Figs. 4.10 and 4.11 shown in Chapter 4. This is because when the neutral pressure is increased, the electric potential profile flattens, resulting in the $\mathbf{E}\times\mathbf{B}$ frequency ω_{E0}, and therefore ω_0, much smaller and compensating for the increase in ν_{in}. The experimental observation of $\epsilon << 1$ motivates performing an expansion in this parameter to solve Eq. 6.2. We expanded $\bar{\mathbf{v}}_{i1}$ in powers of ϵ,

$$\bar{\mathbf{v}}_{i1} = \bar{\mathbf{v}}^{(0)}_{i1} + \epsilon\bar{\mathbf{v}}^{(1)}_{i1} + \epsilon^2\bar{\mathbf{v}}^{(2)}_{i2} + \ldots\ldots \tag{6.3}$$

where $\bar{\mathbf{v}}^{(0)}_{i1}$ is the ion fluid velocity when $\epsilon = 0$ but not necessarily $\bar{\nu}_{in} = 0$. Assuming

$\epsilon << 1$, Eq. 6.3 reduces to $\bar{\mathbf{v}}_{i1} = \bar{\mathbf{v}}_{i1}^{(0)} + \epsilon \bar{\mathbf{v}}_{i1}(1)$. Substituting this value of $\bar{\mathbf{v}}_{i1}$ in Eq. 6.2 and neglecting terms of the order of $O(\epsilon^2)$ and higher, the zeroth order component, $\bar{\mathbf{v}}_{i1}^{(0)}$ is,

$$\bar{\mathbf{v}}_{i1}^{(0)} = \frac{C}{C^2 - \bar{\omega}_c^2}\left[\mathbf{b} \times \nabla\Phi_1 + \frac{i\bar{\omega}_c}{C}\nabla\Phi_1\right] \tag{6.4}$$

This is the same solution as obtained for the collisionless case (Eq. 5.15), but with $\bar{\omega}_{ph}$ replaced by $\bar{\omega}_c = \bar{\omega}_{ph} + i\bar{\nu}_{in}$. The first order component $\bar{\mathbf{v}}_{i1}^{(1)}$ is,

$$-i\bar{\omega}_c\bar{\mathbf{v}}_{i1}^{(1)} = C\left(\bar{\mathbf{v}}_{i1}^{(1)} \times \mathbf{b}\right) + \bar{r}\bar{\mathbf{v}}_{i1}^{\prime(0)} + \bar{\mathbf{v}}_{i1}^{(0)} \tag{6.5}$$

Taking the cross product of the above equation with $\mathbf{b}$ from RHS and then substituting the value of $\bar{\mathbf{v}}_{i1}^{(1)} \times \mathbf{b}$, the above equation becomes:

$$\left(\frac{C^2 - \bar{\omega}_c^2}{C}\right)\bar{\mathbf{v}}_{i1}^{(1)} = -\frac{i\bar{\omega}_c}{C}\left(\bar{r}\bar{\mathbf{v}}_{i1}^{(0)\prime} + \bar{\mathbf{v}}_{i1}^{(0)}\right) - \mathbf{b} \times \left(\bar{r}\bar{\mathbf{v}}_{i1}^{(0)\prime} + \bar{\mathbf{v}}_{i1}^{(0)}\right) \tag{6.6}$$

where,

$$\bar{\mathbf{v}}_{i1}^{\prime(0)} = \frac{C}{C^2 - \bar{\omega}_c^2}\left[\mathbf{b} \times \nabla\Phi_1^{\prime} + \frac{im}{\bar{r}^2}\Phi_1\hat{e}_r + \frac{i\bar{\omega}_c}{C}\left(\nabla\Phi_1^{\prime} - \frac{im}{\bar{r}^2}\Phi_1\hat{e}_\theta\right)\right] \tag{6.7}$$

$$\mathbf{b} \times \bar{\mathbf{v}}_{i1}^{(0)} = \frac{C}{C^2 - \bar{\omega}_c^2}\left[-\nabla\Phi_1 + \frac{i\bar{\omega}_c}{C}\mathbf{b} \times \nabla\Phi_1\right] \tag{6.8}$$

$$\mathbf{b} \times \bar{\mathbf{v}}_{i1}^{\prime(0)} = \frac{C}{C^2 - \bar{\omega}_c^2}\left[-\nabla\Phi_1^{\prime} + \frac{im}{\bar{r}^2}\Phi_1\hat{e}_\theta + \frac{i\bar{\omega}_c}{C}\left(\mathbf{b} \times \nabla\Phi_1^{\prime} + \frac{im}{\bar{r}^2}\Phi_1\hat{e}_r\right)\right] \tag{6.9}$$

Substituting these terms in Eq. 6.6 and solving it further, we obtain the expression for $\bar{\mathbf{v}}_{i1}^{(1)}$:

$$\bar{\mathbf{v}}_{i1}^{(1)} = \left(\frac{1}{C^2 - \bar{\omega}_c^2}\right)^2\left[\left(C^2 + \bar{\omega}_c^2\right)\left(\Phi_1^{\prime}\hat{e}_r + \bar{r}\nabla\Phi_1^{\prime}\right) - 2iC\bar{\omega}_c\mathbf{b} \times \left(\Phi_1^{\prime}\hat{e}_r + \bar{r}\nabla\Phi_1^{\prime}\right)\right] \tag{6.10}$$

The next step is to obtain the linearized divergence of the ion particle flux,

$$\nabla \cdot (n_i\bar{\mathbf{v}}_i)|_1 = n_0\nabla \cdot \bar{\mathbf{v}}_{i1} + \bar{\mathbf{v}}_{i1} \cdot \nabla n_0 + n_1\nabla \cdot \bar{\mathbf{v}}_0 + \bar{\mathbf{v}}_0 \cdot \nabla n_1 \tag{6.11}$$

Compared to the collisionless case (Eq. 5.16), new contribution arises due to finite radial equilibrium flow.

Expanding Eq. 6.11 in terms of $\bar{\mathbf{v}}_{i1}^{(0)}$ and $\bar{\mathbf{v}}_{i1}^{(1)}$ using Eq. 6.3, we get:

$$\nabla \cdot (n_i\bar{\mathbf{v}}_i)|_1 = n_0\nabla \cdot \bar{\mathbf{v}}_{i1}^{(0)} + \bar{\mathbf{v}}_{i1}^{(0)} \cdot \nabla n_0 + \epsilon\left(n_0\nabla \cdot \bar{\mathbf{v}}_{i1}^{(1)} + \bar{\mathbf{v}}_{i1}^{(1)} \cdot \nabla n_0\right) + n_1\nabla \cdot \bar{\mathbf{v}}_0 + \bar{\mathbf{v}}_0 \cdot \nabla n_1 \tag{6.12}$$

The terms $n_0\nabla \cdot \bar{\mathbf{v}}_{i1}^{(0)}$, $\bar{\mathbf{v}}_{i1}^{(0)} \cdot \nabla n_0$ are the same as given by Eq. 5.17 and Eq. 5.18 respectively, the only difference being $\bar{\omega}_{ph}$ will be replaced by $\bar{\omega}_c$. The new terms in red

are,

$$n_0\nabla\cdot\bar{\mathbf{v}}_{i1}^{(1)} = n_0\frac{C^2+\bar{\omega}_c^2}{(C^2-\bar{\omega}_c^2)^2}\left(\bar{r}\Phi_1'''+3\Phi_1''-\frac{m^2}{\bar{r}}\Phi_1'+\frac{1}{\bar{r}}\Phi_1'\right) \tag{6.13}$$

$$\bar{\mathbf{v}}_{i1}^{(1)}\cdot\nabla n_0 = n_0\frac{C^2+\bar{\omega}_c^2}{(C^2-\bar{\omega}_c^2)^2}\left(-\frac{r\bar{\Phi}_1''}{\bar{L}_n}-\frac{\Phi_1'}{\bar{L}_n}+\frac{2mC\bar{\omega}_c}{C^2+\bar{\omega}_c^2}\frac{\Phi_1'}{\bar{L}_n}\right) \tag{6.14}$$

$$n_1\nabla\cdot\bar{\mathbf{v}}_{i0} = -2\epsilon n_1 \tag{6.15}$$

$$\bar{\mathbf{v}}_{i0}\cdot\nabla n_1 = im\bar{\omega}_0 n_1-\bar{r}\epsilon n_1' \tag{6.16}$$

Here n_1' can be written in terms of Φ_1 using Eq. 5.8 and Eq. 5.22,

$$n_1' = -\frac{m\bar{\omega}_{*0}}{(\bar{\omega}_{ph}-m(\bar{\omega}_{E0}-\bar{\omega}_0))(1+\alpha_*)}\left(n_0'\Phi_1+n_0\Phi_1'\right) \tag{6.17}$$

which when divided with n_0 becomes,

$$\frac{n_1'}{n_0} = \frac{m\bar{\omega}_{*0}}{(\bar{\omega}_{ph}-m(\bar{\omega}_{E0}-\bar{\omega}_0))(1+\alpha_*)}\left(\frac{\Phi_1}{\bar{L}_n}-\Phi_1'\right) \tag{6.18}$$

Here α_* is given by Eq. 5.23 and $1/\bar{L}_n = -n_0'/n_0 = 2\bar{r}/\bar{r}_0^2$ is the normalized density gradient and depends on the parameterization used for the density profile.

Substituting all the required terms in Eq. 6.12 and rearranging them, we get a third-order linear differential equation,

$$\begin{aligned}&\epsilon\Phi_1'''+\left[\frac{C_{NC}}{\bar{r}}+\epsilon\left(\frac{3}{\bar{r}}-\frac{1}{\bar{L}_n}\right)\right]\Phi_1''+\left[\frac{C_{NC}}{\bar{r}}\left(\frac{1}{\bar{r}}-\frac{1}{\bar{L}_n}\right)+\epsilon\left(-\frac{m^2}{\bar{r}^2}+\frac{1}{\bar{r}}\left(\frac{1}{\bar{r}}-\frac{1}{\bar{L}_n}\right)\right.\right.\\ &\qquad\left.\left.+\frac{2mC\bar{\omega}_c}{\bar{r}\bar{L}_n(C^2+\bar{\omega}_c^2)}-\frac{m}{\bar{r}\bar{L}_n\left(\bar{\omega}_{ph}+m\delta\bar{\omega}_0\right)}\frac{(C^2-\bar{\omega}_c^2)^2}{C^2+\bar{\omega}_c^2}\right)\right]\Phi_1'\\ &+\left[\frac{C_{NC}}{\bar{r}}\left(-\frac{m^2}{\bar{r}^2}-\frac{m}{\bar{r}\bar{L}_n}\left(\frac{C^2-\bar{\omega}_c^2}{\bar{\omega}_{ph}+m\delta\bar{\omega}_0}\frac{\bar{\omega}_{ph}}{\bar{\omega}_c}-\frac{C}{\bar{\omega}_c}\right)\right)-\epsilon\frac{m}{\bar{r}\bar{L}_n(\bar{\omega}_{ph}+m\delta\bar{\omega}_0)}\frac{(C^2-\bar{\omega}_c^2)^2}{C^2+\bar{\omega}_c^2}\left(\frac{2}{\bar{r}}-\frac{1}{\bar{L}_n}\right)\right]\Phi_1=0\end{aligned} \tag{6.19}$$

where,

$$C_{NC} = i\bar{\omega}_c\left(\frac{C^2-\bar{\omega}_c^2}{C^2+\bar{\omega}_c^2}\right),\ \ \bar{\omega}_{ph}=\bar{\omega}-m\bar{\omega}_0,\ \ \bar{\omega}_c=\bar{\omega}_{ph}+i\bar{\nu}_{in},\ \ \delta\bar{\omega}_0=\bar{\omega}_0-\bar{\omega}_{E0}-\bar{\omega}_{*0},\ \text{and}\ C=1+2\bar{\omega}_0 \tag{6.20}$$

If $\epsilon=0$, the collisionless case given by Eq. 5.24 is recovered.

The third-order differential equation in $\bar{r}$, represented by Eq. 6.19 is cumbersome to solve due to the problem of singularity at the initial boundary $r=0$ (near the axis of plasma column). In addition, if the analytic form of Φ_1 is known, it can be

instrumental in solving the Eq. 6.19 as we did for the collisionless case. Despite efforts within the scope of this thesis, a suitable change of variables or numerical method to address this singularity problem was not identified, nor a suitable analytic form for Φ_1 was found. We, therefore, focus on the limit $\epsilon \to 0$, but retaining finite $\bar{\nu}_{in}$ in the following.

6.2. Dispersion relation in the limit $\epsilon \to 0$

As the parameter $\epsilon << 1$ for the frequency range found in MISTRAL, it would be interesting to observe the effect of collisions on the growth rate and perturbed frequency in the limit $\epsilon \to 0$. In this limit, Eq. 6.19 reduces to,

$$\Phi_1'' + \left(\frac{1}{\bar{r}} - \frac{1}{\bar{L}_n}\right)\Phi_1'' - \frac{m^2}{\bar{r}^2}\Phi_1 + \frac{1}{\bar{r}\bar{L}_n}N\Phi_1 = 0 \tag{6.21}$$

where

$$\frac{N}{m} = \frac{C}{\bar{\omega}_c} - \frac{C^2 - \bar{\omega}_c^2}{\bar{\omega}_{ph} + m\delta\bar{\omega}_0}\frac{\bar{\omega}_{ph}}{\bar{\omega}_c} \tag{6.22}$$

Eq. 6.21 has the same structure as obtained for the case without collisions (Eq. 5.24), but the expression of N is different. We can use the same method as used for the collisionless case to find the eigenvalue N. Once N is known, substituting $\bar{\omega}_c = \bar{\omega}_{ph} + i\bar{\nu}_{in}$ in Eq. 6.22 and rearranging it further, we obtain a cubic equation in $\bar{\omega}_{ph}$:

$$\bar{\omega}_{ph}^3 - \left(\frac{N}{m} - 2i\bar{\nu}_{in}\right)\bar{\omega}_{ph}^2 + \left(C - C^2 - \frac{N}{m}(m\delta\bar{\omega}_0 + i\bar{\nu}_{in}) - \bar{\nu}_{in}^2\right)\bar{\omega}_{ph} + (mC - iN\bar{\nu}_{in})\,\delta\bar{\omega}_0 = 0 \tag{6.23}$$

The dispersion relation given by Eq. 6.23 will be used for the following analysis.

6.3. Effect of collisionality and radial boundary on the growth rate and frequency of modes

The effect of collisionality is observed on the growth rate and Doppler-shifted frequency of different azimuthal mode numbers m using the dispersion relation given by Eq. 6.23. It's done for two values of $Z = \bar{r}_b^2/\bar{r}_0^2$ and the first radial mode number ($n = 0$) keeping all the other parameters unchanged. For a fixed m and n, the change in the value of Z changes the values of N and therefore influences the growth rate and Doppler shifted frequency. Another important thing to note is that it's not necessarily the lowest radial mode number that yields the largest growth rate as shown previously in Fig. 5.5 in Chapter 5. This can be seen from Fig. 6.1 where the growth rate for mode $m = 1$ is shown for different radial mode numbers n and two different values of Z or $\bar{r}_b$. For $Z \approx 2.8$, it's always $n = 0$, that yields the highest growth rate, however, this is

not the case when $Z \approx 11$.

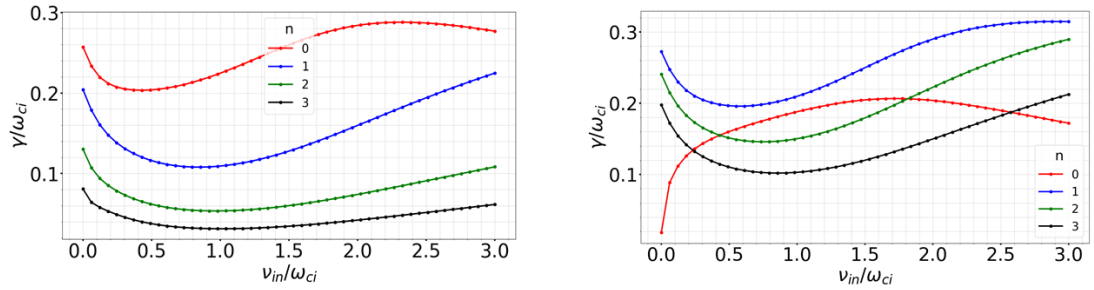

Figure 6.1.: Normalized growth rate γ/ω_{ci} of azimuthal mode number $m = 1$ as a function of normalized ion-neutral collision frequency ν_{in}/ω_{ci} for $Z \approx 2.8$ ($\bar{r}_b \approx 5.5$) (left) and $Z \approx 11$ ($\bar{r}_b \approx 11$)(right). The various curves in the figure correspond to different radial harmonics n. The parameters used are $\bar{r}_0 = 3.32$, $\bar{\omega}_{*0} = -0.18$ and $\bar{\omega}_{E0} = 0.4$.

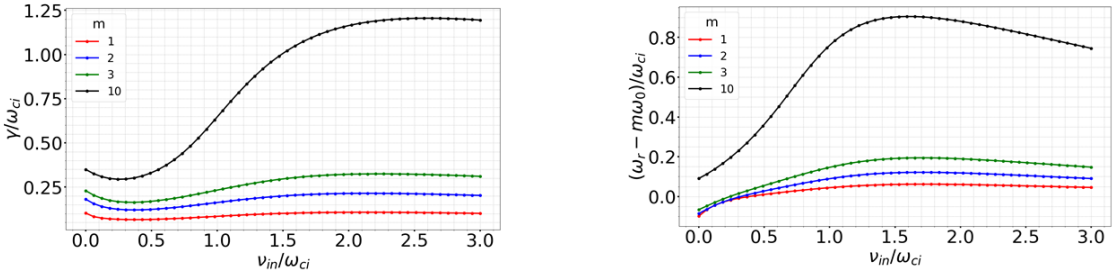

Figure 6.2.: Normalized growth rate γ/ω_{ci} (at left) and normalized Doppler shifted frequency $((\omega_r - m\omega_0)/\omega_{ci})$ (at right) as a function of normalized ion-neutral collision frequency ν_{in}/ω_{ci} for different azimuthal mode numbers. The parameters used are $\bar{r}_0 = 3.32$, $\bar{r}_b \approx 5.5$, $Z \approx 2.8$, $\bar{\omega}_{*0} = -0.18$ and $\bar{\omega}_{E0} = 0.4$. These parameters correspond to the reference case B when P=5.5×10^{-4} mbar, (see Appendix B).

The growth rate of the given modes exhibits a non-monotonic behavior with increasing collisionality (Figs. 6.2 and 6.3) in both cases, except for $m = 1$ when $Z \approx 11$. This is not the case for the Doppler-shifted frequency. At a small value of Z, the Doppler-shifted frequency of the given modes first increases and then decreases with increasing collisionality. As Z is increased, this trend changes. At a large value of Z, the Doppler-shifted frequency of the given modes is increasing with the increase in collisionality and then eventually approaches a constant value.

Interestingly, the impact of the boundary location on the mode growth rate differs at low and high collisionality. At low collisionality, increasing Z (boundary further away from the plasma) destabilizes the mode, whereas the opposite is observed at larger collisionality. This is best seen in Fig. 6.4, where the growth rate for two values of Z is shown as a function of $\bar{\nu}_{in}$. The value of collisionality where Z has no impact is indicated by a dashed black line and is found to be close to $\bar{\nu}_{in} = 1$. This change

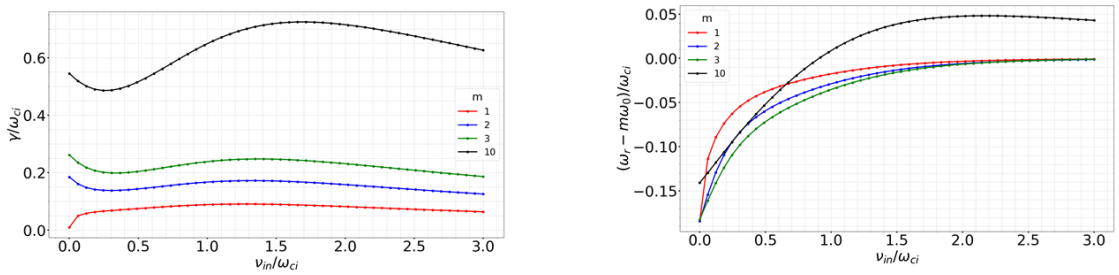

Figure 6.3.: Normalized growth rate γ/ω_{ci} (at left) and normalized Doppler shifted frequency $((\omega_r - m\omega_0)/\omega_{ci})$ (at right) as a function of normalized ion-neutral collision frequency ν_{in}/ω_{ci} for different azimuthal mode numbers. The parameters used are $\bar{r}_0 = 3.32$, $\bar{r}_b \approx 11$, $Z \approx 11$, $\bar{\omega}_{*0} = -0.18$ and $\bar{\omega}_{E0} = 0.4$.

in behavior closer to $\bar{\nu}_{in}$ suggests a transition between two distinct behaviors of instability. This hypothesis is explained in the next section.

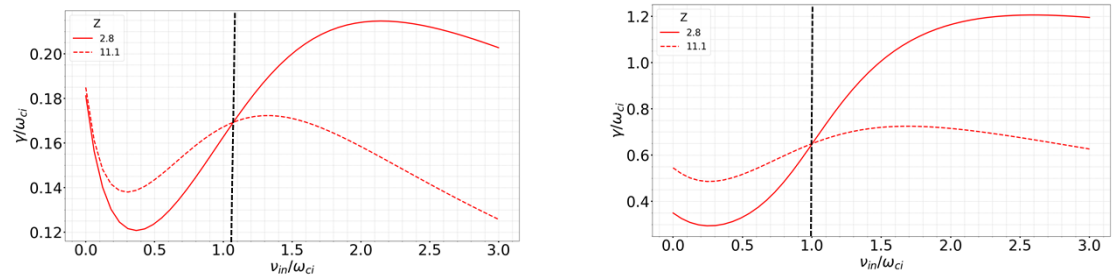

Figure 6.4.: Normalized growth rate γ/ω_{ci} as a function of normalized ion-neutral collision frequency ν_{in}/ω_{ci} for $m = 2$ (left) and $m = 10$ (right) for two different values of Z. The value of $Z \approx 2.8$ corresponds to the case when $\bar{r}_b \approx 5.5$ and the value $Z \approx 11$ corresponds to $\bar{r}_b \approx 11$. The parameters used are $\bar{r}_0 = 3.32$, $\bar{\omega}_{*0} = -0.18$ and $\bar{\omega}_{E0} = 0.4$.

6.4. Effect of ion-neutral collisions in the presence of inertia

The dispersion relation given by Eq. 6.23 in the limit $\epsilon \to 0$ accounts for the impact due to both inertia and ion-neutral collisions in addition to the electromagnetic force and pressure gradient effects. If one wants to observe the growth rate and frequency of the modes only due to the impact of ion-neutral collisions (in addition to the electromagnetic force and pressure gradient), then it can be done by setting $C = 1$ and $\bar{\omega}_{ph} = \bar{\omega}$ in Eq. 6.23. The growth rate and frequency evaluated using the dispersion relation derived with this approximation do not account for the effects due to inertia and is given as:

$$\bar{\omega}^3 - \left(\frac{N}{m} - 2i\bar{\nu}_{in}\right)\bar{\omega}^2 - \left(\frac{N}{m}(m\delta\bar{\omega}_0 + i\bar{\nu}_{in}) + \bar{\nu}_{in}^2\right)\bar{\omega} + (m - iN\bar{\nu}_{in})\,\delta\bar{\omega}_0 = 0 \qquad (6.24)$$

Figs. 6.5 and 6.6 represent the growth rate and frequencies evaluated using different dispersion relations for mode numbers $m = 1$ and $m = 10$. The main objective of presenting these plots is to observe the relative dominance of collisions over inertial effects or vice versa on the growth rate and frequency of the existing modes. It is important to note that the expression for $\bar{\omega}_0$ given by Eq. 4.45 is used in evaluating $\delta\bar{\omega}_0 = \bar{\omega}_0 - \bar{\omega}_{E0} - \bar{\omega}_{*0}$ irrespective of the effects considered to compute the growth rate and frequency shown in Figs. 6.5 and Figs. 6.6. This is done to emphasize the role of inertial effects and collisions on the modification of instability behavior keeping other parameters unchanged.

The red curve in Figs. 6.5 and 6.6 corresponds to the growth rate and frequencies evaluated using the dispersion relation given by Eq. 5.31. The blue curve represents the results obtained using Eq. 6.21, and the green curve is based on Eq. 6.24. It should be noted that for the case when collisions are not taken into account (red curve), the change in the growth rate is due to the change in equilibrium flow frequency (equilibrium flow frequency is decreasing due to an increase in collisionality (see Eq. 4.44)) in addition to inertial effects.

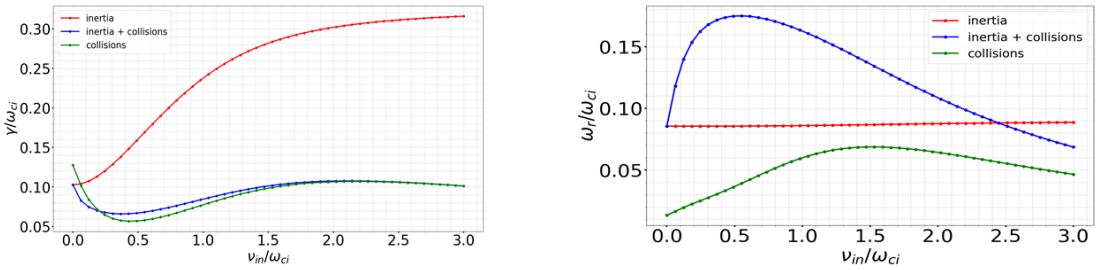

Figure 6.5.: Normalized growth rate γ/ω_{ci} (at left) and normalized perturbed frequency (ω_r/ω_{ci}) (at right) as a function of normalized ion-neutral collision frequency ν_{in}/ω_{ci} for mode $m = 1$. The parameters used are $\bar{r}_0 = 3.32$, $\bar{r}_b \approx 5.5$, $Z \approx 2.8$, $\bar{\omega}_{*0} = -0.18$ and $\bar{\omega}_{E0} = 0.4$. The parameters considered are consistent with the ref. case B in Chapter 2 when P = 4.6×10^{-4} mbar.

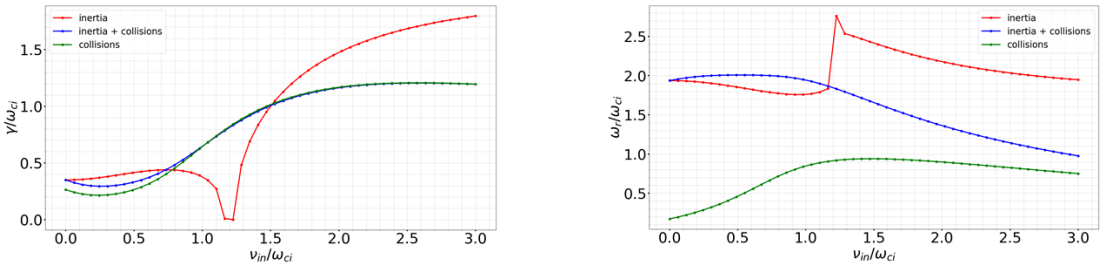

Figure 6.6.: Normalized growth rate γ/ω_{ci} (at left) and normalized perturbed frequency (ω_r/ω_{ci}) (at right) as a function of normalized ion-neutral collision frequency ν_{in}/ω_{ci} for mode $m = 10$. The parameters used are $\bar{r}_0 = 3.32$, $\bar{r}_b \approx 11$, $Z \approx 2.8$, $\bar{\omega}_{*0} = -0.18$ and $\bar{\omega}_{E0} = 0.4$.

The presented figures (Figs. 6.5 and 6.6) clearly illustrate the change in the behavior of instability when collisions are taken into account. In the absence of collisions (red curve), the growth rate is predominantly influenced by the factor $\delta\bar{\omega}_0$. The growth rate in the presence of inertial effects increases with the increase in the absolute value of $\delta\bar{\omega}_0$. However, when both collisions and inertial effects are considered (blue curve), collisions have a more significant impact on the growth rate considering that $|\delta\bar{\omega}_0|$ is the same as considered in the case with inertia. This is further evident from the green curve, where inertial effects are not considered, and the growth rate aligns more closely with the blue curve.

In addition, the disparity in the growth rates obtained by three different dispersion relations gets reduced with the increase in mode number at low values of collisionality. The threshold on collisionality (or equilibrium flow frequency for the collisionless case) at which the growth rate of the given modes converge closer to a similar value decreases with the increase in mode number.

The behavior of the normalized perturbed frequency varies depending on the considered cases. In the case with collisions only (green curve) and when inertia is considered along with collisions, the normalized perturbed frequency first decreases and then increases with increasing collisionality. However, when only inertial effects are taken into account (red curve), the perturbed frequency first shows different behavior for different mode numbers as collisionality increases.

6.5. Summary

The model given in Chapter 5 is extended to incorporate the frictional force term in the ion-momentum equation in the limit $\epsilon << 1$ where $\epsilon = \bar{\nu}_{in}\bar{\omega}_0/C$. The global dispersion relation is obtained which takes the form of a third-order differential equation. The analysis is then performed in the limit $\epsilon \to 0$. The investigation reveals that the growth rate of the modes exhibits a non-monotonic behavior with increasing collisionality. Additionally, the effect of increasing the radial boundary on the growth rate varies depending on the magnitude of collisionality. The growth rate and frequency of the modes are found to be largely affected by collisions when both the inertial effect and ion-neutral collisions are taken into account.

7. Conclusions and future prospects

The stability of rotating plasmas holds significance across various applications, including magnetically confined fusion plasma, space propulsion, plasma mass separation, and material processing. When magnetic fields are combined with transverse electric fields or electric currents, rotating plasma configurations are formed. Plasma rotation, transport perpendicular to the magnetic field, and stability are intricately linked. The perpendicular transport of plasma is influenced by turbulent processes arising from a wide range of instabilities. These instabilities are sensitive to the plasma rotation and can result in the formation of coherent rotating structures which further result in turbulent transport. The focus of this thesis was to study such instabilities leading to the formation of coherent rotating structures in MISTRAL plasma.

The experimental part of the thesis aimed to pave the way for the theoretical modeling of the MISTRAL plasma. MISTRAL plasmas were characterized at various magnetic field intensities and pressure values in a specific configuration. The profiles were parameterized to compute the inputs to be used in the theoretical model. For example, the determination of $\mathbf{E}\times\mathbf{B}$ drift frequency (ω_{E0}) and ion-diamagnetic drift frequency (ω_{*0}) were used to compute the equilibrium flow frequency (ω_0). In addition, the experimental measurements of the spoke frequency and fluctuations in electron density and potential were obtained for comparison with the predictions generated by the theoretical model. Modes $m = 1$, 2, and 3 can be seen existing experimentally, thanks to the Langmuir probe and fast camera diagnostics.

The electron density was found to follow a Gaussian distribution and the plasma potential to follow a parabolic profile with the radial electric field directed inward or outward depending on the configuration, In addition, the plasma potential was found to deviate from the parabolic shape at high pressure. This may be related to the high ion-neutral collisionality at high pressure but would deserve a more extensive investigation. An effect of pressure and magnetic field variation was observed on the mode frequency. The frequency of the mode was found to decrease with the increase in pressure whereas a decrease in mode frequency was found with the increase in magnetic field strength. $m = 1$ mode structure was observed for $P \leq 5.5 \times 10^{-4}$ mbar and B$\leq$ 240 G. There is no clear indication of mode parity at high pressure and high magnetic field due to highly oscillating plasma fluctuations in time. In a previous study conducted on MISTRAL [Bar+05], where the transition to the turbulent regime has been studied, it has been found out these strongly oscillating fluctuations can give

rise to intermittent transport at the edge of the plasma column. A deeper experimental and theoretical investigation is needed in this regard.

The rest of the thesis was focused on the theoretical modeling of the weakly magnetized rotating plasma columns. Though the analysis has been done considering the plasma parameters relevant to MISTRAL, the model is applicable to a variety of plasma systems. Existing models for studying instabilities in plasmas in cross-field configuration predominantly rely on a low-frequency approximation (LFA) for which the instability frequency and equilibrium flow are assumed to be much smaller than the ion cyclotron frequency. This approximation is challenged in weakly magnetized plasma devices including MISTRAL where the equilibrium and fluctuation frequencies are comparable to the ion-cyclotron frequency. Therefore, a significant advancement of this work was the elimination of the LFA in the existing models and emphasizing the impact of this approximation.

Firstly, a radially global dispersion relation was derived neglecting the gyro-viscosity tensor and the collisionality in the ion momentum equation but valid at arbitrary frequency values. This model predicts the stability of flute modes destabilized by a rigid body azimuthal rotation. A significant difference in the growth rate and frequency of the unstable modes was found when computed with dispersion relation with and without the LFA. This difference escalates with the increase in mode number. The radial mode number n that yields the most unstable mode is always $n = 0$ for the dispersion relation with LFA. However, when the dispersion relation without LFA is employed, the radial mode number that yields the most unstable mode corresponding to a given m varies with the variation in radial boundary and equilibrium flow frequency.

In addition, the parametric dependencies of normalized growth rate and normalized Doppler shifted frequency were investigated. The growth rate and frequency of different modes were found to be strongly influenced at small radial boundaries depending on the direction of equilibrium flow frequency. In the limit where the conducting wall is far from the plasma $\left(\frac{r_b^2}{r_0^2} >> 1\right)$, the growth rate of the most unstable mode is $\bar{\gamma} = |\bar{\omega}_0|\sqrt{m-1}$ with the corresponding Doppler shifted frequency as $\bar{\omega}_r - m\bar{\omega}_0 = -\bar{\omega}_0$ which is independent of the azimuthal mode number m. In this limit, the mode $m = 1$ is stable. When the conducting cylinder radius is reduced, the mode growth rate first increases, including that of $m = 1$ which becomes unstable before complete stabilization of all the modes is obtained. The growth rate is found to increase with the increase in azimuthal mode number. This is, at least, due to the neglect of FLR effects which come into account by including the gyro-viscosity tensor in the ion momentum equation. Including FLR effects would stabilize all modes with a wavelength smaller in comparison to the ion Larmor radius. For the parameters considered for the analysis, modes with azimuthal mode numbers $m > 5$ are expected to get stabilized due to FLR effects.

Regarding the mode structure, the modes with low azimuthal mode numbers were radially spread out more than those with high azimuthal mode numbers. The mode with the same azimuthal mode numbers gets more pushed toward the edge as the radial boundary increases. At a fixed radial boundary, the phase difference between normalized density fluctuations and potential fluctuations can take any value depending on the value of mode number, equilibrium flow frequency, $\mathbf{E}\times\mathbf{B}$ flow frequency, the parameter $\bar{r}_0$ and the radial boundary $\bar{r}_b$. The phase difference was closer to 90° in those regions where the normalized perturbed frequency ($\bar{\omega}_r$) is approaching $m\bar{\omega}_{E0}$. In addition, the critical value of $\bar{\omega}_{E0}$, at which the phase shift transitions from negative to positive, increases as $\bar{r}_0$ decreases. The theoretical predictions of the amplitude of normalized potential to density fluctuations and phase difference were also compared with the experimental results. Some discrepancies were found in the comparison as the model does not take into account ion-neutral collisionality which is relatively high in MISTRAL plasma and can possibly affect these results. In addition, the experimental measurements correspond to the non-linear state whereas the model is linear.

The comparison of the local and global solutions of the dispersion relation revealed that global effects play a critical role across all parameter ranges. The local dispersion relation, which simplifies the analysis by neglecting boundary effects and spatial variations, predicts a maximum growth rate either near the plasma axis or the outer boundary. These boundary effects and spatial variations introduce additional physics that cannot be adequately captured by the local model.

To account for the presence of a large fraction of neutrals in the plasma system, the model was extended to include the effects of ion-neutral collisions. This choice was motivated by the relatively high collision frequency between ions and neutrals compared to other species. The differential equation obtained under the assumption $\epsilon << 1$ with $\epsilon = \frac{\bar{\nu}_{in}\bar{\omega}_0}{C}$ was then solved in the limit $\epsilon \to 0$. Although the solution obtained using this limit may not be completely adequate in terms of the identification of the observed phenomenon, it still offers a first-order estimate. In the limit $\epsilon \to 0$, the growth rate and frequency of the modes are found to be strongly influenced by collisions. In the absence of collisions, the instability is primarily influenced by the centrifugal force effect caused by inertia through the change in factor $\delta\bar{\omega}_0$. However, when ion-neutral collisions are considered, the centrifugal modes undergo damping, even at low collisionality levels. As collisionality further increases, the instability becomes predominantly influenced by collisions.

Based on the findings of this study, it is difficult to interpret if the rotating structures observed in MISTRAL are attributed due to neutral drag instability or centrifugal instability, or a combination of both. Solving the radially global dispersion relation would be required to address this point. However, from the analysis done in the limit $\epsilon \to 0$, we can conclude that MISTRAL plasmas are in a regime where collisions cannot be neglected. It should also be noted that the criteria given by [Jas72] for

instability identification is not valid when the LFA is removed. The relative amplitude of the fluctuations, the phase difference, the growth rate, and the instability frequency strongly depend on various parameters ($\bar{\omega}_0$, $\bar{r}_b$, $\bar{r}_0$ and m). The required quantities can easily be computed from the dispersion relation derived in the thesis and the theoretical predictions can then be compared with the experimental results. Detailed explanations regarding the remaining open questions are provided in the subsequent section.

7.1. Future prospects

As one delves deeper into understanding a subject, it becomes evident that the number of unresolved questions arising from the study increases. This thesis has found certain unresolved issues within the context of this topic, albeit suggesting new and important directions. Further focused efforts are required to adequately address these outstanding issues along the research path.

The analysis including ion-neutral collisions in the limit $\epsilon \to 0$, does not provide adequate information. It is observed that $\epsilon << 1$ for the frequency range found in MISTRAL and therefore it might be possible that the solution of the third-order differential equation might not be very different from what we obtain in the limit $\epsilon \to 0$. However, it's not certain. Therefore, it is necessary to complete the analysis to unveil the effects of collisions on the growth rate and frequency of the existing modes. Work in this direction has been initiated to solve numerically the third-order differential equation.

The effects of weak magnetization and high collisionality which is often present in the laboratory plasmas are frequently neglected or simplified in existing models. Even the models that exist and include these effects are based on strong assumptions (low-frequency approximations, assuming cold ions, low or no collision frequencies). Developing analytically tractable models that incorporate all the relevant terms becomes challenging due to certain complexities. For example, including the FLR effects through the gyroviscosity tensor in the current model is very challenging unless the LFA is implemented as it couples the radial and azimuthal components of the ion momentum. Therefore, the development of a numerical fluid model keeping all the effects relevant to weakly magnetized plasmas can be a great initiative to understand the dynamics of plasma in such systems. In addition, there are some configurations for which rigid body rotation is not valid. The profiles measured in RAID were also not consistent with the rigid body rotation used in the model. Although the model development was done for this scenario, it never reached the stage of full linear analysis. This task can be accomplished by doing the complete linear analysis using the derived model in Appendix F. The results can be compared with the outcomes of the model based on the rigid body rotation, which has been thoroughly analyzed and presented in the thesis.

In plasma systems, the perturbations can grow to a certain extent and then saturate, reaching a nonlinear equilibrium. The linear models which focus on small perturbations around the equilibrium state can give information about the onset of the instabilities leading to the formation of large-scale structures and the threshold of certain parameters at which these instabilities get triggered. The linear models cannot capture the plasma behavior beyond the linear regime, thus giving no information about the nonlinear interactions in the system. Comparing the experimental results with the theoretical predictions of the model becomes challenging due to this discrepancy within the scope of this thesis. In addition, the non-linear interactions result in turbulent transport, one of the major problems regarding the confinement of the plasma. Therefore, nonlinear analysis is required to get a complete understanding of the plasma dynamics in the present system. An effort is going on through a collaboration with Laplace laboratory to study the MISTRAL plasma behavior using PIC simulations. This approach has the potential to uncover crucial phenomena including nonlinear effects.

Finally, the experimental study on MISTRAL would deserve further documentation. The study was conducted focusing on a specific configuration to align with the theoretical work presented in this thesis. However, it is important to recognize that different configurations can result in distinct plasma states, and therefore, it is necessary to thoroughly document the effects of boundary conditions (biasing of separating and collecting grids as well as of cylinder), pressure, and magnetic field in various configurations. It is recommended to conduct detailed measurements of density and potential fluctuations, as well as cross-phase measurements, for various configurations to enable direct comparisons of theoretical model predictions with the experimental data. By combining experimental, theoretical, and numerical approaches in parallel, it can be possible to identify and elucidate specific mechanisms that contribute to the existence of coherent rotating modes in MISTRAL and MISTRAL-like plasma systems.

A. Radial profiles of plasma potential and electron temperature

A.1. Magnetic field scans

With the identical configuration as that of ref. case A as described in Chapter 2, the radial maps of the floating potential V_f and electron temperature T_e corresponding to various magnetic field intensities are shown in Fig. A.1.

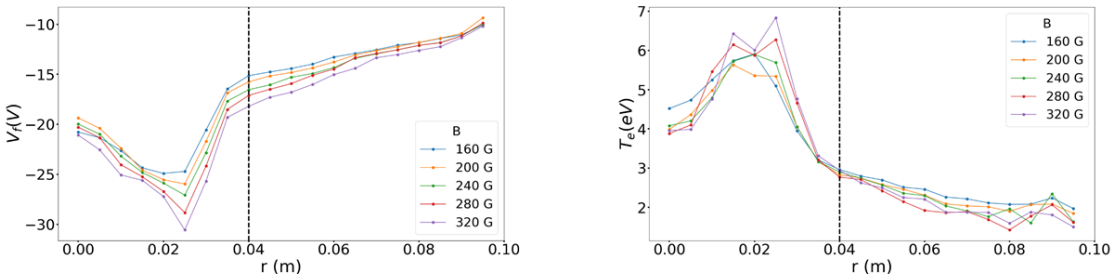

Figure A.1.: Radial variation of floating potential V_f (left) and electron temperature T_e for increasing magnetic field. The dashed black line represents the location of the limiter.

It was found that the increase in the magnetic field resulted in a slight drop in the floating potential whereas the variation in electron temperature is not following a regular trend with the increase in magnetic field. The radial variation of electron temperature exhibits a depletion zone between r = 2 and 3 cm at high magnetic fields (B=280 G and 320 G). More investigation should be done in this regard.

A.2. Pressure scans

The radial maps of the floating potential V_f and electron temperature T_e corresponding to different pressure levels are depicted in Fig. A.2 for the ref. case B in Chapter 2.

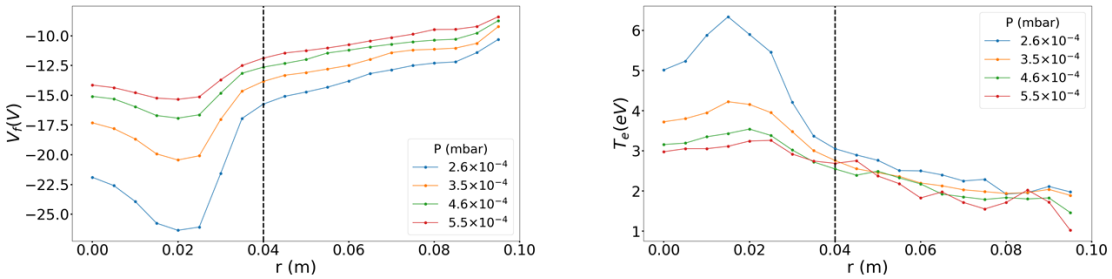

Figure A.2.: Radial variation of floating potential V_f (left) and electron temperature T_e at (a). P = 2.6×10^{-4} mbar and (b). P = 3.5×10^{-4} mbar. The dashed black line represents the location of the limiter.

Contrary to what was seen with the magnetic field change, the increase in pressure has a significant impact on the floating potential and electron temperature. The floating potential increases with the increase in pressure whereas the electron temperature decreases.

B. Extracting parameters from density and potential profiles parameterization

The linear stability analysis in the framework of this thesis is performed using the range of parameters that are experimentally relevant as found in MISTRAL. The parameters such as **E**×**B** drift frequency ($\bar{\omega}_{E0}$) and diamagnetic drift frequency ($\bar{\omega}_{*0}$) are estimated by performing the parameterization of the radial profiles of number density and plasma potential given in Chapter 2. The Gaussian distribution for number density and the parabolic profile for plasma potential provided by Eq. B.1 are used to fit the data.

$$n_0(r) = n_{00}\ exp\left(-\frac{r^2}{r_0^2}\right);\ \ \phi_0 = p_1 r^2 + p_2 \tag{B.1}$$

The expression for **E**×**B** drift frequency ($\bar{\omega}_{E0}$) and diamagnetic drift frequency ($\bar{\omega}_{*0}$) are given by Eq. 4.53 and the variation of the parameters with pressure and magnetic field is also provided in the Chapter 2 and Chapter 4 respectively. Here the values are provided in the tabular form for reference.

Table B.1 shows various parameters for a range of pressure values while keeping B constant at 160 Gauss. The corresponding values of ω_{ci} and ρ_i are 6.1 kHz and 1.8 cm respectively. The graphical representation is provided in Fig. 4.11 by Chapter 4.

P (mbar)	r_0 (cm)	p_1	p_2	$\bar{\omega}_{E0}$	$\bar{\omega}_{*0}$	$\bar{\nu}_{in}$	$\bar{\omega}_0$
7.15×10^{-5}	5.36	725.26	-7.88	2.37	-0.22	0.42	1.03
1.5×10^{-4}	5.41	569.14	-6.4	1.86	-0.22	0.89	0.8
2.6×10^{-4}	6.1	319.05	-4.37	1.04	-0.18	1.54	0.35
3.5×10^{-4}	6.07	202.7	-3.39	0.66	-0.18	2.07	0.11
4.6×10^{-4}	6.05	127.16	-2.78	0.41	-0.18	2.73	0.03
5.5×10^{-4}	6.08	95.54	-2.43	0.3	-0.18	3.26	0.01
6.7×10^{-4}	6.22	85.79	-2.24	0.28	-0.17	3.97	0.006
7.8×10^{-4}	6.47	108.87	-2.25	0.35	-0.16	4.63	0.009

Table B.1.: Varoius parameters in MISTRAL for Ar at B=160 Gauss

From P= 3.5×10^{-4} mbar onwards, the parabolic fit for plasma potential as given by Eq. B.1 does not work well as shear is present which modifies the electric field. Therefore, values of $\bar{\omega}_{E0}$ can have some factor of ambiguity and thus $\bar{\omega}_0$. However, an approximation can be made to observe the effect of an increase in pressure on various frequency values.

Table B.2 displays various parameters at different magnetic field intensities keeping P constant at 1.04×10^{-4} mbar. Due to the variation in B, ω_{ci} and ρ_i will also vary. As the ion temperature T_i is assumed to be constant, ν_{in} depends only on pressure (since the number density of neutrals changes with the change in pressure) and will also be constant, ν_{in} = 3.76 kHz. However, the normalized value will change with the change in ω_{ci}. The graphical representation is provided by Fig. 4.10 in Chapter 4.

B (Gauss)	ω_{ci} (kHz)	ρ_i (cm)	r_0 (cm)	p_1	p_2	$\bar{\omega}_E$	$\bar{\omega}_{*0}$	$\bar{\nu}_{in}$	$\bar{\omega}_0$
160	6.1	1.8	5.89	371.94	-4.15	1.2	-0.19	0.61	0.59
180	6.86	1.6	5.99	412.95	-4.74	1.09	-0.14	0.54	0.55
200	7.6	1.4	5.95	394.61	-5.25	0.82	-0.12	0.49	0.45
220	8.39	1.3	5.99	437.30	-5.83	0.75	-0.1	0.44	0.43
240	9.15	1.2	5.97	430.87	-6.45	0.62	-0.08	0.41	0.37
260	9.91	1.11	6.14	512.16	-6.98	0.63	-0.06	0.38	0.39
280	10.67	1.03	6.46	554.88	-7.52	0.59	-0.05	0.35	0.37
300	11.44	0.96	6.62	589.12	-8.11	0.55	-0.04	0.32	0.35
320	12.2	0.9	6.78	641.97	-8.81	0.52	-0.04	0.30	0.34
340	12.96	0.85	6.78	641.97	-8.81	0.52	-0.03	0.29	0.34

Table B.2.: Varoius parameters in MISTRAL for Ar at P=1.04×10^{-4} mbar

C. Zeros of Kummer's function

Eq. 5.29 used to solve Eq. 5.24 is the modified form of the confluent hypergeometric equation, known as the Whittaker equation and is helpful in solving eigenvalue problems with boundary conditions. Eq. 5.30 known as the Whittaker function gives the non-singular solution of Eq. 5.29 and can be written in terms of Kummer's function $F\left(\frac{m-N}{2}, 1+2m; z\right)$,

$$W_{N,m}(z) = z^{\frac{m+1}{2}} e^{-\frac{z}{2}} F\left(\frac{m-N}{2}, 1+2m; z\right) \tag{C.1}$$

where F is the generalized hypergeometric series given by,

$$F(a,b;z) = 1 + \frac{a}{1!\ b} z + \frac{a(a+1)}{2!\ b(b+1)} z^2 + ... \tag{C.2}$$

with $a = \frac{m-N}{2}$ and $b = 1+2m$.

The values of N obtained are used in determining the eigenfrequency from Eq. 5.25. In the previous works [RKR62], [Che66], the values of N were determined by requiring $W_{N,m}(z)$ to decay at large values of Z. This means that the power series corresponding to Kummer's function must end after a finite number of terms specified by the radial mode number n. This condition writes,

$$N = m + 2n \tag{C.3}$$

where $n = 0, 1, 2...$ is the radial mode number. This conclusion, which is known as the asymptotic solution ($Z \to \infty$), can only be reached when $Z >> 1$. However, in experiments, the value of Z is finite which means it is useful to obtain N values when the wave amplitude goes to zero at the finite radial position. This requires the numerical solution to find the zeros of Kummer's function at finite radial boundaries. The precise values of N can be found as a function of finite outer radial boundary measured by $Z = r_b^2/r_0^2$. The asymptotic values of N and the one found numerically are shown in Fig. 5.1. A more detailed explanation of Confluent hypergeometric function and radial mode numbers can be found in [SP00].

D. Finite Larmor radii effects and collisions

One of the main difficulties encountered while doing the fluid modelization was to include the gyro-viscosity tensor ($\nabla \cdot \pi_i$) which accounts for the stabilization at high m numbers due to finite Larmor radius effect as given in [RKR62],[Che66] and [Hoh63b]. All the studies that have been done until now including the gyro-viscosity tensor were done under the LFA and for collisionless plasmas, making it easy to handle the gyro-viscosity tensor term ($\nabla \cdot \pi_i$) when used in the ion-momentum equation. A more detailed expression for $\nabla \cdot \pi_i$ can be found in [Ram05]. In cylindrical coordinates, the expression of gyroviscosity tensor for finite collisionality in the limit $\bar{\nu}_{in}^2 << 1$ and homogenous $\mathbf{B} = B\hat{e}_z$, neglecting the axial fluctuations, as given in [Che66] is,

$$-\nabla \cdot \pi_i = \left(\bar{A}_r \hat{e}_r + \bar{A}_\theta \hat{e}_\theta\right) \tag{D.1}$$

Here,

$$\bar{A}_r = \bar{A}_{rr}\,\bar{v}_{ir_1} + \bar{A}_{r\theta}\,\bar{v}_{i\theta_1} \;\;;\;\; \bar{A}_\theta = \bar{A}_{\theta r}\,\bar{v}_{ir_1} + \bar{A}_{\theta\theta}\,\bar{v}_{i\theta_1} \tag{D.2}$$

$$\bar{A}_{rr} = -\frac{1}{3\bar{r}\bar{\nu}_{in}}\left[\frac{1}{\bar{r}} - \frac{\partial}{\partial \bar{r}}\left(\bar{r}\frac{\partial}{\partial \bar{r}}\right)\right] + \frac{im}{\bar{r}}\left(-\frac{1}{2\bar{L}_n} + \frac{1}{\bar{r}}\right) - \frac{m^2\bar{\nu}_{in}}{4\bar{r}^2} \tag{D.3}$$

$$\bar{A}_{\theta\theta} = -\frac{\bar{\nu}_{in}}{4\bar{r}}\left[\frac{1}{\bar{r}} - \frac{\partial}{\partial \bar{r}}\left(\bar{r}\frac{\partial}{\partial \bar{r}}\right)\right] + \frac{im}{\bar{r}}\left(-\frac{1}{2\bar{L}_n} + \frac{1}{\bar{r}}\right) - \frac{m^2}{3\bar{\nu}_{in}\bar{r}^2} + \frac{\bar{\nu}_{in}}{2\bar{L}_n}\left[\frac{1}{\bar{r}} - \frac{\partial}{\partial \bar{r}}\right] \tag{D.4}$$

$$\begin{aligned}\bar{A}_{r\theta} = \frac{1}{2}\left(\frac{\partial^2}{\partial \bar{r}^2} - \frac{m^2}{\bar{r}^2}\right) + \left[\frac{1}{2}\left(-\frac{1}{\bar{L}_n} + \frac{1}{\bar{r}}\right) + \frac{im}{\bar{r}}\left(\frac{1}{3\bar{\nu}_{in}} + \frac{\bar{\nu}_{in}}{4}\right)\right]\frac{\partial}{\partial \bar{r}} \\ - \frac{1}{\bar{r}}\left[\frac{1}{2}\left(-\frac{1}{\bar{L}_n} + \frac{1}{\bar{r}}\right) + \frac{im}{\bar{r}}\left(\frac{1}{3\bar{\nu}_{in}} + \frac{\bar{\nu}_{in}}{4}\right)\right]\end{aligned} \tag{D.5}$$

$$\begin{aligned}\bar{A}_{\theta r} = \frac{1}{2}\left(\frac{m^2}{\bar{r}^2} - \frac{\partial^2}{\partial \bar{r}^2}\right) - \left[\frac{1}{2}\left(-\frac{1}{\bar{L}_n} + \frac{1}{\bar{r}}\right) - \frac{im}{\bar{r}}\left(\frac{1}{3\bar{\nu}_{in}} + \frac{\bar{\nu}_{in}}{4}\right)\right]\frac{\partial}{\partial \bar{r}} \\ + \frac{1}{\bar{r}}\left[\frac{1}{2}\left(-\frac{1}{\bar{L}_n} + \frac{1}{\bar{r}}\right) + \frac{im}{\bar{r}}\left(\frac{1}{3\bar{\nu}_{in}} + \frac{\bar{\nu}_{in}}{4}\right) - \frac{im\bar{\nu}_{in}}{2\bar{r}\bar{L}_n}\right]\end{aligned} \tag{D.6}$$

The part without collisionality in the above equation accounts for the FLR effects and the one with collisionality accounts for collisional viscosity. These equations when substituted in the linearized form of ion momentum equation with collisionality 3.12

and then projected along the radial ($\hat{e}_r$) and azimuthal ($\hat{e}_\theta$) directions give:

$$\hat{e}_r: \quad -i\left(\bar{\omega}_{ph}+i\bar{\nu}_{in}\right)\bar{v}_{ir1}-C\bar{v}_{i\theta 1}+\bar{v}_{ir0}\left(\bar{v}'_{ir1}+\frac{\bar{v}_{ir1}}{\bar{r}}\right)=-\Phi'_1+\bar{A}_r \tag{D.7}$$

$$\hat{e}_\theta: \quad -i\left(\bar{\omega}_{ph}+i\bar{\nu}_{in}\right)\bar{v}_{i\theta 1}+C\bar{v}_{ir1}+\bar{v}_{ir0}\left(\bar{v}'_{i\theta 1}+\frac{\bar{v}_{i\theta 1}}{\bar{r}}\right)=-i\frac{m}{\bar{r}}\Phi_1+\bar{A}_\theta \tag{D.8}$$

Here ' refers to $\partial/\partial\bar{r}$. An effort was made to solve this system of equations, however, to tackle the complexities arising from the derivatives of $\bar{v}_{ir1}$, $\bar{v}_{i\theta 1}$, and Φ_1, analytical solutions for this system of equations become unwieldy. Therefore, a numerical approach should be employed to solve the system of equations to have a complete understanding of the plasma dynamics in MISTRAL-like plasmas.

E. Evaluation of convective derivative: $(\mathbf{v}\cdot\nabla)\,\mathbf{v}$

The convective derivative term appearing in the ion momentum equation (Eq. 3.12) in the cylindrical co-ordinates can be evaluated using the given formula:

$$(\mathbf{A}\cdot\nabla)\,\mathbf{B} = \left(A_r\frac{\partial B_r}{\partial r} + \frac{A_\theta}{r}\frac{\partial B_r}{\partial \theta} + A_z\frac{\partial B_r}{\partial z} - \frac{A_\theta B_\theta}{r}\right)\hat{e}_r + \left(A_r\frac{\partial B_\theta}{\partial r} + \frac{A_\theta}{r}\frac{\partial B_\theta}{\partial \theta} + A_z\frac{\partial B_\theta}{\partial z} + \frac{A_\theta B_r}{r}\right)\hat{e}_\theta + \left(A_r\frac{\partial B_z}{\partial r} + \frac{A_\theta}{r}\frac{\partial B_z}{\partial \theta} + A_z\frac{\partial B_z}{\partial z}\hat{e}_z\right) \quad \text{(E.1)}$$

Now the terms $(\mathbf{v}_{i0}\cdot\nabla)\,\mathbf{v}_{i0}$, $(\mathbf{v}_{i0}\cdot\nabla)\,\mathbf{v}_{i1}$ and $(\mathbf{v}_{i1}\cdot\nabla)\,\mathbf{v}_{i0}$ are required to evaluate the equilibrium flow and dispersion relation for the work done in this thesis. Reminding that $\mathbf{v}_{i0} = v_{ir_0}\hat{e}_r + v_{i\theta_0}\hat{e}_\theta$ where $v_{ir_0} = -r\nu_{in}\omega_0/C$ and $v_{i\theta_0} = r\omega_0$. For the linearized part, $v_{ir_1} = \left(v_{ir_1}\hat{e}_r + v_{i\theta_1}\hat{e}_\theta\right)\ exp\ [i(m\theta - \omega t)]$. The axial contribution has been neglected in the present hypotheses. Based on the form of Fourier representation of the fluctuating quantities as given by Eq. 4.34, $\partial/\partial\theta$ can be replaced with im for the terms which are θ dependent.

Using the information given, following are the expressions for the required terms,

$$(\mathbf{v}_{i0}\cdot\nabla)\,\mathbf{v}_{i0} = \left(v_{ir_0}\omega_0 - r\omega_0^2\right)\hat{e}_r + 2\omega_0 v_{ir_0}\hat{e}_\theta \quad \text{(E.2)}$$

$$(\mathbf{v}_{i0}\cdot\nabla)\,\mathbf{v}_{i1} = \Big[\left(v_{ir_0}v'_{ir_1} + im\omega_0 v_{ir_1} - \omega_0 v_{i\theta_1}\right)\hat{e}_r + \left(v_{ir_0}v'_{i\theta_1} + im\omega_0 v_{i\theta_1} + \omega_0 v_{ir_1}\right)\hat{e}_\theta\Big]\ exp\ [i(m\theta - \omega t)] \quad \text{(E.3)}$$

which on further manipulation reduces to,

$$(\mathbf{v}_{i0}\cdot\nabla)\,\mathbf{v}_{i1} = \Big[\left(v_{ir_0}(v'_{ir_1}\hat{e}_r + v'_{i\theta_1}\hat{e}_\theta\right) + im\omega_0\mathbf{v}_{i1} - \omega_0\,(\mathbf{v}_{i1}\times\mathbf{b})\Big]\ exp\ [i(m\theta - \omega t)] \quad \text{(E.4)}$$

and,

$$(\mathbf{v}_{i1}\cdot\nabla)\,\mathbf{v}_{i0} = \left[\left(v_{ir_1}v'_{ir_0} - \omega_0 v_{i\theta_1}\right)\hat{e}_r + \left(\omega_0 v_{ir_1} + \frac{v_{i\theta_1}v_{ir_0}}{r}\right)\hat{e}_\theta\right]\ exp\ [i(m\theta - \omega t)] \quad \text{(E.5)}$$

which is equivalent to,

$$(\mathbf{v}_{i1}\cdot\nabla)\,\mathbf{v}_{i0} = \left[v_{ir_1} v'_{ir_0}\hat{e}_r + \frac{v_{i\theta_1} v_{ir_0}}{r}\hat{e}_\theta - \omega_0\,(\mathbf{v}_{i1}\times\mathbf{b}) \right]\ exp\ [i(m\theta-\omega t)] \tag{E.6}$$

It should be noted that the v_{ir_0} and $v_{i\theta_0}$ are independent of θ. For the case without collisions $v_{ir_0} = 0$.

F. Solution in case of non-uniform rotation

F.1. Electron density and plasma potential profiles of RAID plasma column

A few experiments were also performed at RAID (Resonant Antenna Ion Device) to determine the characteristics and the shapes of the profiles of electron density (n_e) and plasma potential (V_p). A description of the device is given in [Fur+17]. The profiles of electron density and plasma potential of Ar plasma generated in the RAID plasma column at B=200 G and P≈ 10^{-4} mbar are shown in Fig. F.1.

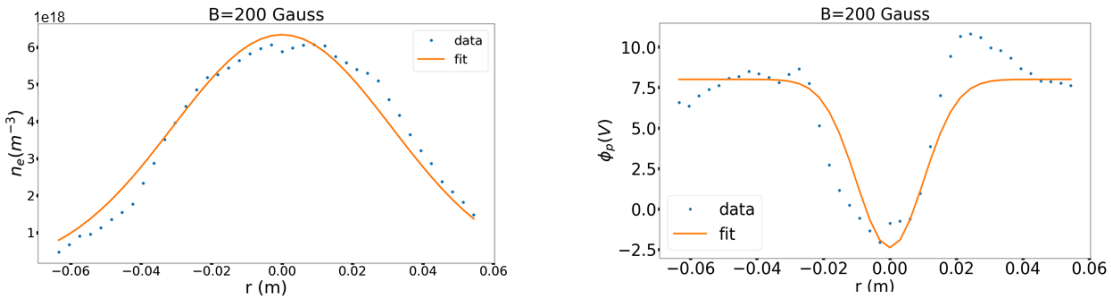

Figure F.1.: Radial variation of electron density n_e (left) and plasma potential ϕ_p.

One of the main objectives of getting the profiles of the RAID plasma column is to check the validation of the developed theory for different experiments. However, the profiles obtained for electron density and plasma potential were not consistent with the rigid body rotation assumption used for the model development. The electron density profile was found to be following a Gaussian distribution with an offset. The plasma potential can also be approximated using the Gaussian distribution with an offset. The parameterization profiles that can be used are,

$$n_e(r) = n_{offset} + n_{00}\ exp\left(-\frac{r^2}{r_0^2}\right);\ \ \phi_p = \phi_{offset} + \phi_{00}\ exp\left(-\frac{r^2}{r_\phi^2}\right) \tag{F.1}$$

where n_{offset} and ϕ_{offset} give the offset in the profiles of density and plasma potential; r_0 and r_ϕ characterize the width of the density and potential profiles respectively. As it is evident that the rigid body rotation is not applicable to RAID plasma column, a theory was developed in the following section keeping the shear into account.

F.2. Dispersion relation for non-uniform rotation in the absence of collisions and FLR effects

If the rigid body rotation is not considered, i.e. $\omega_0' \neq 0$, $\omega_0'' \neq 0$, the Eq. 5.15 for the linearized velocity changes to,

$$\bar{\mathbf{v}}_{\mathbf{i1}} = \frac{C}{C^2 - \bar{\omega}_{ph}^2}\left[\mathbf{b}\times\nabla\Phi_1 + i\frac{\bar{\omega}_{ph}}{C}\nabla\Phi_1 + \bar{r}\,\bar{v}_{ir_1}\bar{\omega}_0'\left(\frac{i\bar{\omega}_{ph}}{C}\hat{e}_\theta - \hat{e}_r\right)\right] \tag{F.2}$$

with $\bar{\omega}_{ph} = \bar{\omega} - m\bar{\omega}_0$ and $C = 1 + 2\bar{\omega}_0$ From Eq. F.2, one can write:

$$\bar{r}\,\bar{v}_{ir_1}\bar{\omega}_0' = A\left(-\frac{im}{\bar{r}}\Phi_1 + \frac{i\bar{\omega}_{ph}}{C}\Phi_1'\right) \tag{F.3}$$

where A is,

$$A = \frac{C\bar{r}\bar{\omega}_0'}{\left(C^2 - \bar{\omega}_{ph}^2\right) + C\bar{r}\bar{\omega}_0'} \tag{F.4}$$

The linearized divergence of the ion particle flux is:

$$\nabla\cdot(n_i\bar{\mathbf{v}}_i)|_1 = n_0\nabla\cdot\bar{\mathbf{v}}_{i1} + \bar{\mathbf{v}}_{i1}\cdot\nabla n_0 + \bar{\mathbf{v}}_{i0}\cdot\nabla n_1 \tag{F.5}$$

Evaluating these terms one by one,

$$n_0\nabla\cdot\bar{\mathbf{v}}_{i1} = n_0\left[\nabla\cdot\left(\frac{C}{C^2-\bar{\omega}_{ph}^2}(\mathbf{b}\times\nabla\Phi_1)\right) + i\nabla\cdot\left(\frac{\bar{\omega}_{ph}}{C^2-\bar{\omega}_{ph}^2}\nabla\Phi_1\right) + i\nabla\cdot\left(\frac{\bar{\omega}_{ph}}{C^2-\bar{\omega}_{ph}^2}\bar{r}\,\bar{v}_{ir_1}\bar{\omega}_0'\hat{e}_\theta\right) - \nabla.\left(\frac{\bar{r}C\bar{v}_{ir_1}\bar{\omega}_0'}{C^2-\bar{\omega}_{ph}^2}\hat{e}_r\right)\right] \tag{F.6}$$

Manipulating further, Eq. F.6 becomes:

$$\begin{aligned} n_0\nabla\cdot\bar{\mathbf{v}}_{i1} = in_0\Bigg[&\left(\bar{\Omega}_{ph} - \frac{\bar{\omega}_{ph}}{C}\frac{\xi(\bar{r})}{\bar{r}}\right)\Phi_1'' \\ &+\left(\bar{\Omega}_{ph}' + \frac{\bar{\Omega}_{ph}}{\bar{r}} + \frac{imA\bar{\omega}_{ph}\bar{\Omega}_{ph}}{\bar{r}C} + \frac{1}{\bar{r}}\left(\frac{m\xi(\bar{r})}{\bar{r}} - \left(\frac{\bar{\omega}_{ph}\xi(\bar{r})}{C}\right)'\right)\right)\Phi_1' \\ &+\left(-\frac{mC_1'}{\bar{r}} - \frac{m^2}{\bar{r}^2}\bar{\Omega}_{ph}(1+iA) + \frac{1}{\bar{r}}\left(\frac{m\xi(\bar{r})}{\bar{r}}\right)'\right)\Phi_1\Bigg] \end{aligned} \tag{F.7}$$

with

$$\bar{\Omega}_{ph} = \frac{\bar{\omega}_{ph}}{C^2-\bar{\omega}_{ph}^2},\quad C_1 = \frac{C}{C^2-\bar{\omega}_{ph}^2},\ \text{and}\ \xi(\bar{r}) = A\left(\frac{\bar{r}C}{C^2-\bar{\omega}_{ph}^2}\right) \tag{F.8}$$

The second term in Eq. F.5 is,

$$\bar{\mathbf{v}}_{i1}\cdot\nabla n_0 = \left(i\bar{\Omega}_{ph} - \frac{iAC_1\bar{\omega}_{ph}}{C}\right)\Phi_1' n_0' - \frac{imC_1}{\bar{r}}(1-A)\,\Phi_1 n_0' \tag{F.9}$$

and the third term in Eq. F.5 is,

$$\bar{\mathbf{v}}_{i0}\cdot\nabla n_1 = im\bar{\omega}_0 n_1 \tag{F.10}$$

Combining quasi-neutrality, $n_e = n_i$, and the continuity equations yields:

$$\nabla\cdot(n_e\bar{\mathbf{v}}_e)|_1 = \nabla\cdot(n_i\bar{\mathbf{v}}_i)|_1 \tag{F.11}$$

The term $\nabla\cdot(n_e\bar{\mathbf{v}}_e)|_1$ evaluates the same as given by Eq. 5.6 in Chapter 5. Now, substituting the required terms in Eq. F.11, a second-order differential equation is obtained:

$$\Phi_1'' + G_1\Phi_1' + G_0\Phi_1 = 0 \tag{F.12}$$

with coefficients G_1 and G_0 given as:

$$G_1 = \left(\frac{1}{\bar{r}} - \frac{1}{\bar{L}_n}\right) + \frac{C_1\bar{\omega}_0'}{\bar{L}_n}(1-\bar{r}) + \left(ln(\bar{\Omega}_{ph})\right)' + im\bar{\Omega}_{ph}\bar{\omega}_0' + \frac{mC_1^2\bar{\omega}_0'}{\bar{\Omega}_{ph}} - \bar{r}C_1\bar{\omega}_0'(ln(A))' \tag{F.13}$$

$$G_0 = \frac{\bar{r}C_1\bar{\omega}_0'}{A}\left(-\frac{m^2}{\bar{r}^2} + \frac{N}{\bar{r}\bar{L}_n}\right) - \frac{mC_1'}{\bar{r}\bar{\Omega}_{ph}} + \frac{\bar{r}C\bar{\omega}_0'}{\bar{\omega}_{ph}}\left(-i\frac{m^2}{\bar{r}^2}\bar{\Omega}_{ph} + \frac{mC_1}{\bar{r}}(ln(A))' - \frac{mC_1}{\bar{r}\bar{L}_n}\right) \tag{F.14}$$

Eq. F.12 can be solved and the effect of shear on the instability behavior can be analyzed.

Bibliography

[AYT19] Sakudo A, Yagyu Y, and Onodera T. “Disinfection and Sterilization Using Plasma Technology: Fundamentals and Future Perspectives for Biological Applications”. In: *Int J Mol Sci.* 20 (2019). DOI: 10.3390/ijms20205216 (cit. on p. 38).

[A E10] A. Escarguel. “Optical diagnostics of a low-frequency instability rotating around a magnetized plasma column”. In: *Eur. Phys. J. D* 56.2 (2010), pp. 209–214. DOI: 0.1140/epjd/e2009-00297-y (cit. on pp. 40, 41, 52, 56).

[Abo12] S N Abolmasov. “Physics and engineering of crossed-field discharge devices”. In: *Plasma Sources Science and Technology* 21.3 (May 2012), p. 035006. DOI: 10.1088/0963-0252/21/3/035006 (cit. on p. 40).

[Ada+08] J C Adam et al. “Physics, simulation and diagnostics of Hall effect thrusters”. In: *Plasma Physics and Controlled Fusion* 50.12 (2008), p. 124041. DOI: 10.1088/0741-3335/50/12/124041 (cit. on p. 38).

[Agg+23] S. Aggarwal, Y. Camenen, A. Escarguel, and A. Poyé. “Centrifugal instability in a weakly magnetized rotating plasma column”. In: *Journal of Plasma Physics* 89.3 (2023), p. 905890310. DOI: 10.1017/S002237782300051X (cit. on p. 107).

[Ann+11] B. M. Annaratone, A. Escarguel, T. Lefevre, Cyril Rebont, Nicolas Claire, and Fabrice Doveil. “Rotation of a magnetized plasma”. In: *Physics of Plasmas* 18 (2011), p. 032108. DOI: 10.1063/1.3566004 (cit. on pp. 20, 52, 97).

[AYT07] G. Y. Antar, J. H. Yu, and G. Tynan. “The origin of convective structures in the scrape-off layer of linear magnetic fusion devices investigated by fast imaging”. In: *Physics of Plasmas* 14.2 (2007), p. 022301. DOI: 10.1063/1.2424886 (cit. on p. 40).

[Bar+05] R Barni, C Riccardi, Th Pierre, G Leclert, A Escarguel, D Guyomarc’h, and K Quotb. “Formation of spiral structures and radial convection in the edge region of a magnetized rotating plasma”. In: *New Journal of Physics* 7.1 (Oct. 2005), p. 225. DOI: 10.1088/1367-2630/7/1/225 (cit. on p. 138).

[Bel06] Paul M. Bellan. *Fundamentals of Plasma Physics*. Cambridge University Press, 2006 (cit. on pp. 37, 78).

[Bro+06] F. Brochard, G. Bonhomme, E. Gravier, S. Oldenbürger, and M. Philipp. “Spatiotemporal control and synchronization of flute modes and drift waves in a magnetized plasma column”. In: *Physics of Plasmas* 13.5 (2006), p. 052509. DOI: 10.1063/1.2199807 (cit. on pp. 17, 42, 55, 79).

[BGB05] F. Brochard, E. Gravier, and G. Bonhomme. “Transition from flute modes to drift waves in a magnetized plasma column”. In: *Physics of Plasmas* 12.6 (May 2005). DOI: 10.1063/1.1921167 (cit. on pp. 17, 42).

[Che03] F. F. Chen. “Langmuir Probe Diagnostics”. In: *Mini-Course on Plasma Diagnostics, IEEE-ICOPS meeting* (2003) (cit. on pp. 50, 51).

[Che16] F. F. Chen. *Introduction to Plasma Physics and Controlled Fusion*. 2016 (cit. on pp. 36, 38, 40, 74, 76, 77, 79, 80, 93, 95, 98).

[Che66] Francis F. Chen. “Microinstability and Shear Stabilization of a Low-, Rotating, Resistive Plasma”. In: *The Physics of Fluids* 9.5 (1966), pp. 965–981. DOI: 10.1063/1.1761798 (cit. on pp. 84, 85, 101, 108, 110, 111, 114, 118, 123, 148, 149).

[Chu+69] T. K. Chu, B. Coppi, H. W. Hendel, and F. W. Perkins. “Drift Instabilities in a Uniformly Rotating Plasma Cylinder”. In: *The Physics of Fluids* 12.1 (1969), pp. 203–208. DOI: 10.1063/1.1692265 (cit. on p. 85).

[Cla+18] N Claire, A Escarguel, C Rebont, and F Doveil. “Ion velocity analysis of rotating structures in a magnetic linear plasma device”. In: *Physics of Plasmas* 25.6 (2018). DOI: https://doi.org/10.1063/1.5019448 (cit. on p. 53).

[Cor+15] O. D. Cortázar, A. Megía-Macías, O. Tarvainen, and H. Koivisto. “Experimental evidence of E × B plasma rotation in a 2.45GHz hydrogen discharge”. In: *Physics of Plasmas* 22.12 (Dec. 2015). DOI: 10.1063/1.4938033 (cit. on p. 55).

[Cro79] William Crookes. In: *Phil. Trans.* 135.1 (1879) (cit. on p. 36).

[DAn65] Nicola D’Angelo. “Kelvin—helmholtz instability in a fully ionized plasma in a magnetic field”. In: *The Physics of Fluids* 8.9 (1965), pp. 1748–1750. DOI: 10.1063/1.1761496 (cit. on p. 82).

[DK74] Daniel A. D’lppolito and Nicholas A. Krall. “Electric field driven flute instabilities in a nonuniform collisional plasma”. In: *The Physics of Fluids* 17.10 (1974), pp. 1848–1852. DOI: 10.1063/1.1694628 (cit. on p. 85).

[Dav17] P. David. “Tomography in a linear magnetised plasma”. PhD thesis. Aix-Marseille University, 2017 (cit. on pp. 47, 54).

[Dav+17] P. David, A. Escarguel, Y. Camenen, R. Baude, and D. Ferrand. “A tomography diagnostic in the visible spectrum to investigate turbulence and coherent modes in the linear plasma column Mistral”. In: *Review of Scientific Instruments* 88.11 (Nov. 2017). DOI: 10.1063/1.4998017 (cit. on pp. 54, 55).

[Den93] R. O. Dendy. *Plasma Physics: An Introductory Course*. Cambridge University Press, 1993 (cit. on pp. 38, 73, 74).

[Dif+15] G. Dif-Pradalier et al. "Finding the Elusive **E** × **B** Staircase in Magnetized Plasmas". In: *Phys. Rev. Lett.* 114 (8 Feb. 2015), p. 085004. DOI: 10.1103/PhysRevLett.114.085004 (cit. on p. 40).

[ERF12] C. L. Ellison, Y. Raitses, and N. J. Fisch. "Cross-field electron transport induced by a rotating spoke in a cylindrical Hall thruster". In: *Physics of Plasmas* 19.1 (2012), p. 013503. DOI: 10.1063/1.3671920 (cit. on p. 40).

[EKG20] Richard Engeln, Bart Klarenaar, and Olivier Guaitella. "Foundations of optical diagnostics in low-temperature plasmas". In: *Plasma Sources Science and Technology* 29.6 (June 2020), p. 063001. DOI: 10.1088/1361-6595/ab6880 (cit. on p. 53).

[Esc12] Alexandre Escarguel. *Physique des plasmas magnetises par diagnostics optiques*. Habilitation à diriger des recherches, 2012 (cit. on p. 51).

[Fre+03] Å Fredriksen, C Riccardi, L Cartegni, and H Pécseli. "Coherent structures, transport and intermittency in a magnetized plasma". In: *Plasma Physics and Controlled Fusion* 45.5 (Apr. 2003), p. 721. DOI: 10.1088/0741-3335/45/5/314 (cit. on p. 40).

[Fri64] A. M. Fridman. "On the Phenomena of the Critical Magnetic Field and Anomalous Diffusion in Weakly Ionized Plasma". In: *Soviet Physics Doklady* 9 (July 1964), p. 75 (cit. on p. 124).

[Fub+21] G. Fubiani et al. "Negative hydrogen ion dynamics inside the plasma volume of a linear device: Estimates from particle-in-cell calculations". In: *Physics of Plasmas* 28.6 (June 2021). DOI: 10.1063/5.0044358 (cit. on p. 41).

[Fur+17] I. Furno, R. Agnello, U. Fantz, A. Howling, R. Jacquier, C. Marini, G. Plyushchev, P. Guittienne, and A. Simonin. "Helicon wave-generated plasmas for negative ion beams for fusion." In: *EPJ Web of Conferences* 157 (2017). DOI: https://doi.org/10.1051/epjconf/201715703014 (cit. on pp. 40, 86, 153).

[GM09] A Fujisawa G R Tynan and G McKee. "A review of experimental drift turbulence studies". In: *Plasma Physics and Controlled Fusion* 51.11 (Oct. 2009), p. 113001. DOI: 10.1088/0741-3335/51/11/113001 (cit. on p. 81).

[GR95] R.J. Goldston and P.H. Rutherford. *Introduction to Plasma Physics*. IOP Publishing Ltd., 1995 (cit. on p. 92).

[Gon+20] V. Gonzalez-Fernandez, P. David, R. Baude, A. Escarguel, and Y. Camenen. "Spatially resolved determination of the electronic density and temperature by a visible spectro-tomography diagnostic in a linear magnetized plasma". In: *Scientific Reports* 10 (2020). DOI: 10.1038/s41598-020-62426-9 (cit. on p. 55).

[Gra+04] E. Gravier, F. Brochard, G. Bonhomme, T. Pierre, and J. L. Briançon. “Low-frequency instabilities in a laboratory magnetized plasma column”. In: *Physics of Plasmas* 11.2 (2004), pp. 529–537. DOI: 10.1063/1.1636479 (cit. on pp. 17, 42, 55).

[GRF17] Renaud Gueroult, Jean-Marcel Rax, and Nathaniel J Fisch. “Centrifugal instability in the regime of fast rotation”. In: *Physics of Plasmas* 24.8 (2017), p. 082102. DOI: https://doi.org/10.1063/1.4994546 (cit. on pp. 84, 101, 108, 114, 115).

[Gue+19] Renaud Gueroult, Stewart J. Zweben, Nathaniel J. Fisch, and J.-M. Rax. “E×B configurations for high-throughput plasma mass separation: An outlook on possibilities and challenges”. In: *Physics of Plasmas* 26.4 (2019). DOI: 10.1063/1.5083229 (cit. on p. 38).

[Hoh63a] F. C. Hoh. “Instability of Penning-Type Discharges”. In: *The Physics of Fluids* 6.8 (1963), pp. 1184–1191. DOI: 10.1063/1.1706878 (cit. on p. 83).

[Hoh63b] F. C. Hoh. “Simple Picture of the Finite Larmor Radius Stabilization Effect”. In: *The Physics of Fluids* 6.9 (1963), pp. 1359–1359. DOI: 10.1063/1.1706909 (cit. on pp. 123, 149).

[Hor99] W. Horton. “Drift waves and transport”. In: *Rev. Mod. Phys.* 71 (3 Apr. 1999), pp. 735–778. DOI: 10.1103/RevModPhys.71.735 (cit. on p. 81).

[Hut02] I. H. Hutchinson. *Principles of Plasma Diagnostics*. Cambridge University Press, 2002. DOI: 10.1017/CBO9780511613630 (cit. on p. 51).

[Ili+73] D. B. Ilić, T. D. Rognlien, S. A. Self, and F. W. Crawford. “Low-frequency flute instabilities of a hollow cathode arc discharge: Theory and experiment”. In: *The Physics of Fluids* 16.7 (1973), pp. 1042–1053. DOI: 10.1063/1.1694466 (cit. on p. 80).

[IC08] Tsuyohito Ito and Mark Cappelli. “High-Speed Images of Drift Waves and Turbulence in Magnetized Microplasmas”. In: *IEEE Transactions on Plasma Science* 36 (Sept. 2008), pp. 1228–1229. DOI: 10.1109/TPS.2008.927347 (cit. on p. 55).

[Jae10] S. Jaeger. “Etude theorique et experimentale des instabilites basses frequences dans un plasma en champs magnetique et electrique croises.” PhD thesis. Aix-Marseille University, 2010 (cit. on pp. 47, 51, 75, 86).

[Jas72] D. L. Jassby. “Transverse Velocity Shear Instabilities within a Magnetically Confined Plasma”. In: *The Physics of Fluids* 15.9 (1972), pp. 1590–1604. DOI: 10.1063/1.1694135 (cit. on pp. 70, 79, 80, 85, 86, 101, 122, 140).

[JWD14] Jay R. Johnson, Simon Wing, and Peter A. Delamere. “Kelvin Helmholtz Instability in Planetary Magnetospheres”. In: *Space Science Reviews* 184 (2014). DOI: 10.1007/s11214-014-0085-z (cit. on pp. 82, 83).

[KHK18] R Kawashima, K Hara, and K Komurasaki. "Numerical analysis of azimuthal rotating spokes in a crossed-field discharge plasma". In: *Plasma Sources Science and Technology* 27.3 (Mar. 2018), p. 035010. DOI: 10.1088/1361-6595/aab39c (cit. on p. 55).

[KJC69] Gerald I Kent, Norman C Jen, and Francis F Chen. "Transverse Kelvin-Helmholtz instability in a rotating plasma". In: *The Physics of Fluids* 12.10 (1969), pp. 2140–2151. DOI: https://doi.org/10.1063/1.1692323 (cit. on p. 82).

[KT73] N. A. Krall and A. W. Trivelpiece. *Principles of Plasma Physics*. McGraw Hill Book Company, 1973 (cit. on pp. 36, 77, 82, 98).

[Leh62] B. Lehnert. "Stabilization of Flute Disturbances by the Coriolis Force". In: *The Physics of Fluids* 5.6 (1962), pp. 740–741. DOI: 10.1063/1.1706693 (cit. on p. 84).

[Leh71] B. Lehnert. "Rotating Plasmas". In: *Nuclear Fusion* 11.5 (Oct. 1971), p. 485. DOI: 10.1088/0029-5515/11/5/010 (cit. on p. 80).

[LL05] Michael A. Libermann and Allan J. Lichtenberg. *Principles of Plasma Discharges and Material Processing*. John Wiley & Sons, 2005. ISBN: 9780471720010 (cit. on pp. 38, 41, 48–50, 75, 77, 80, 91).

[Man+11] P. Manz, M. Xu, S. H. Müller, N. Fedorczak, S. C. Thakur, J. H. Yu, and G. R. Tynan. "Plasma Blob Generation due to Cooperative Elliptic Instability". In: *Phys. Rev. Lett.* 107.4 (19 Nov. 2011), p. 195004. DOI: 10.1103/PhysRevLett.107.195004 (cit. on pp. 40, 55).

[MEW86] E M Marshall, R F Ellis, and J E Walsh. "Collisional drift instability in a variable radial electric field". In: 28.9B (Sept. 1986), p. 1461. DOI: 10.1088/0741-3335/28/9B/003 (cit. on p. 80).

[Mat+03] M. Matsukuma, Th. Pierre, A. Escarguel, D. Guyomarc'h, G. Leclert, F. Brochard, E. Gravier, and Y. Kawai. "Spatiotemporal structure of low frequency waves in a magnetized plasma device". In: *Physics Letters A* 314.1 (2003), pp. 0375–9601. DOI: https://doi.org/10.1016/S0375-9601(03)00865-X (cit. on pp. 40, 55).

[MRD08] J. R. Myra, D. A. Russell, and D. A. D'Ippolito. "Transport of perpendicular edge momentum by drift-interchange turbulence and blobs". In: *Physics of Plasmas* 15.3 (2008), p. 032304. DOI: 10.1063/1.2889419 (cit. on p. 79).

[Par20] J. Parisi. "Microstability in the Pedestal". PhD thesis. Merton College, Oxford, 2020 (cit. on p. 77).

[PJ71] F. W. Perkins and D. L. Jassby. "Velocity Shear and Low-Frequency Plasma Instabilities". In: *The Physics of Fluids* 14.1 (1971), pp. 102–115. DOI: 10.1063/1.1693259 (cit. on p. 85).

[Phe94] A. V. Phelps. “The application of scattering cross sections to ion flux models in discharge sheaths”. In: *Journal of Applied Physics* 76.2 (1994), pp. 747–753. DOI: 10.1063/1.357820 (cit. on p. 91).

[Pie+04] T. Pierre, A. Escarguel, D. Guyomarc’h, R. Barni, and C. Riccardi. “Radial convection of plasma structures in a turbulent rotating magnetized-plasma column.” In: *Phys Rev Lett.* 92.6 (2004). DOI: 10.1103/PhysRevLett.92.065004 (cit. on p. 55).

[Pie16] Thiéry Pierre. “The slow collisional E× B ion drift characterized as the major instability mechanism of a poorly magnetized plasma column with an inward-directed radial electric field”. In: *Physics of Plasmas* 23.4 (2016), p. 042110. DOI: https://doi.org/10.48550/arXiv.1602.06125 (cit. on pp. 20, 55, 97).

[Pli+15] N. Plihon et al. “Flow dynamics and magnetic induction in the von-Kármán plasma experiment”. In: *Journal of Plasma Physics* 81.1 (2015), p. 345810102. DOI: 10.1017/S002237781400083X (cit. on p. 41).

[Pli+14] Nicolas Plihon, Guillaume Bousselin, Francesco Palermo, Jorge Morales, Wouter Bos, Fabien Godeferd, Mickael Bourgoin, Jean-Francois Pinton, M. Moulin, and Ane Aanesland. “Flow dynamics and magnetic induction in the von-Karman plasma experiment”. In: *Journal of Plasma Physics* (Sept. 2014). DOI: 10.1017/S002237781400083X (cit. on pp. 40, 86).

[Pow+18] Andrew T. Powis, Johan A. Carlsson, Igor D. Kaganovich, Yevgeny Raitses, and Andrei Smolyakov. “Scaling of spoke rotation frequency within a Penning discharge”. In: *Physics of Plasmas* 25.7 (2018). DOI: 10.1063/1.5038733 (cit. on p. 55).

[Ram05] J. J. Ramos. “Fluid formalism for collisionless magnetized plasmas”. In: *Physics of Plasmas* 12.5 (2005), p. 052102. DOI: 10.1063/1.1884128 (cit. on p. 149).

[Rax+15] JM Rax, A Fruchtman, R Gueroult, and NJ Fisch. “Breakdown of the Brillouin limit and classical fluxes in rotating collisional plasmas”. In: *Physics of Plasmas* 22.9 (2015), p. 092101. DOI: https://doi.org/10.1063/1.4929791 (cit. on pp. 101, 102).

[Reb10] C. Rebont. “Etude d’une colonne de plasma magnetise parfluorescence induite par laser.” PhD thesis. Aix-Marseille University, 2010 (cit. on pp. 46, 47, 53, 54, 88).

[Reb+11] C. Rebont, N. Claire, Th. Pierre, and F. Doveil. “Ion Velocity Distribution Function Investigated Inside an Unstable Magnetized Plasma Exhibiting a Rotating Nonlinear Structure”. In: *Phys. Rev. Lett.* 106 (22 June 2011), p. 225006. DOI: 10.1103/PhysRevLett.106.225006 (cit. on p. 53).

[RT62] K. V. Roberts and J. B. Taylor. “Magnetohydrodynamic Equations for Finite Larmor Radius”. In: *Phys. Rev. Lett.* 8 (5 Mar. 1962), pp. 197–198. DOI: 10.1103/PhysRevLett.8.197 (cit. on p. 84).

[Rog73] T. D. Rognlien. “Low-frequency flute instabilities of a bounded plasma column”. In: *Journal of Applied Physics* 44.8 (1973), pp. 3505–3512. DOI: 10.1063/1.1662794 (cit. on pp. 84, 108, 110).

[RKR62] M N Rosenbluth, N A Krall, and N Rostoker. “Finite Larmor radius stabilization of "weakly" unstable confined plasmas”. In: *Nuclear Fusion, Suppl.* (1962). URL: https://www.osti.gov/biblio/4808729 (cit. on pp. 84, 110, 111, 148, 149).

[SPR09] S.Jaeger, Th. Pierre, and C. Rebont. “Direct observation of a cross-field current-carrying plasma rotating around an unstable magnetized plasma column”. In: *Physics of Plasmas* 16.2 (2009), p. 022304. DOI: 10.1063/1.3076931 (cit. on pp. 55, 89).

[Sek+15] Michael J. Sekerak, Benjamin W. Longmier, Alec D. Gallimore, Daniel L. Brown, Richard R. Hofer, and James E. Polk. “Azimuthal Spoke Propagation in Hall Effect Thrusters”. In: *IEEE Transactions on Plasma Science* 43.1 (2015), pp. 72–85. DOI: 10.1109/TPS.2014.2355223 (cit. on pp. 39, 40).

[Sha84] D.H. Sharp. “An overview of Rayleigh-Taylor instability”. In: *Physica D: Nonlinear Phenomena* 12.1 (1984), pp. 3–18. DOI: https://doi.org/10.1016/0167-2789(84)90510-4 (cit. on p. 81).

[Sim63] Albert Simon. “Instability of a Partially Ionized Plasma in Crossed Electric and Magnetic Fields”. In: *The Physics of Fluids* 6.3 (1963), pp. 382–388. DOI: 10.1063/1.1706743 (cit. on p. 83).

[SP00] GÉRARD SOSENKO PETRO P.and BONHOMME and THIÉRY PIERRE. “Global drift waves in weakly ionized magnetized plasmas: theory and observations”. In: *Journal of Plasma Physics* 63.2 (2000), pp. 157–190. DOI: 10.1017/S002237789900803X (cit. on pp. 85, 148).

[Sug+10] Satoru Sugita, Masatoshi Yagi, Sanae-I. Itoh, and Kimitaka Itoh. “Interchange Turbulence and Radial Transport in Tokamak Scrape-Off Layer Dominated by Meso Scale Structure”. In: *Journal of the Physical Society of Japan* 79.4 (2010), p. 044502. DOI: 10.1143/JPSJ.79.044502 (cit. on p. 79).

[Tan+12] H. Tanaka, N. Ohno, Y. Tsuji, K. Okazaki, and S. Kajita. “Statistical Analysis of the Spatial Behavior of Plasma Blobs Around the Plasma Column in a Linear Plasma Device”. In: *Contributions to Plasma Physics* 52.5-6 (2012). DOI: https://doi.org/10.1002/ctpp.201210027 (cit. on p. 55).

[Tyu+23] M. Tyushev, M. Papahn Zadeh, V. Sharma, M. Sengupta, Y. Raitses, J.-P. Boeuf, and A. Smolyakov. “Azimuthal structures and turbulent transport in Penning discharge”. In: *Physics of Plasmas* 30.3 (2023), p. 033506. DOI: 10.1063/5.0129804 (cit. on p. 40).

[VG21] Amparo M. Gallardo-Moreno Verónica Luque-Agudo Margarita Hierro-Oliva and M. Luisa González-Martín. “Effect of plasma treatment on the surface properties of polylactic acid films”. In: *Polymer Testing* 96 (2021), p. 107097. DOI: https://doi.org/10.1016/j.polymertesting.2021.107097 (cit. on p. 38).

[Vid21] Theo Vidril. *Étude du transport anormal dans une colonne de plasma magnétisé*. 2021 (cit. on pp. 56, 58, 64).

[WC04] J. Wesson and D.J. Campbell. *Tokamaks*. Clarendon Press, 2004. ISBN: 9780198509226 (cit. on p. 38).

[WP73] George M. Wheeler and Robert V. Pyle. “Low-frequency waves in a weakly ionized, rotating magnetoplasma”. In: *The Physics of Fluids* 16.11 (1973), pp. 1917–1921. DOI: 10.1063/1.1694234 (cit. on pp. 80, 85).

[WW] E. T. Whittaker and G. N. Watson. *A course of Modern Analysis*. Cambridge University Press (cit. on p. 110).

[Zai+23] Ilman Nuran Zaini, Rikard Svanberg, Daniel Sundberg, Kristofer Bölke, Jenny Granqvist, Cecilia Lille, Nicklas Tarantino, and Weihong Yang. “A pilot-scale test of plasma torch application for decarbonizing the steel reheating furnaces”. In: *Thermal Science and Engineering Progress* 40 (2023), p. 101766. DOI: https://doi.org/10.1016/j.tsep.2023.101766 (cit. on p. 38).